Modeling Solar Wind Mass-Loading Due to Dust in the Solar Corona

by

Anthony P. Rasca

B.A., Carroll College, 2007

M.S., University of Colorado at Boulder, 2009

A thesis submitted to the

Faculty of the Graduate School of the

University of Colorado in partial fulfillment

of the requirements for the degree of

Doctor of Philosophy

Department of Applied Mathematics

2013

This thesis entitled:
Modeling Solar Wind Mass-Loading Due to Dust in the Solar Corona
written by Anthony P. Rasca
has been approved for the Department of Applied Mathematics

Mihály Horányi

Keith Julien

Date

The final copy of this thesis has been examined by the signatories, and we find that both the content and the form meet acceptable presentation standards of scholarly work in the above mentioned discipline.

Rasca, Anthony P. (Ph.D., Applied Mathematics)

Modeling Solar Wind Mass-Loading Due to Dust in the Solar Corona

Thesis directed by Prof. Mihály Horányi

Collisionless mass-loading was first discussed to describe interactions between the solar wind and cometary atmospheres. Recent observations have led to an increased interest in mass-loading occurring in the solar corona, due to both sungrazing comets and collisional debris production by sunward migrating interplanetary dust particles. Direct coronal wind observations from future space missions, such as Solar Probe Plus, may reveal such dust sources, motivating the need of a theoretical model for mass-loading in the coronal wind.

This dissertation begins with developing a simple 1D hydrodynamic solar wind mass-loading model, demonstrating the effects of mass-loading dust into the wind. Second, the mass-loading model used in the 1D code is adapted for use with an MHD Solar Corona (SC) component of the Space Weather Modeling Framework (SWMF), with initial results compared to 1D results. The new SC component is then used for a sungrazing cometary dust source example, utilizing orbital and mass loss estimates from the recent sungrazer, Comet C/2011 W3 (Lovejoy). Both a point source and tail source (a dust source spread across a syndyne/synchrone-defined tail) of dust are used to generate a mass-loaded coronal wind. Last, we use results from our sungrazing comet example to show how solar wind properties will appear to a solar probe passing downwind of a cometary dust source.

Dedication

I dedicate this to my undergraduate advisor Dr. Kelly Cline, without whom I would not be where I am now.

Acknowledgements

This work was funded by NASA and I thank them for their support. This work also utilized the Janus supercomputer, which is supported by the National Science Foundation (award number CNS-0821794) and the University of Colorado at Boulder. The Janus supercomputer is a joint effort of the University of Colorado at Boulder, the University of Colorado at Denver and the National Center for Atmospheric Research. Janus is operated by the University of Colorado at Boulder.

I also thank my advisor Prof. Mihály Horányi for welcoming me into his research group and for his support and encouragement over the years. I would also like to thank my co-advisor Prof. Keith Julien for his mathematical guidance during times I found myself at a dead end, as well as Prof. Bengt Fornberg, Prof. Sascha Kempf, and Prof. James Meiss for agreeing to be on my committee, and my undergraduate professors Prof. Kelly Cline, Prof. Mark Parker, and Prof. Holly Zullo for all their continued help and advice during the past ten years.

Additionally, I would like to thank everyone at the University of Michigan's Center for Space Environment Modeling, especially Rona Oran, Bart Van der Holst, Tomas Gombosi, and Gábor Tóth, for all their hospitality during my brief stay in Ann Arbor, Michigan and their continued assistance with the SWMF and BATS-R-US code. Many of my results would not have been possible without their help.

Last, I would like to thank all my close friends, who have supplied much support and encouragement over the years. In particular: Former/current officemates Lois Smith and João Hooks, who were always there to grab tea or coffee with and always willing to listen during times of frustration; Fellow mathematics friends Ben Dunham, Karen Farrell, Adam Fox, Jerrad Hampton, Phil Lenzini, Adam Rose, Amrik Sen, and Adrean Webb, who have always been great graduate school company, whether it be outside the office on an adventure or while working hard together on our course and prelim studies; My hometown friends Amanda Sharp, who helped me make my initial trek out to Boulder for graduate school, and Manfred Mueller, Tatiana Mueller, Solveig Osborne, and Kevin Pease, who make me feel like I still have second home outside Colorado.

Contents

Chapter

Tables

Table

Figures

Figure

Chapter 1

Introduction

1.1 Motivation

The dynamics of charged dust particles picked up by the solar wind and other plasma environments is a growing area of interest, with several future space missions still focusing on exploring dusty plasma environments. This is in addition to past and present work observing and modeling dusty plasma environments around planetary objects such as the Moon, planetary rings, and comets (Horányi[18]). Understanding these dusty plasma environments around the solar system is important for space exploration. Additionally, they are important for engineering applications since dust impacts can cause physical damage to operating spacecraft.

In regards to observations, there are several current missions, such as the New Horizons and the Cassini-Huygens space probes, where the Student Dust Counter (SDC) and Cosmic Dust Analyzer (CDA) instruments are helping build a better picture of dust environments in the solar system (Horányi et al.[17]). Closer to the Sun, the Mercury Surface, Space Environment, Geochemistry and Ranging (MESSENGER) mission is capable of measuring charged particles around and emanating from Mercury. Additionally, a number of missions, such as the Lunar Atmospheric and Dust Environment Explorer (LADEE), are set to explore the dusty plasma environment around the Moon (Grün et al.[13]).

Current exploration of dusty plasma environments omits charged dust particles from the dust cloud forming the F-corona near the Sun. There are theoretical studies modeling the size, density, distribution, and trajectories of dust grain particles migrating in towards the Sun (Mann et al.[28]), which can then be ejected as β-meteoroids. Dust particles can also find themselves in the outer solar atmosphere, known as the corona, via larger bodies such as sungrazing comets, which release dust and gas on approach to the Sun. Upon being ionized, these particles can eventually be detected downstream by space probes such as the STEREO/WAVES instrument (S/WAVES) (Meyer-Vernet et al.[30]). There are plans to explore the solar corona and take direct measurements, such as the Solar Probe Plus (SPP) mission, but they will not begin for several years (SPP is not scheduled to launch until 2018).

This timespan devoid of direct observations in the solar corona provides the opportunity for further theoretical modeling of the coronal dusty plasma environment and the impacts dust particles have on the coronal wind. Additionally, solar satellites such as the Solar and Heliospheric Observatory (SOHO) are often discovering and observing sungrazing comets, which act as dusty probes for the solar corona, providing useful observation data prior to any direct observations. For example, a recent study of the sungrazing comet C/2011 W3 (Lovejoy) shows changes in its dust tail revealing part of the Sun's magnetic structure that were previously unobservable (Schrijver et al.[43]).

1.2 A Mass-Loading Model for Cometary Atmospheres

A major motivating paper for our study is by Biermann et al.[4]. They introduced collisionless mass-loading, the addition of mass via ionized particles (pick-up ions), in the solar wind, showing the effects of a cometary atmosphere interacting with the solar wind, eighteen years before any direct measurements were taken. Their work forms the foundation of our study modeling mass-loading in a fluid solar wind.

Biermann et al.[4] use a purely fluid, or hydrodynamic, model for the stream of protons and electrons that make up the solar wind. There are various fluid models for different circumstances, such as the Navier-Stokes equations, which are often used in a terrestrial setting and involve incompressible viscous flows. The supersonic solar wind is not incompressible, nor does viscosity play a significant role. Instead, a more fundamental hydrodynamic model must be used, known as Euler's equations.

Euler's equations are a set of hyperbolic partial differential equations in space and time, representing the conservation of mass, momentum, and energy for a fluid being being transported in a control volume. In conservative homogeneous form, they are

$$\frac{\partial \rho}{\partial t} + \nabla \cdot (\rho \mathbf{u}) = 0 \tag{1.1}$$

$$\frac{\partial \rho \mathbf{u}}{\partial t} + \nabla \cdot (\rho \mathbf{u} \otimes \mathbf{u} + p\mathbf{I}) = 0 \tag{1.2}$$

$$\frac{\partial E}{\partial t} + \nabla \cdot [\mathbf{u}\,(E + p)] = 0, \tag{1.3}$$

where ρ, $\mathbf{u}$, and p are the fluid density, velocity vector, and pressure, respectively, and where $\otimes$ is the tensor product, mapping $\mathbb{R}^n \to \mathbb{R}^{n \times n}$, used to represent each surface stress term. The energy E is independently defined using these dependent variables,

$$E = \frac{1}{2}\rho|\mathbf{u}|^2 + \frac{p}{\gamma - 1}, \tag{1.4}$$

allowing Equations 1.1-1.3 to be written in terms of either conserved variables $(\rho,\, \rho\mathbf{u},\, E)^\top$ or primitive variables $(\rho,\, \mathbf{u},\, p)^\top$. The constant γ is the adiabatic index, or heat capacity ratio,[1] which tells us how easily heat is dispersed within a fluid. Equations 1.1-1.3 also use the divergence operator ∇, which in 3D Cartesian coordinates is

$$\nabla = \left(\frac{\partial}{\partial x}, \frac{\partial}{\partial y}, \frac{\partial}{\partial z}\right)^\top. \tag{1.5}$$

Through the course of this study, we will see ∇ defined for various other coordinate systems.

It is important to note that Equations 1.1-1.3 are for a single-fluid case, which assumes all particles making up the fluid have the same in size and mass. Multi-fluid models require an additional set of conservation equations for each particle species in the fluid. The solar wind, however, is made of at least two species of particles, protons and electrons, along with some minor ions.[2] To avoid using an extremely computationally-intensive multi-fluid model, one particle species

[1] γ varies according to how well heat is exchanged in a fluid. For an adiabatic flow, where there is no heat exchange, $\gamma = 0$. For an isothermal flow, where heat exchange is instantaneous (constant temperature), $\gamma = 1$.

[2] A fluid of charged particles become susceptible to magnetic and electric fields, making it a magnetohydrodynamic (MHD) fluid. A simpler hydrodynamic model serves as a starting point for the solar wind.

is assumed, with the particle mass being the average of the particles present. Since the solar wind has approximately equal quantities of protons and electrons with masses $m_p >> m_e$, respectively, the mean particle mass μ is assumed to be

$$\mu = \frac{1}{2} m_p. \tag{1.6}$$

This single-fluid and mean particle mass assumption is used for the undisturbed solar wind in Biermann et al.[4]. A mass-loaded solar wind has a varying mean particle mass.

1.2.1 An Axially-Symmetric Fluid Model

For the specific case of Biermann et al.[4], Equations 1.1-1.3 are altered for a solar wind/cometary case. As a uniform solar wind approaches an approximately spherical cometary atmosphere and body, or nucleus, the dead-on solar wind streamline will form an axis connecting the Sun to the cometary nucleus (which they refer to as the z-axis, pointing positively away from the Sun). All off-axis streamlines do not necessarily collide with the nucleus, but are allowed the change in a radial direction. Hence, a simple 1D model would not be completely appropriate for this case, but instead an *axially-symmetric* model is used.

An axially-symmetric model uses the cylindric ∇ operator and velocity vector $\mathbf{u}$,

$$\nabla = \left(\frac{\partial}{\partial z}, \frac{1}{r}\frac{\partial}{\partial r} r \right)^{\top} \tag{1.7}$$

$$\mathbf{u} = (u_z, u_r)^{\top}, \tag{1.8}$$

where r is the direction perpendicular to the z-axis. They also introduce a fourth conservation law for solar wind particle number density n in cm^{-3} and collisionless[3] mass-loading source terms

$$\mathbf{S}_d = (S_{d0}, S_{d1}, \mathbf{S}_{d2}, S_{d3})^{\top} \tag{1.9}$$

to get the set of axially-symmetric equations

$$\frac{\partial n}{\partial t} + \frac{\partial}{\partial z}(n u_z) + \frac{1}{r}\frac{\partial}{\partial r}(r n u_r) = S_{d0} \tag{1.10}$$

[3] The ionization process used, photoionization, involved no physical interactions, or collisions, between solar wind particles and pick-up ion particles.

$$\frac{\partial \rho}{\partial t} + \frac{\partial}{\partial z}\left(\rho u_z\right) + \frac{1}{r}\frac{\partial}{\partial r}\left(r\rho u_r\right) = S_{d1} \tag{1.11}$$

$$\frac{\partial \rho u_z}{\partial t} + \frac{\partial}{\partial z}\left(\rho u_z^2\right) + \frac{1}{r}\frac{\partial}{\partial r}\left(r\rho u_z u_r\right) = S_{d2_z} \tag{1.12}$$

$$\frac{\partial \rho u_r}{\partial t} + \frac{\partial}{\partial z}\left(\rho u_z u_r\right) + \frac{1}{r}\frac{\partial}{\partial r}\left(r\rho u_r^2\right) = S_{d2_r} \tag{1.13}$$

$$\frac{\partial E}{\partial t} + \frac{\partial}{\partial z}\left[u_z\left(E+p\right)\right] + \frac{1}{r}\frac{\partial}{\partial r}\left[r u_r\left(E+p\right)\right] = S_{d3}. \tag{1.14}$$

Equation 1.10 for the conservation of particle number is present due to the addition of a third species to the solar wind from cometary gas particles. All species of particles share the same ρ, $\mathbf{u}$, p, and n variables, but n and ρ can be used to calculate the local mean particle mass in the mass-loaded wind, which allows an estimate of how many pick-up ions are present without resorting to a multi-fluid model.[4]

1.2.2 Mass-Loading Model

The mass-loading source terms contained in $\mathbf{S}_d$ are used to account for changes in the solar wind when particles are ionized and have their mass, momentum, and energy added to the flow. Biremann et al.[4] focused on three primary modes of ionization: photoionization, charge exchange, and electron impact. Mass-loading by photoionization means the particles add their mass to the system and as a consequence, if they are moving with non-negligible velocity relative to the fluid,[5] their momentum and energy as well. For the other two modes of ionization, interactions with solar wind particles already in the flow make calculating their source contributions less trivial.

According to Biremann et al.[4], at the heliospheric distances within one astronomical unit (AU), the distance used in their study, both charge exchange and electron impact become negligible relative to photoionization, allowing the dust source terms $\mathbf{S}_d = (S_{d0}, S_{d1}, \mathbf{S}_{d2}, S_{d3})^\top$ to be defined using only the photoionization process,

$$S_{d0} = P_d \tag{1.15}$$

$$S_{d1} = P_d \rho_d \tag{1.16}$$

[4] Later we will see that splitting ρ into a proton/electron density ρ_{H} and ionized dust density ρ_{d_i} has the same effect as introducing n.

[5] For most cases in this thesis mass-loading particles are assumed to be traveling at negligible velocities relative to the solar wind prior to ionization.

$$S_{d2_z} = P_d \rho_d u_{d_z} \tag{1.17}$$

$$S_{d2_r} = P_d \rho_d u_{d_r} \tag{1.18}$$

$$S_{d3} = \frac{1}{2} P_d \rho_d |\mathbf{u}_d|^2, \tag{1.19}$$

where P_d, ρ_d, and $\mathbf{u}_d = (u_{d_z}, u_{d_r})^\top$ are the neutral dust particle number ionization rate (dependent on the neutral particle density and probability of photoionization), mass density, and velocity vector, respectively. From here on, $P_d \rho_d$ will be represented by the mass-loading factor,

$$P_{ml} = P_d \rho_d, \tag{1.20}$$

defining the mass-loading rate per volume. This results from the ionization rate and mass density appearing frequently together. The particle number density then becomes $S_{d0} = P_{ml}/\rho_d$.

1.2.3 Mass-Loading Solutions in Cometary Atmospheres

Figure 1.1 shows a particular solution of Equations 1.10-1.14 along the z-axis, using cometary ion particle mass m_{C} and velocity u_{d_z} fixed values

$$m_{\mathrm{C}} = 30\, m_p \tag{1.21}$$

$$u_{d_z} = -1\,\mathrm{km/s}, \tag{1.22}$$

respectively, and undisturbed (denoted with a 0 subscript) solar wind parameters

$$\rho_0 = 3\, m_p/\mathrm{cm}^{-3} \tag{1.23}$$

$$u_{z_0} = 400\,\mathrm{km/s} \tag{1.24}$$

$$u_{r_0} = 0\,\mathrm{km/s} \tag{1.25}$$

$$p_0 = 3.8 \times 10^{-11}\,\mathrm{dyn/cm}^2. \tag{1.26}$$

The solution accurately portrays the structure of the outer cometary atmosphere sketched out in their study, including the bow shock, where the solar wind initially transitions to a subsonic flow, and the contact discontinuity, where streamlines originating from the Sun separate from those

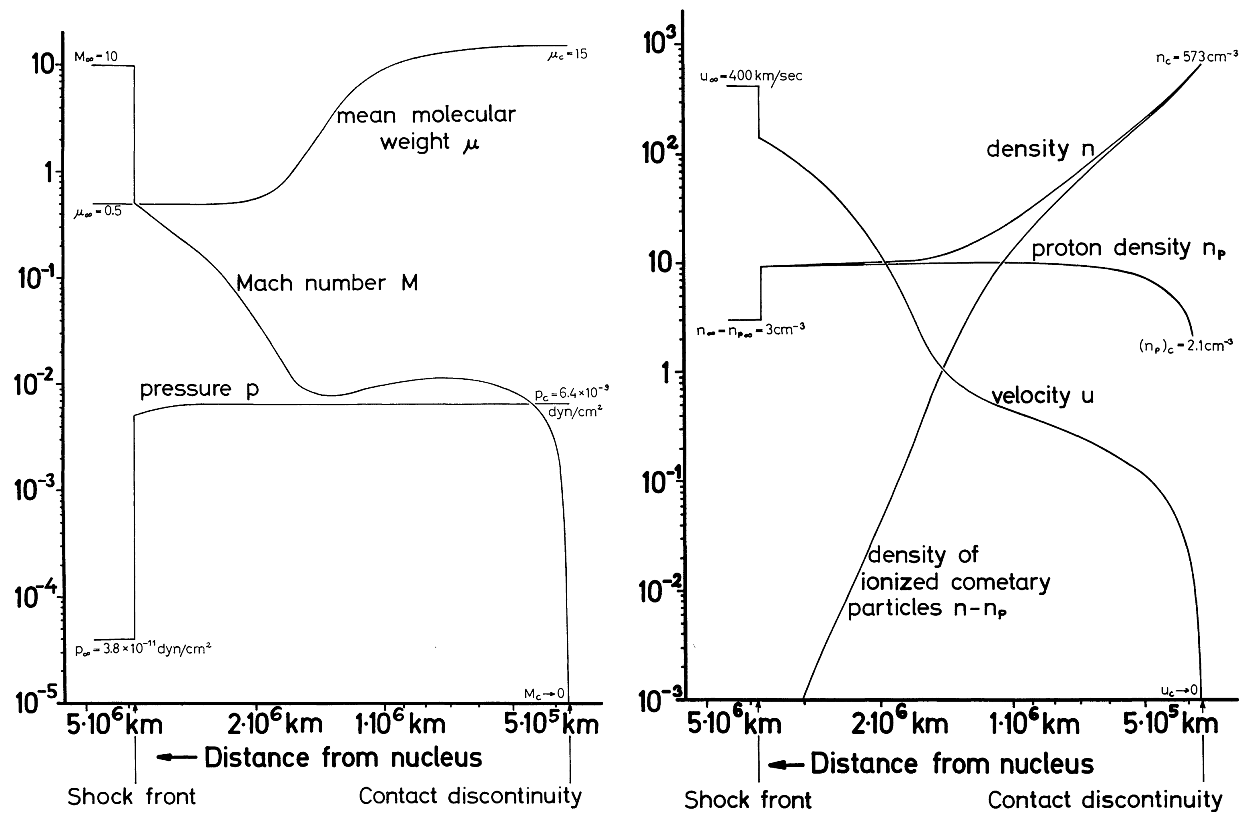

Figure 1.1: A solution to the mass-loaded solar wind along the z-axis (in cgs units, with the exception of velocity) due to pick-up ions in a cometary atmosphere, with the cometary nucleus to the right and the solar wind originating from the left. Images are reproduced from Biermann et al.[4].

originating from the comet's nucleus. However, their solution ends at the contact discontinuity and does not elaborate on what happens within the inner cometary atmosphere. The dynamics of the inner atmosphere will be mentioned again in a later chapter and will be surprisingly relevant to modeling the solar wind's acceleration through the solar corona.

1.3 Dust Distribution Modeling in the F-Corona

A second motivating paper shows a dust cloud near the Sun, forming the F-corona, using theoretical modeling (Mann et al.[28]). Originally theorized in observational studies, such as Mann and MacQueen[27], Mann et al.[28] modeled how dust grains can migrate towards the Sun. Near the Sun these dust grains can be observed via light scattering, alerting us to their presence. Similar effects are observed in the form of the zodiacal light, or even on the lunar surface, an effect called lunar horizon glow (Rennilson and Criswell[40]). The latter forms a major motivator for the previously mentioned LADEE mission.

A dust grain's ability to migrate towards the Sun depends on two forces: solar gravitation and radiation pressure. Extremely small particles, sub-micron or less, have a large β ratio of radiation pressure to gravity,

$$\beta = \frac{F_{\text{rad}}}{F_{\text{grav}}}, \tag{1.27}$$

and can easily become overwhelmed by radiation pressure and be swept up in the form of β-meteoroids. However, larger grains (1-100 μm in size, according to Mann et al.[28]) naturally migrate inward due to Poynting-Robertson (P-R) drag, in which the radiation pressure affects the angular momentum and energy of dust grains, causing them to slowly spiral towards the Sun.

Mann et al.[28] uses both P-R drag and collisions between particles to model dust grain trajectories spiraling towards the Sun. Distributions with respect to radial distances from the Sun are shown in Figure 1.2. Trajectories were modeled for a variety of dust grain sizes, compositions, and initial orbital eccentricities. The abrupt cutoff occurring between 2-4 solar radii $R_\odot$ forms the boundary of the dust-free zone, where particle-particle collisions dominate and the resulting smaller

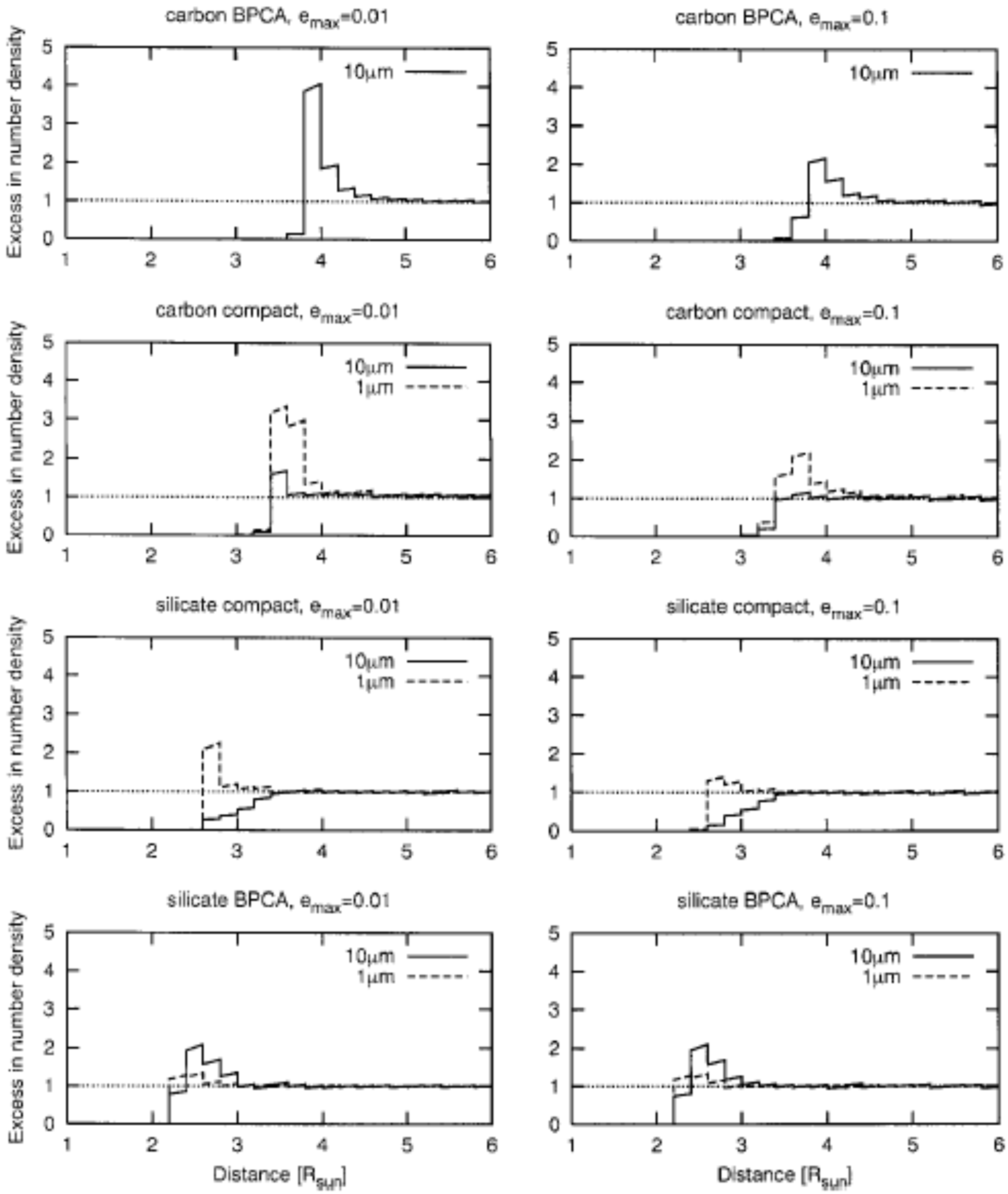

Figure 1.2: Dust grain radial distributions from theoretical modeling of grain trajectories via P-R drag and collisions. Distributions vary by dust grain size, composition, and initial orbital eccentricities. Images are reproduced from Mann et al.[28].

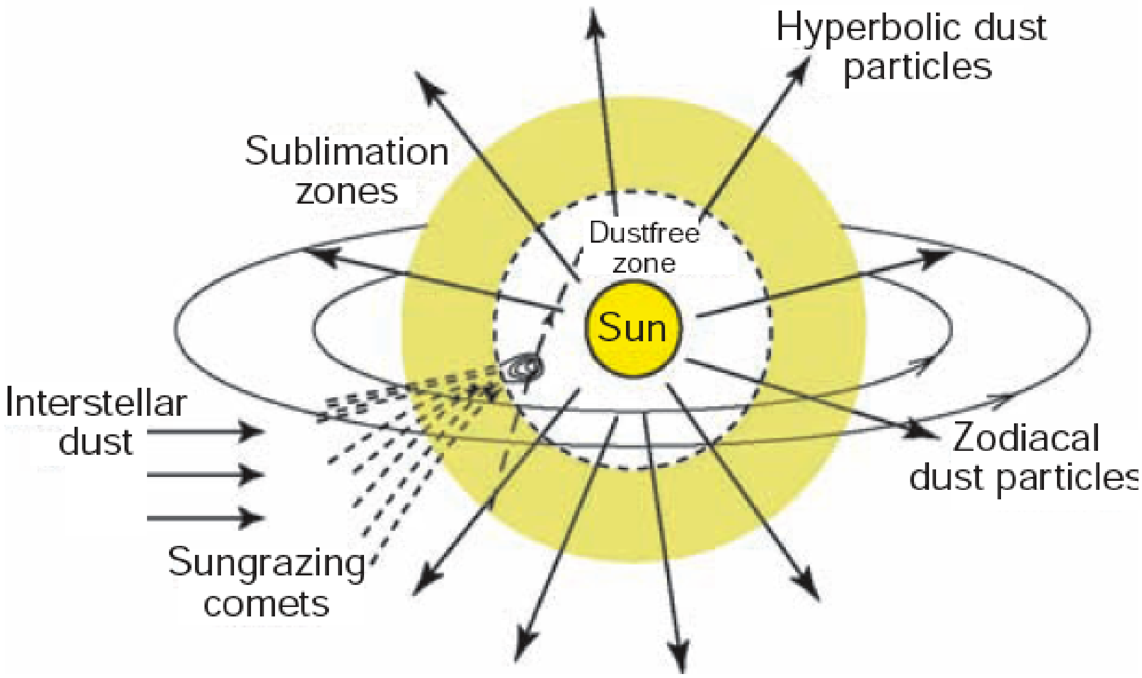

Figure 1.3: Diagram demonstrating the dust-free zone that occurs in the corona near the Sun. Dust particles are still capable existing in the dust-free zone via other means, such at larger objects (e.g. sungrazing comets, asteroids) releasing dust particles through evaporation and sputtering.

particles get ejected as β-meteoroids.

Figure 1.3 shows the theorized dust-free zone. Dust grains spiraling towards the Sun that reach this boundary get ejected (shown as hyperbolic dust particles and zodiacal dust particles in the figure). However, larger objects passing very near the Sun, such as sungrazing comets and asteroids, can deliver dust particles closer, where dust particles are ejected due to evaporation and sputtering.

Our overall goal combines these two motivations: the idea of modeling mass-loading in the solar wind and the known presence of dust near the Sun. We first aim to develop a 1D hydrodynamic coronal wind model to use in conjunction with the mass-loading model by Biermann et al.[4] and analyze the effects of a mass-loaded coronal wind. We will then expand on an existing 3D magnetohydrodynamic (MHD) solar corona model to be used as a solar wind modeling tool for our mass-loading problem.

Chapter 2

A 1D Hydrodynamic Model for Mass-Loading in the Solar Wind

Our primary goal is to develop a mass-loading component for a coronal wind environment. Before jumping to such a complex plasma environment, it is necessary to begin modeling with the most basic solar wind model. Like in Biermann et al.[4] it is best to begin with a uniform solar wind, using the velocity, density, and pressure parameters from about 1 AU in the Sun's equatorial plane. Unlike Biermann et al.[4], having a generalized non-cometary mass-loading region such as on a strictly radial interval (relative to the Sun) of pick-up dust particles allows for the reduction to a simpler 1D hydrodynamic model.

The 1D version of Equations 1.10-1.14 is essentially the same, but with the only spatial dimension being the radial distance[1] r relative to the Sun. The resulting simplified conservation equations for a flow through a cross-sectional area $A = A\left(r\right)$ then become

$$\begin{aligned}
\frac{\partial n}{\partial t} + \frac{1}{A}\frac{\partial}{\partial r}\left(Anu\right) &= S_0 && (2.1)\\
\frac{\partial \rho}{\partial t} + \frac{1}{A}\frac{\partial}{\partial r}\left(A\rho u\right) &= S_1 && (2.2)\\
\frac{\partial \rho u}{\partial t} + \frac{1}{A}\frac{\partial}{\partial r}\left(A\rho u^2\right) + \frac{\partial p}{\partial r} &= S_2 && (2.3)\\
\frac{\partial E}{\partial t} + \frac{1}{A}\frac{\partial}{\partial r}\left[Au\left(E+p\right)\right] &= S_3, && (2.4)
\end{aligned}$$

where u is now the only velocity component and the Equations 2.2-2.4 are once again not dependent on number density conservation, which is utilized to determine mean mass values. The source vector $\mathbf{S} = \left(S_0,\, S_1,\, S_2,\, S_3\right)^\top$ retains only the mass-loading source terms $\mathbf{S} = \mathbf{S}_d$, which now only accounts

[1] Note the change from the r used in the previous chapter.

for a momentum source in the radial direction. These equations will form the basis of all our 1D tests, with source term modifications introduced in the next chapter.

This chapter will demonstrate the basic mass-loading effects in a uniform solar wind, beginning with a purely mathematical formulation, allowing for an initially qualitative description of the effects a mass-loading source term can have. We will then describe a basic first-order numerical method for solving Equations 2.1-2.4 and discuss results of adding a mass-loading region to the domain. Last, we will discuss both potential higher-order numerical methods and potential implicit schemes.

2.1 Mass-Loading Effects in a Compressible Flow

Prior to any numerical results, it is best to formulate a mathematical description that will allow us to estimate the impact of suddenly adding mass to the system. While demonstrating the dynamics of an inner cometary atmosphere, Gombosi et al.[12] showed that with a steady flow through a cross-sectional area A and general sources in the momentum and energy equations ($S_0 = S_1 = 0$), a single equation can be formed by eliminating $\frac{d\rho}{dr}$ and $\frac{dp}{dr}$ to get

$$\frac{du}{dr} = -\frac{u}{1-M^2}\left(\frac{A'}{A} + \frac{1}{p}S_3 - \frac{\gamma-1}{\gamma}\frac{1}{pu}S_4\right), \tag{2.5}$$

where M is the mach number

$$M = u\sqrt{\frac{\rho}{\gamma p}}. \tag{2.6}$$

However, we are interested in the case where mass-loading source term are present in each conservation equation. Using the same methods, we derive a more generalized form of Equation 2.5,

$$\frac{du}{dr} = -\frac{u}{1-M^2}\left(\frac{A'}{A} - \frac{\gamma+1}{2\gamma}\frac{u}{p}S_2 + \frac{1}{p}S_3 - \frac{\gamma-1}{\gamma}\frac{1}{pu}S_4\right), \tag{2.7}$$

Having an equation in this form is useful for understanding the acceleration of a compressive flow. For a steady flow through a cross-sectional area A we have $\rho u A = \text{constant}$. Then

$$\frac{d}{dr}(\rho u A) = uA\frac{dp}{dr} + \rho A\frac{du}{dr} + \rho u\frac{dA}{dr} = 0 \tag{2.8}$$

$$\rightarrow \frac{1}{\rho}\frac{d\rho}{dr} + \frac{1}{u}\frac{du}{dr} + \frac{1}{A}\frac{dA}{dr} = 0. \tag{2.9}$$

Combining the steady-state homogeneous ($S_2 = S_3 = S_4 = 0$) mass and momentum equations in 1D coordinates gives us $\rho u \frac{du}{dr} + \frac{dp}{dr} = 0$. Using the sound speed relation $\frac{dp}{dr} = a^2 \frac{d\rho}{dr}$ (where we introduce the sound speed a) and substituting into Equation 2.9 we get

$$\frac{du}{dr} = -\frac{u}{1-M^2}\frac{1}{A}\frac{dA}{dr}. \tag{2.10}$$

Now calling A in Equation 2.10 the effective area A_{eff}, we can compare it with Equation 2.7 and form the relation

$$\frac{1}{A_{eff}}\frac{dA_{eff}}{dr} = \frac{A'}{A} - \frac{\gamma+1}{2\gamma}\frac{u}{p}S_2 + \frac{1}{p}S_3 - \frac{\gamma-1}{\gamma}\frac{1}{pu}S_4, \tag{2.11}$$

Where A is the purely geometrical area function. The source terms then have an effect on the area that the flow sees, the effective area.

Changes in the cross-sectional area that a fluid flows through (or that it sees via the effective area) is very important for compressible flows as it influences acceleration and deceleration. In addition, the influences vary, depending on whether the flow is subsonic or supersonic. From the relation in Equation 2.10, it is evident subsonic flows accelerate if and only if A is decreasing and vice versa for supersonic flows. Figure 2.1 shows how this effect can be used to accelerate a flow to supersonic velocities in a pinched tube called a de Laval nozzle. The compressible flow begins subsonic and is accelerated to $M = 1$ at the bottleneck and is further accelerated with the following area expansion.

For the specific case of a uniform 1D solar wind addressed in this chapter, there is a negligible area expansion effect ($A =$ constant),[2] leaving the mass-loading terms to contribute solely to the effective area. Furthermore, if the solar wind velocity is sufficiently large relative the neutral particle speed, S_2 will be the dominating source term of the three. This results in a contracting contribution to the effective area due to mass-loading sources. Consequently, we should see a decelerating supersonic wind and accelerating subsonic winds in any mass-loading regions.

[2] On larger scales and/or at closer distances to the Sun, A cannot be ignored. Such situations will be discussed in proceeding chapters

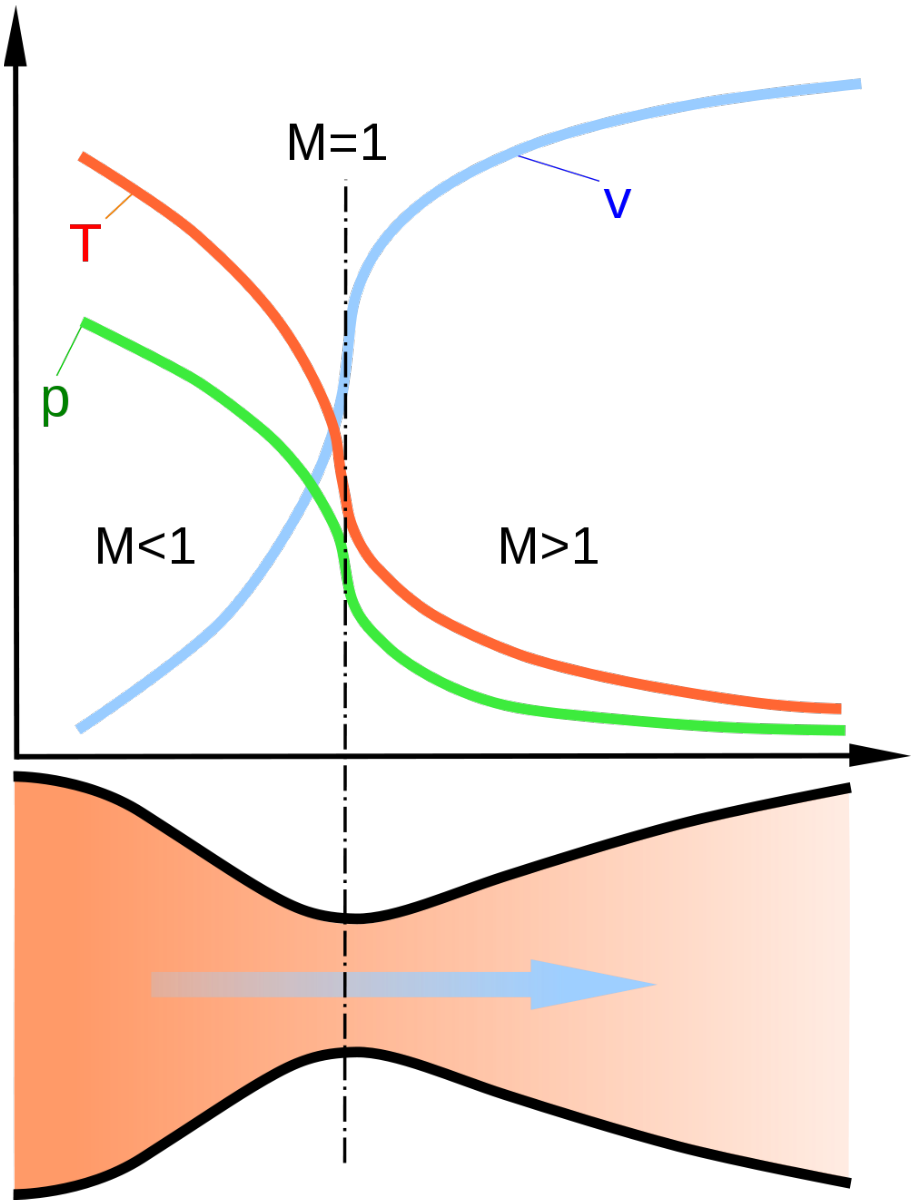

Figure 2.1: A de Laval nozzle example, used to accelerate an initially subsonic compressible flow to supersonic speeds. The subsonic flow is accelerated through a contracting cross-sectional area until it becomes supersonic, at which point the the tube expands to further accelerate the fluid. We also see how temperature and velocity change throughout this process.

2.2 Numerical Description

We now describe a numerical method for solving Equations 2.1-2.4. There are numerous numerical solvers for time-dependent PDEs, both implicit and explicit, with various orders of accuracy. Explicit schemes advance the solution in time only using information from previous time steps. A simple example is the first-order explicit upwind scheme for the linear advection equation,

$$\frac{\partial u}{\partial t} + a\frac{\partial u}{\partial r} = 0 \qquad a > 0, \tag{2.12}$$

which becomes discretized as

$$u_i^{n+1} = u_i^n - \frac{a\Delta t}{\Delta r}\left(u_i^n - u_{i-1}^n\right), \tag{2.13}$$

where the subscript i is used for the computational cell index, the superscript n identifies the time step index, Δt is the time step, and Δr is the spatial step. This scheme is first-order accurate in space and time and has the necessary restriction

$$\frac{a\Delta t}{\Delta r} \leq 1. \tag{2.14}$$

for producing stable solutions, called the the Courant-Friedrichs-Lewy (CFL) condition.

The CFL condition is necessary, but not sufficient for stability. The stability of a scheme can be checked using von Neumann analysis, where we assume the solution is composed of non-growing Fourier modes,

$$u_i^n = \lambda^n e^{Iki\Delta x}, \tag{2.15}$$

where k is the wavenumber and $I = \sqrt{-1}$. Necessary *and* sufficient restrictions on Δt and Δr for stable solutions are revealed when substituting Equation 2.15 into Equation 2.13 and saying the amplification factor λ must satisfy $|\lambda| \leq 1$

Implicit schemes, however, have a different form, using values at $t = (n+1)\,\Delta t$ in their spatial discretization(s). The implicit upwind scheme for Equation 2.12 is

$$u_i^{n+1} = u_i^n - \frac{a\Delta t}{\Delta r}\left(u_i^{n+1} - u_{i-1}^{n+1}\right). \tag{2.16}$$

Finding u_i^{n+1} now involves solving an effectively explicit matrix equation, which will be elaborated on towards the end of the chapter. Despite the added matrix computation, some implicit methods are know for being unconditionally stable (no restrictions on Δt or Δr), which is a significant advantage when high grid resolution is desired.

We will focus on describing an explicit scheme for solving Equations 2.1-2.4, primarily due to their simplicity. This will require following a specific CFL condition we will introduce. Also, due to the shock solutions seen by mass-loading a supersonic flow in Chapter 1, we will be implementing a widely-used shock-capturing method called Godunov's scheme. Shock-capturing schemes are able to handle solutions with discontinuities without numerical oscillations.

As a simple test code for modeling mass-loading in the solar wind before transitioning to and advance MHD model, we will keep our numerical method first-order accurate. Explicit schemes, such as Godunov's scheme, can be extended to much higher-order methods for much higher accuracy and computational efficiency when reducing Δt or Δr. There are several higher-order extensions and alternatives of Godunov's scheme that can be implemented and are discussed at the end of this chapter. Also provided at the end of this chapter is an overview of implicit schemes for advective problems and how they can be useful with stiff sources. For both high-order and implicit extensions, we will address advantages and disadvantages of applying them to our problem.

2.2.1 Formulating a Hyperbolic System

The basic Euler equations for conservation of mass, momentum, and energy (Equations 2.2-2.4) form a hyperbolic system in the form

$$\mathbf{U}_t + \mathbf{F}\left(\mathbf{U}\right)_r = \mathbf{S}, \tag{2.17}$$

or

$$\mathbf{U}_t + \mathbf{A}\left(\mathbf{U}\right)\mathbf{U}_r = \mathbf{S}, \tag{2.18}$$

with the latter showing its advective nature. Subscripts indicate the time and spatial derivatives being used. $\mathbf{U}$ contains our conserved variables,

$$\mathbf{U} = \begin{pmatrix} \rho \\ \rho u \\ E \end{pmatrix}, \tag{2.19}$$

$\mathbf{F}$ is our flux function,

$$\mathbf{F}(\mathbf{U}) = \begin{pmatrix} \rho u \\ \rho u^2 + p\mathbf{I} \\ u(E+p) \end{pmatrix}, \tag{2.20}$$

and $\mathbf{A}$ is the Jacobian of $\mathbf{F}$,

$$\mathbf{A}(\mathbf{U}) = \begin{pmatrix} 0 & 1 & 0 \\ \frac{1}{2}(\gamma-3)u^2 & (3-\gamma)u & \gamma-1 \\ \frac{1}{2}(\gamma-2)u^3 - \gamma\frac{uE}{\rho} & \gamma\frac{E}{\rho} - \frac{3}{2}(\gamma-1)u^2 & \gamma u \end{pmatrix}. \tag{2.21}$$

Having these equations in a conservative form such as Equation 2.17 is important for using the proper numerical scheme to find time-dependent solutions. Scheme requiring equations to be represented in conservative form are call conservative schemes. Several conservative schemes for fluid equation problems are described in Toro[46]. Among the subsets of conservative schemes are a type called finite volume methods. Finite volume methods use volume integral representations of the relevant set of equations to derive a scheme using the flux across computational cell (or volume) interfaces.

There are two parts to solving hyperbolic equations in the form of Equation 2.17. The first part is determining the particular discretization and extrapolation out to the cell boundaries. The second part is determining the flux across the boundary using the extrapolated values. In most cases the extrapolated values on either side of the interface results in a discontinuity, creating a Riemann problem. Solutions to Riemann problems determine (or estimate) the numerical flux across the cell interface. In the following section we will describe the following: an explicit discretization used by a method known as Godunov's scheme, a method for solving the Riemann problem across cell interfaces, and boundary conditions for a 1D supersonic flow. Although our main focus will be on a first-order explicit scheme, implicit schemes and higher-order methods will be discussed at the end of the chapter.

2.2.2 Godunov's Explicit Scheme

One of the most popular explicit first-order conservative finite-volume methods is Godunov's scheme (Godunov[10]). Godonuv's scheme takes non-linear systems of equations in the form of Equation 2.17 and uses a seemingly simple discretization,

$$\mathbf{U}_i^{n+1} = \mathbf{U}_i^n + \frac{\Delta t}{\Delta r}\left(\mathbf{F}_{i-\frac{1}{2}} - \mathbf{F}_{i+\frac{1}{2}}\right) + \mathbf{S}_i^n, \tag{2.22}$$

where $\mathbf{F}_{i\pm\frac{1}{2}} = \mathbf{F}\left(\mathbf{U}_{i\pm\frac{1}{2}}(0)\right)$ are the numerical fluxes on either side of the ith cell.[3] The most important part of using Godunov's Scheme (and other finite volume methods) is determining the numerical fluxes. This involves finding a solution to a Riemann problem, which will be elaborated on in the next section.

For an initial collection of data Godunov's scheme averages values over each cell, forming a piecewise constant initial condition, with a discontinuity at each cell interface (Figure 2.2). The updated values after each time step then become the new averaged values and are extrapolated out to the cell interfaces. The new left and right states are then used for finding the numerical fluxes $\mathbf{F}_{i\pm\frac{1}{2}}$.

Despite being considered a stable scheme for nonlinear hyperbolic systems, care still needs to be taken for Godunov's scheme to remain stable. With Godunov's method for Equations 2.2-2.4 the CFL condition is

$$\Delta t \leq \frac{\Delta r}{S_{\max}^n}, \tag{2.23}$$

[3] It should be noted that including source terms in this manner should not be done blindly. There is no issue with the constant sources used in our current case, but as we move to the solar corona new source terms will require additional numerical techniques to be implemented.

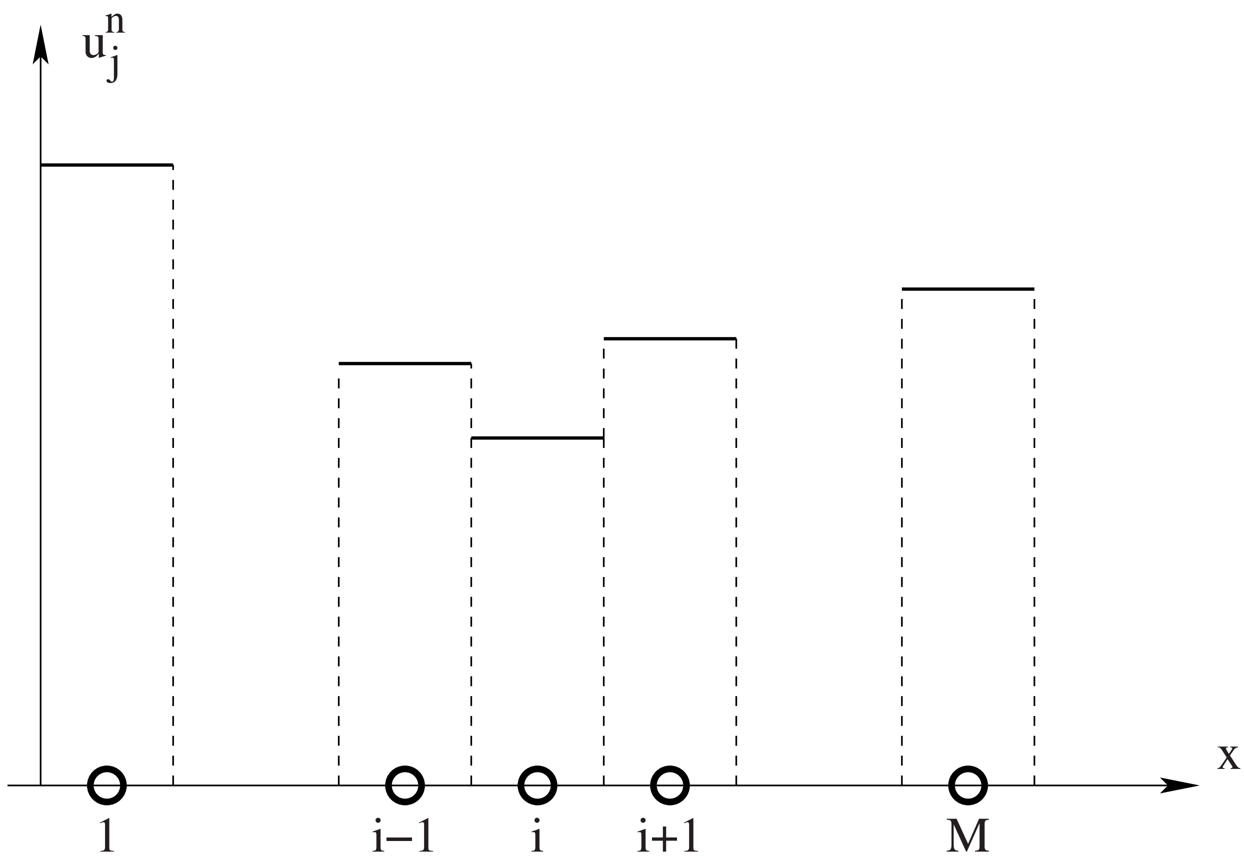

Figure 2.2: Godunov's scheme discretizes using initial condition data and cell-averaging across each cell width to create a piecewise constant set of data. Discontinuities are formed at each cell interface, requiring a solution to the Riemann problem at each one. Image is reproduced from Toro[46].

where $S^n_{\max}$ is the maximum wave speed at time t^n, and can be approximated as

$$S^n_{\max} = \max_i \{|u^n_i| + a^n_i\}, \tag{2.24}$$

where a^n_i is used for the sound speed at the ith cell and nth time step. The need for an approximation is a result of a complicated set of nonlinear waves present. Since Equation 2.24 is merely an approximation, it is not a good idea to set Δt to the right hand side. We therefore set a buffer for our time step,

$$\Delta t = 0.5 \frac{\Delta r}{S^n_{\max}}, \tag{2.25}$$

which will be used for all our 1D cases. Next, we will finally cover the Riemann problem, including what it is and a description of the Riemann solver we will use.

2.2.3 Approximate Solution to the Riemann Problem

A Riemann problem is formed when an initial condition for a hyperbolic equation, or set of equations, in the form of Equation 2.17 has a discontinuity at $r = r_0$ with left and right states $\mathbf{U}_{\mathrm{L}}$ and $\mathbf{U}_{\mathrm{R}}$ to form the initial value problem

$$\mathbf{U}(r,0) = \begin{cases} \mathbf{U}_{\mathrm{L}} & \text{if } r < r_0 \\ \mathbf{U}_{\mathrm{R}} & \text{if } r > r_0 \end{cases}. \tag{2.26}$$

Solutions can be found using wave patterns that form as a result of characteristic interactions from each side. For scalar hyperbolic equations the solutions can be relatively straightforward. For systems of equations, such as Euler's equations (Equations 2.2-2.4), the exact solution for the Riemann problem becomes excessively difficult and computationally expensive. In fact, beyond one spatial dimension the exact Riemann solution is not attainable with currently known techniques (Toro[46]). It is for these reasons that many solvers utilize approximate Riemann solvers.

Approximate Riemann solvers are extremely useful, plentiful, and less computationally expensive. However, not all conservative schemes that rely on solutions to the Riemann Problem can use approximate Riemann solutions. One example is the Random Choice Method (Chorin[7]).

Fortunately, Godunov's scheme does not rely solely on an exact solution to the Riemann problem. There are several approximate Riemann solvers and Toro[46] goes through many of them in detail. One of the most popular approximate Riemann solvers is the Roe solver, described by Roe[42], which we will cover here and proceed to use.

The general premise of the Roe solver is to take the homogeneous nonlinear hyperbolic system in Jacobian form,

$$\mathbf{U}_t + \mathbf{A}\left(\mathbf{U}\right)\mathbf{U}_r = 0, \tag{2.27}$$

and replace the Jacobian matrix $\mathbf{A}\left(\mathbf{U}\right)$ with a constant matrix $\tilde{\mathbf{A}}\left(\mathbf{U}_{\mathrm{L}},\, \mathbf{U}_{\mathrm{R}}\right)$, dependent on the left and right states at the cell interfaces. The resulting approximate Riemann problem for the linear system

$$\mathbf{U}_t + \tilde{\mathbf{A}}\mathbf{U}_r = 0 \tag{2.28}$$

is then solved with an exact Riemann solver. In determining the $m \times m$ matrix $\tilde{\mathbf{A}}$, it must satisfy the following properties:

- Real eigenvalues and m linearly independent eigenvectors
- The Jacobian and $\tilde{\mathbf{A}}$ must be consistent ($\tilde{\mathbf{A}}\left(\mathbf{U},\, \mathbf{U}\right) = \mathbf{A}\left(\mathbf{U}\right)$)
- Quantities across discontinuities must be conserved ($\mathbf{F}\left(\mathbf{U}_{\mathrm{R}}\right) - \mathbf{F}\left(\mathbf{U}_{\mathrm{L}}\right) = \tilde{\mathbf{A}}\left(\mathbf{U}_{\mathrm{R}} - \mathbf{U}_{\mathrm{L}}\right)$).

To find $\tilde{\mathbf{A}}$, Roe[42] chose a vector $\mathbf{Q}$ such that $\mathbf{U}$ and $\mathbf{F}$ could be expressed in terms of $\mathbf{Q}$. Two additional matrices $\tilde{\mathbf{B}}$ and $\tilde{\mathbf{C}}$ are found such that

$$\Delta\mathbf{U} = \tilde{\mathbf{B}}\Delta\mathbf{Q} \tag{2.29}$$

and

$$\Delta\mathbf{F} = \tilde{\mathbf{C}}\Delta\mathbf{Q}. \tag{2.30}$$

$\tilde{\mathbf{A}}$ can then be found when Equation 2.29 and Equation 2.30 are combined to get

$$\Delta\mathbf{F} = \left(\tilde{\mathbf{C}}\tilde{\mathbf{B}}^{-1}\right)\Delta\mathbf{U}, \tag{2.31}$$

where

$$\tilde{\mathbf{A}} = \tilde{\mathbf{C}}\tilde{\mathbf{B}}^{-1}. \tag{2.32}$$

There exists a very convenient algorithm for finding $\tilde{\mathbf{B}}$ and $\tilde{\mathbf{C}}$ using the eigenspace of $\mathbf{A}$, along with the left and right states, described in Toro[46], which we will be utilizing for our 1D problems.

2.2.4 Boundary Conditions

The boundary conditions need to be chosen such that the fluid interacts with the domain boundaries appropriately. Common types of boundary conditions include transmissive and reflective. Transmissive boundary are those that allow the flow through, as if no boundary existed. Reflective boundaries act as a physical boundary that blocks the flow from leaving the computational domain, often resulting in disturbances being reflected back.

For the uniform supersonic solar wind in this chapter, we define transmissive boundary conditions for inflow and outflow. The upwind boundary it determined by defining a fictitious cell, or ghost cell, next to the most upwind cell. If the solar wind is uniform, then the upwind ghost cell takes on the values of its neighbor. If the velocity of the most downwind cell remains supersonic, then no ghost cell is required, as updated values will be determined by the upwind cell.

2.3 Mass-Loading in a Uniform Solar Wind

We now have a feasible numerical scheme for solving Equations 2.2-2.4 (Equation 2.1 can be updated using the numerical fluxes calculated for Equations Equations 2.2-2.4). This section will focus on our first solutions from numerically solving the 1D hydrodynamic equations with a mass-loading term. Special care will be taken to verify the predicted nozzle effects describe earlier in the chapter.

2.3.1 Mass-Loading Setup

Prior to presenting solutions of a mass-loaded solar wind, we need to set up our one-dimensional grid, solar wind parameters, and source terms. Our computational domain will cover the interval $0\,\mathrm{km} \leq r \leq 10^5\,\mathrm{km}$, and be composed of 1000 spatial steps. This is smaller than the domain used by Biermann et al.[4] by about an order of magnitude, but is still fitting for a general mass-loading event in the general heliosphere. Our undisturbed solar wind parameters (denoted with subscript 0) will be similar to those in BIermann et al.[4], which mimic the solar wind at 1 AU.[4] The solar wind parameters are then defined as

$$\begin{aligned} u_0 &= 400\,\mathrm{km/s} \\ \rho_0 &= 3\,m_p \\ p_0 &= 3.8 \times 10^{-11}\,\mathrm{dyn/cm^2}. \end{aligned}$$

From our defined solar wind density, our number density and mean mass become

$$\begin{aligned} n_0 &= 6\,\mathrm{cm}^{-3} \\ \mu_0 &= 0.5\,m_p, \end{aligned}$$

since we are using a single-fluid model.

For our source terms we will assume the particle velocities are negligible relative to the solar wind velocity, allowing us to define $u_d = 0$. This makes the our only non-zero source term the mass-loading factor P_{ml} in the mass conservation equation. Additionally, we will only use a small region of our domain defined by $1 \times 10^4\,\mathrm{km} \leq r \leq 3 \times 10^4\,\mathrm{km}$ for P_{ml} to be non-zero. This will act as a band of potential pick-up ions or, in terms of effective area, a contracting cross-sectional area the solar wind will see.

[4] These values are for 1AU in the Sun's equatorial plane. The solar wind varies with respect to latitude, which will discussed in a later chapter.

2.3.2 Mass-Loading Results

We now check to ensure a mass-loaded wind behaves as predicted by theory presented earlier. In Figure 2.3 we have a new solar wind steady-state by solving the Equations 2.1-2.4 as previously described, using $P_{ml} = 6.5 \times 10^{-25}\,\mathrm{g\,cm^{-3}\,s^{-1}}$.[5] We see a quick deceleration and shock down to subsonic speeds, followed by reacceleration back to supersonic speeds at the mass-loading region's outer edge. Additionally, the mean mass increases steadily and levels off downwind, reflecting the increased concentration of pick-up ions as the solar wind passes through the mass-loading region. This validates the predicted effects for the mass-loading contributions to effective area, which we can calculate for this steady-state and plot against our results to show a decreasing A_{eff} in the mass-loading region (Figure 2.4).

Note in Figure 2.3 that our mass-loading factor seems almost high enough to stop the solar wind completely. This begs the question for if the solar wind can in a sense be broken with an extremely high mass-loading factor. When P_{ml} from our first results was increased by an order of magnitude, this resulted in a nearly unchanged Mach number profile, but an extremely low downwind velocity and high mean mass. This shows incredible resilience for the mass-loading region to reaccelerate the wind back to supersonic speeds. The extent of testing with a large P_{ml} is unfortunately limited by our computational power, as it creates a much stricter CFL condition due to an extremely high sound speed at a point just after the shock.

2.4 Higher-Order Methods

The numerical method used here is of course only an explicit first-order accurate scheme, chosen to provide a simple example of a numerical solver for fluid equations. There exist several high-order numerical schemes for solving Equations 2.1-2.4, many of which are described in detail in Toro[46]. We will provide a brief overview of higher-order extensions and alternatives to Godunov's first-order scheme. We will begin with two basic conservative solvers capable of replacing Godunov's

[5] Several values were tested for P_{ml}. The value for P_{ml} in our presented results was chosen to demonstrate a severely mass-loaded wind.

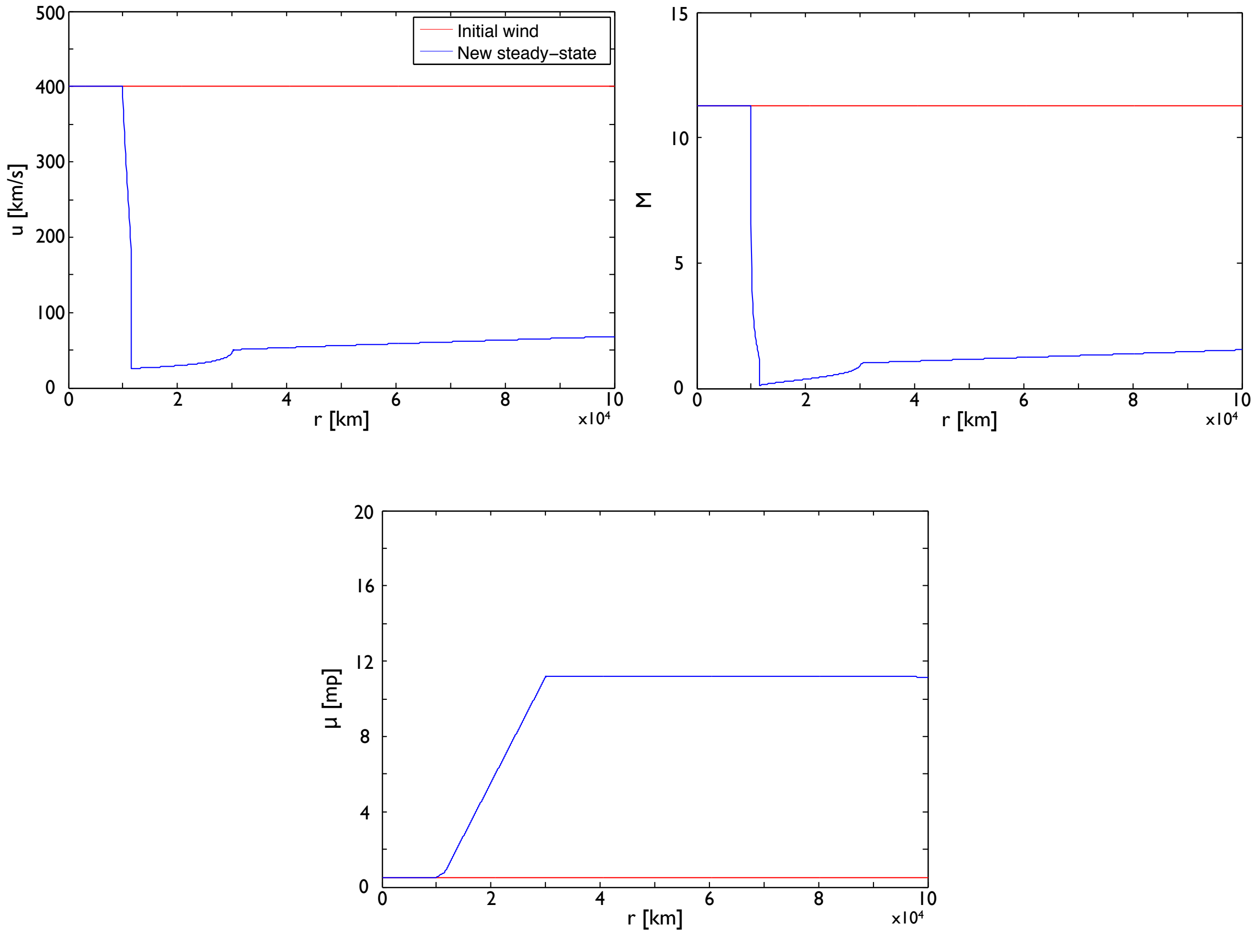

Figure 2.3: New steady-states generated from mass-loading a uniform solar wind on the interval $1 \times 10^4\,\text{km} \leq r \leq 3 \times 10^4\,\text{km}$. Shown are the solar wind velocity, mach number, and mean molecular weight. The mach number shows that the solar wind becomes supersonic at the end of the mass-loading region.

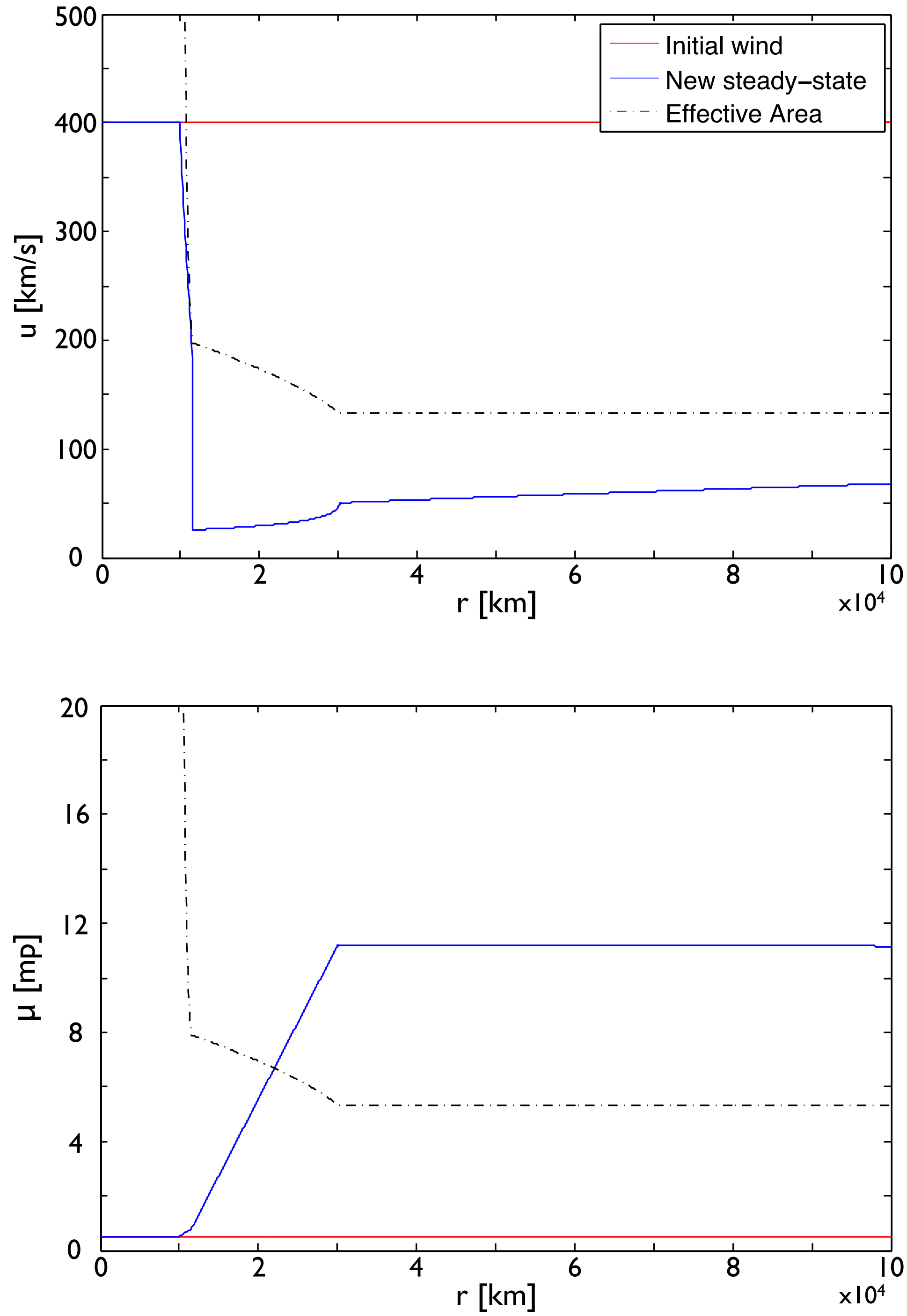

Figure 2.4: The effective area calculated for steady-states in Figure 2.3, composed primarily of a contracting area across the mass-loading region, due to dust particles being loaded into the solar wind.

scheme that actually do not rely on solutions to the Riemann problem, followed by more modern methods relying on Total Variation Diminishing (TVD) schemes.

Earlier, we jumped straight in to using Godunov's conservative method, which relies on solutions to the Riemann problem to determine the intercell flux. There are two methods, typically considered in conjunction with Godunov's scheme for fluid equations. The first is the Lax-Friedich scheme, which is based on splitting the u_i^n term in the time derivative as $\frac{1}{2}\left(u_{i+1}^n + u_{i-1}^n\right)$. It is second-order accurate in space, but only first-order accurate in time. It also does not require solving the Riemann problem. One issue with the Lax-Friedrich scene is much higher numerical diffusion present, one of two issues we do not want too much of in fluid problem.

The second method is the Lax-Wendroff scheme, described by Lax and Wendroff[25], which is based on both upwind and downwind information in its discretization. The Lax-Wendroff scheme has the advantages of being second order in both time and space and also not relying on solving a Riemann problem. The main disadvantage of this method is the presence of oscillations near high gradients or discontinuities, which is the other numerical effect we do not want to see in solutions to Equations 2.1-2.4. Such oscillations are actually a common issue with high-order linear methods (Toro[46]; Godunov[10]), which has led to modern methods using TVD schemes.

TVD schemes, described by Harten[15], are based on imposing constraints on discretization coefficients, allowing monotonicity to be preserved, a property higher-order linear methods lack (Godunov[10]). Resulting TVD criteria is then used with pre-existing higher-order schemes to make them monotone, a property also preventing the growth and creation of local spatial extrema over time and eliminating numerical oscillations near high gradients and discontinuities. Several higher-order schemes shown to have TVD versions include the Weight Average Flux (WAF) method (Toro[45]) and a family of schemes called Monotone Upstream-centered Schemes for Conservation Laws (MUSCL).

MUSCL-type schemes are a natural higher-order extension of Godunov's scheme. Recall from Figure 2.2 that Godunov's scheme relies on cell-averaged values forming piecewise constant data, along with solutions to the intercell Riemann problems. MUSCL-type schemes instead rely on piecewise linear data extrapolated out from the cell-center average values (van Leer[50]), as illustrated in Figure 2.5. One of the widely-used MUSCL-type schemes is the MUSCL-Hancock Method (MHM). Others include the Piecewise Linear Method (PLM) (Colella[8]), Generalized Riemann Problem (GRP) method (Ben-Artzi and Falcovitz[3], applied to Euler's equations), and Slope-Limiter Centered (SLIC) schemes. This is only a brief overview of the higher-order methods mentioned so far. More detailed descriptions are provided in Toro[46] and references therein.

Many of the current higher-order methods used in solar wind and fluid modeling are still based on higher-order extensions of the Roe-based Godunov's scheme, particularly MUSCL-type schemes. A related area of study still heavily researched is the development of flux (or slope) limiters, which are used to construct TVD schemes for higher-order MUSCL-type methods. One particular study by Kurganov and Tadmor[24] focuses on developing a high-order centered scheme for convection-diffusion equations with the use of a flux limiter called minmod (also used in computational MHD), with examples for higher dimensions.

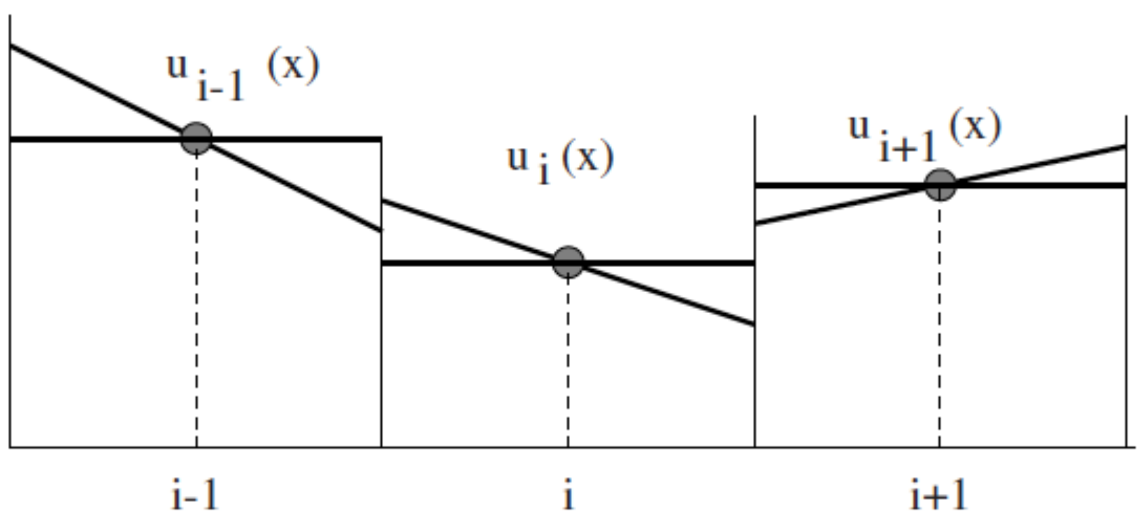

Figure 2.5: MUSCL-type schemes discretize using initial condition data and cell-averaging across each cell width to create a piecewise linear set of data. Discontinuities are formed at each cell interface, once again requiring a solution to the Riemann problem at each one. Image is reproduced from Toro[46].

2.5 Implicit Schemes

Our focus in this chapter was also on an *explicit* numerical scheme for solving Equations 2.1-2.4. Using Godunov's scheme required the selection of Δt to adhere to its CFL condition to maintain stability. There exist families of implicit schemes that are stable, eliminating or reducing restrictions on the time step Δt. In this section we will discuss some of these methods for finite differencing and their advantages with source terms, but also a disadvantage when using Roe-based methods.

We return to the linear advection equation

$$\frac{\partial u}{\partial t} + a\frac{\partial u}{\partial r} \quad = \quad 0, \tag{2.33}$$

which can be solved with an upwind method, discretizing $\frac{\partial u}{\partial r}$ as $\frac{u_{i+1}^n - u_i^n}{\Delta r}$ for $a < 0$ and as $\frac{u_i^n - u_{i-1}^n}{\Delta r}$ for $a > 0$. It still adheres to a CFL condition, requiring Δt to be chosen such that characteristics are contained in the domain of dependence. An implicit scheme is formed by using $n+1$ data discretization of $\frac{\partial u}{\partial r}$,

$$u_i^{n+1} \quad = \quad u_i^n - \frac{a\Delta t}{\Delta r}\left(u_i^{n+1} - u_{i-1}^{n+1}\right), \tag{2.34}$$

where $a > 0$ in this example. The scheme is now unconditionally stable and requires solving the effectively explicit matrix equation,

$$\mathbf{A}\mathbf{x} \quad = \quad \mathbf{b}, \tag{2.35}$$

where $\mathbf{A}$ is a lower bidiagonal matrix and

$$\mathbf{x} \quad = \quad \left(u_0^{n+1},\, u_1^{n+1}, \ldots,\, u_I^{n+1}\right)^\top \tag{2.36}$$

$$\mathbf{b} \quad = \quad \left(u_0^n + \frac{a\Delta t}{\Delta r}u_{-1}^{n+1},\, u_1^n, \ldots,\, u_I^n\right)^\top. \tag{2.37}$$

$I+1$ spatial cells and left ghost cell u_{-1}^{n+1} are used. The the scheme now relies solving Equation 2.35. For bidiagonal matrix $\mathbf{A}$, this is done efficiently with back-substitution.

Such an implicit method can be extended to finite differencing with Equation 2.17,

$$\mathbf{U}_i^{n+1} \quad = \quad \mathbf{U}_i^n + \frac{\Delta t}{\Delta r}\left[\mathbf{F}\left(\mathbf{U}_{i-1}^{n+1}\right) - \mathbf{F}\left(\mathbf{U}_{i+1}^{n+1}\right)\right] + \mathbf{S}_i^{n+1}, \tag{2.38}$$

no longer resulting in a simple bidiagonal matrix **A**. An extension to the Roe-based Godunov scheme would seem like a logical next step, however, an implicit scheme with Roe's approximate Riemann solver is very computationally costly and not widely used. A Roe-based MHD solver that will be introduced in Chapter 4 does have an implicit option, but only for source terms.

Implicit schemes are also useful when solving a stiff system, which is a system of equations with a source requiring a much smaller time step to maintain a stable solution than the rest of the system. Iserles[19] shows several examples of using implicit methods for stiff ODEs. This situation will arise in the next chapter when we add a diffusive term to our Euler equations, which will require a much smaller time step than the CFL condition for Godunov's scheme.

A common implicit scheme used for diffusive problems is the Crank-Nicolson scheme. This scheme is demonstrated in Morton and Mayers[32] with the heat equation, where it is second-order accurate in time and space. For a basic diffusion equation,

$$\frac{\partial u}{\partial t} = \frac{\partial^2 u}{\partial t^2}, \tag{2.39}$$

the Crank-Nicolson scheme discretizes the diffusion term both explicitly and implicitly and averages them,

$$u_i^{n+1} = u_i^n - \frac{\Delta t}{2\Delta r^2}\left(u_{i+1}^n - 2u_i^n + u_{i-1}^n\right) - \frac{\Delta t}{2\Delta r^2}\left(u_{i+1}^{n+1} - 2u_i^{n+1} + u_{i-1}^{n+1}\right). \tag{2.40}$$

Again, Crank-Nicolson is unconditionally stable for solving Equation 2.39 and results in the linear system $\mathbf{Ax} = \mathbf{b}$, where $\mathbf{A}$ is now a tridiagonal matrix, that can be solved with the Thomas algorithm.

The methods in the these last two sections are merely brief examples in the use of higher-order and implicit schemes for Equations 2.2-2.4 and we will continue in the next chapter with finding solutions in the solar corona with the first-order explicit Godunov's scheme. A diffusive term will be introduced, but a different method, called source splitting, is used to solve the resulting stiff system.

Chapter 3

Mass-Loading for a Spherically Symmetric Coronal Wind

With the safety of a uniform 1D solar wind behind us,[1] we now delve into the more complicated solar corona region, extending from the top of the chromosphere near the solar surface, out to tens of solar radii $R_\odot$ from the Sun. The solar corona is known for its incredible temperatures, orders of magnitude hotter than the solar surface, and for being the launch point for solar storms such as coronal mass ejections. As a result, the solar corona has spawned a significant subfield in solar physics, with several mysteries yet to be solved. In moving from the solar wind model used in the previous chapter to a model for the solar corona, our main challenge is adding several physical processes, many of which are well-understood and some of which are still puzzling to solar physicists.

In this chapter we will cover the basic coronal wind modeling and acceleration models leading up to the 1D Euler equations with the appropriate source terms. We will then make the necessary numerical adjustments for solving the Euler equations in the solar corona. Solving these equations with mass-loading sources will involve various cases for subsonic and supersonic wind locations. Last, we will discuss our 1D mass-loading results for the coronal wind and explain the need for moving to a less simple but more accurate coronal wind model.

[1] Or more accurately, downwind of us.

3.1 Establishing a 1D Coronal Wind Model

We have already established and 1D hydrodynamic solar wind model in the previous chapter. For distances closer to the Sun, as with the case of the solar corona, and for the spatial scales we are dealing with, the wind is no longer flowing in a single Cartesian direction, but radially our from the Sun (Parker[33]). In a physical sense this no longer makes the model 1D in space, but assuming spherical symmetry makes it mathematically so, with r as the spatial variable. This section will begin with describing the original Parker solution of the coronal wind and work up to establishing a physical transonic wind (a wind traveling from the solar surface and becoming sup sonic soon after).

3.1.1 The Parker Solution

A 1D starting point for modeling the transonic coronal wind is to begin with a very basic hydrodynamic model, even more so than Equations 2.2-2.4. Meyer-Vernet[31] shows, in looking for an outflowing steady-state solution, that assuming a purely adiabatic flow ($\gamma = 5/3$) in which there is no heat exchange, a wind cannot be generated. On the opposite end of the spectrum, assuming an isothermal flow ($\gamma = 1$) where heat transfers at an infinite rate makes the temperature constant, a wind is generated outflowing from the Sun but is still nonphysical in certain aspects to be explained shortly.

For both the adiabatic and isothermal flows Bernoulli's principle is used,

$$\frac{u^2}{2} + \frac{\gamma}{\gamma - 1}\frac{k_b T}{\mu} - \frac{M_\odot G}{r} = \text{constant} \quad \text{(adiabatic)} \tag{3.1}$$

$$\frac{u^2}{2} + \frac{k_b T}{\mu}\ln\rho - \frac{M_\odot G}{r} = \text{constant} \quad \text{(isothermal)}, \tag{3.2}$$

where T, k_b, $M_\odot$, and G are temperature, Boltzmann's constant, solar mass, and the gravitational constant, respectively. Each equation is the conservation of mass and momentum integrated for a steady flow, with the equation of state $p = \rho k_b T/\mu$ to relate pressure with the other dependent variables. The left sides of Equations 3.1-3.2 are constant along streamlines (extending radially in the 1D case) and equal the energy per unit mass. Meyer-Vernet[31] shows at large distances in the adiabatic case

$$u^2/2 \simeq \text{constant}, \tag{3.3}$$

which is negative when using realistic coronal wind values in Equation 3.1, meaning no wind can be produced. Performing the same on Equation 3.2, it is found that at large distances

$$u \simeq \sqrt{4a^2 \ln r^2}, \tag{3.4}$$

where the sound speed a is defined as

$$a = \sqrt{\frac{k_b T}{\mu}}. \tag{3.5}$$

Since the right side of Equation 3.4 is always positive, then an isothermal solar wind exists.

Using Equation 3.2 with some fixed T and allowing the coronal base velocity to vary, an entire family of solutions to the solar wind is found. Figure 3.1, taken from Parker[34], shows the set of solutions. The critical radius $r = r_C$ is a crucial value in the solution space, as it is the distance where either $du/dr = 0$ or the wind equals the sound speed ($u = a$). In the latter case $r = r_C$ is called the sonic point. The solution passing through the sonic point and from region A to region B represents the transonic Parker solution, often used as an initial condition for more realistic solar wind models. The nonphysical issue facing this model is that $u \to \infty$ as $r \to \infty$, which would require infinite energy.

The Parker solution is a great starting point, as it does generate a transonic coronal wind with the right solar parameters. The next step is to make it a physically possible solar wind, by keeping the kinetic energy at large distances bounded.

3.1.2 Transition to a Physical Transonic Solar Wind

There are two typical solutions used to address the problems in Parker's solution. First, a polytropic wind can be used, where instead of simply using either $\gamma = 1$ or $\gamma = 5/3$ a varying adiabatic index is used to accommodate the spatial-dependence of heat transfer. The problem

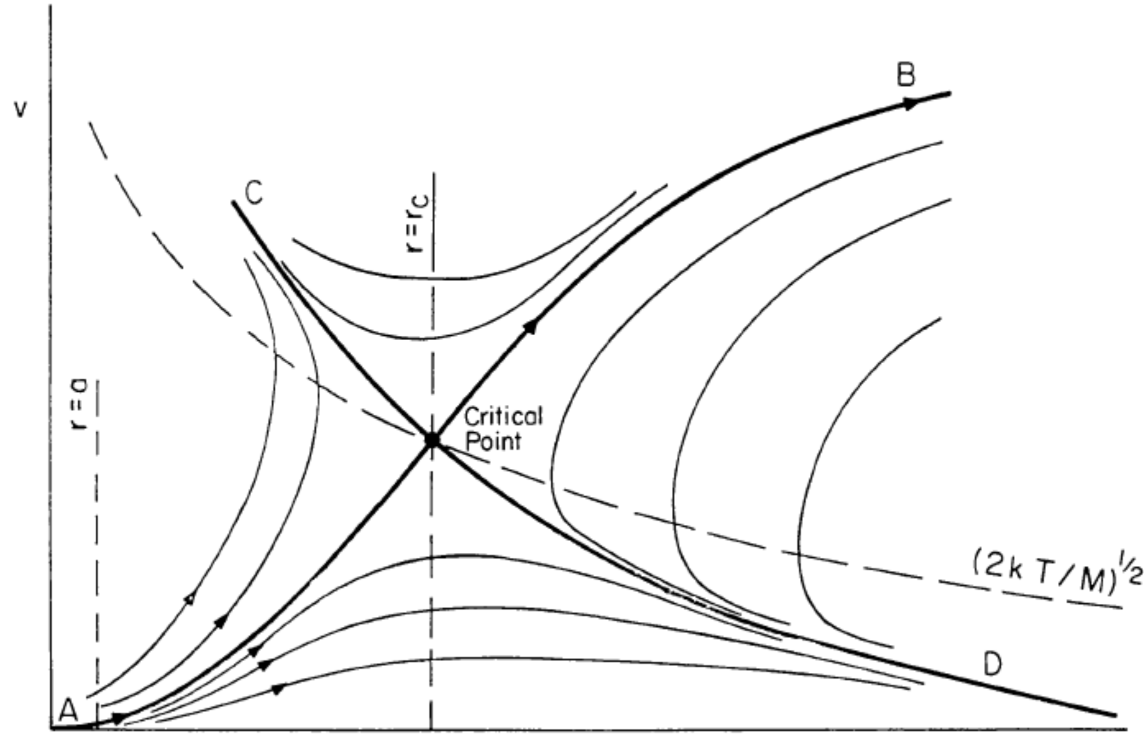

Figure 3.1: The solution topology for the radial velocity of the solar wind, originally derived by Parker[34], which includes the one transonic wind solution. The dashed curve shows how the sound speed a changes with respect to r, where M is used for the proton mass in this case. Image is reproduced from Parker[34].

with this solution, as mentioned by Meyer-Vernet[31], is that it takes multiple physical processes occurring in the solar wind and hides them in a single parameter. The second option is to include extra physical processes in the hydrodynamic equations. We have reviewed several papers using this second option in their 1D hydrodynamic models (Withbroe[51]; Pinto et al.[35]; Riley et al.[41]), with the necessary included physical processes being heat transfer from conduction, radiative losses, and some form of coronal heating.

Taking the latter solution to Parker's problem, we can modify Equations 2.1-2.4 to include not only additional source terms necessary to accelerated the coronal wind in a physical manner, but also the spherical symmetry with an area expansion $A = r^2$. The new set of equations becomes

$$\frac{\partial (An)}{\partial t} + \frac{\partial (Anu)}{\partial r} = AS_0 \tag{3.6}$$

$$\frac{\partial (A\rho)}{\partial t} + \frac{\partial (A\rho u)}{\partial r} = AS_1 \tag{3.7}$$

$$
\begin{aligned}
\frac{\partial\left(A\rho u\right)}{\partial t}+\frac{\partial\left(A\rho u^{2}\right)}{\partial r}+A\frac{\partial p}{\partial r} &= AS_{2} && (3.8)\\
\frac{\partial\left(AE\right)}{\partial t}+\frac{\partial}{\partial r}\left[Au\left(E+p\right)\right] &= AS_{3}. && (3.9)
\end{aligned}
$$

The partial derivatives in Equations 3.6-3.9 can be expanded and the area terms moved to the right side to get the alternative form

$$
\begin{aligned}
\frac{\partial n}{\partial t}+\frac{\partial}{\partial r}\left(nu\right) &= S_{0}-\frac{A'}{A}nu && (3.10)\\
\frac{\partial \rho}{\partial t}+\frac{\partial}{\partial r}\left(\rho u\right) &= S_{1}-\frac{A'}{A}\rho u && (3.11)\\
\frac{\partial \rho u}{\partial t}+\frac{\partial}{\partial r}\left(\rho u^{2}\right)+\frac{\partial p}{\partial r} &= S_{2}-\frac{A'}{A}\rho u^{2} && (3.12)\\
\frac{\partial E}{\partial t}+\frac{\partial}{\partial r}\left[u\left(E+p\right)\right] &= S_{3}-\frac{A'}{A}\left[u\left(E+p\right)\right], && (3.13)
\end{aligned}
$$

where

$$A' = \frac{dA}{dr}. \qquad (3.14)$$

For the coronal wind, additional source terms $\mathbf{S}_{cor}$ must be introduced, making $\mathbf{S}=\mathbf{S}_{cor}+\mathbf{S}_{d}$.

Necessary source terms near the Sun consist primarily of gravity and heat transfer. While gravity is straightforward, heat transfer is not, as it must be split into multiple contributions. There needs to be a heat conduction source, as well as a term for radiative losses. The other heat transfer contribution is coronal heating. Modeling coronal heating, however, is an entire field on its own, since the physics behind heating the corona are still not well-understood. Figuring out how to model coronal heating is not a focus of this research and we will simply use the same power law model presented by Pinto et al.[35]. The coronal sources $\mathbf{S}_{cor}=\left(S_{cor1}, S_{cor2}, S_{cor3}, S_{cor4}\right)^{\top}$ are then

$$
\begin{aligned}
S_{cor1} &= 0 && (3.15)\\
S_{cor2} &= 0 && (3.16)\\
S_{cor3} &= -\rho\frac{GM_{\odot}}{r^{2}} && (3.17)\\
S_{cor4} &= -\rho u\frac{GM_{\odot}}{r^{2}}+\nabla\cdot\left(\mathbf{Q}_{cond}-\mathbf{Q}_{cor}\right)-n^{2}\Phi\left(T\right), && (3.18)
\end{aligned}
$$

where we are now using the spherical divergence operator, along with $\mathbf{Q}_{cond}$, $\mathbf{Q}_{cor}$, and $\Phi\left(T\right)$, which are the collisional Spitzer heat flux, coronal heat flux, and radiative loss function, respectively. The former two terms are defined as

$$\mathbf{Q}_{cond} = \kappa_0 T^{5/2} \frac{\partial T}{\partial r} \hat{\mathbf{r}} \tag{3.19}$$

$$\mathbf{Q}_{cor} = Q_0 \left(\frac{R}{r}\right)^{3/2} \hat{\mathbf{r}}, \tag{3.20}$$

where $\kappa_0 = 10^{-6}$ and $Q_0 = 3 \times 10^5$ (in cgs). Collisional heat conduction becomes less necessary beyond $5\,R_\odot$. As a result, it will multiplied by the following piecewise function:

$$\Gamma\left(r\right) = \begin{cases} 1 & r \leq 5\,R_\odot \\ 2 - \frac{1}{5\,R_\odot} r & 5\,R_\odot < r < 10\,R_\odot \\ 0 & r \geq 10\,R_\odot \end{cases} . \tag{3.21}$$

Within $5\,R_\odot$ the collisional heat conduction term will be used normally, but will be eliminated outside $10\,R_\odot$, with $5\,R_\odot < r < 10\,R_\odot$ being used as a transition region. Radiative losses is a much more complicated function and is plotted in Meyer-Vernet[31] from observational data, accompanied with a primitive formula model for $\Phi\left(T\right)$. We instead use the model from Pinto et al.[35] due to its ability to model observations better at low temperatures.

3.2 Solving for a 1D Steady-State Coronal Wind

With the appropriate set of equations for a spherically symmetric coronal wind established, we move to obtaining an initial steady-state for a mass-loaded coronal wind. This section will cover amendments to our numerical methods used for a uniform 1D solar wind and present a steady-state coronal wind solution. The resulting effective area curve will also be compared with that of an expanding cometary atmosphere in Gombosi et al.[11].

3.2.1 Numerical Description

We still rely on the same first-order Godunov method used with Roe's approximate Riemann solver from the previous chapter. However, the solar corona presents new challenges with obtaining a stable and physical solution. First, our source term $\mathbf{S}$ is no longer a constant term, but is now dependent on radial distance r in each coronal source term, as well as on time-dependent wind parameters. Second, though we can set our outflow boundary such that the solar wind passing through it is supersonic, the inner boundary is completely different from the previous chapter, with the coronal wind beginning at rest. These are the two numerical issues we will address.

3.2.1.1 Source Term Splitting

Our source term $\mathbf{S} = \mathbf{S}_d$ in the previous chapter only dealt with constant terms, which did not impact our stability condition. Even with the introduction of the coronal source terms $\mathbf{S}_{cor}$, most are only spatially-dependent, which again is not a problem to the stability of the scheme we are using. The diffusive heat conduction term, however, does pose a problem, as it causes our system to become stiff.

When solved numerically, stiff equations have an extremely restrictive time step requirement in order to keep the solution stable (Iserles[19]). To show that the heat conduction term is making our system stiff, we first note that by using $p = \rho k_b T/\mu$ and $\gamma = \frac{5}{3}$, $\frac{\partial E}{\partial t}$ can be expanded,

$$\begin{aligned}
\frac{\partial E}{\partial t} &= \frac{\partial}{\partial t}\left(\frac{1}{2}\rho u^2 + \frac{3}{2}p\right) && (3.22)\\
&= \frac{\partial}{\partial t}\left(\frac{1}{2}\rho u^2\right) + \frac{\partial}{\partial t}\left(\frac{3\rho}{2\mu}k_b T\right) && (3.23)\\
&= \left(\frac{1}{2}u^2 + \frac{3}{2}\frac{k_b T}{\mu}\right)\frac{\partial \rho}{\partial t} + \rho u \frac{\partial u}{\partial t} + \frac{3}{2}\frac{\rho k_b}{\mu}\frac{\partial T}{\partial t}. && (3.24)
\end{aligned}$$

Substituting into Equation 3.13 and isolating the partial temperature terms, we get the diffusive contribution to the system,

$$\frac{\partial T}{\partial t} = \frac{4}{21}\frac{\mu \kappa_0}{\rho k_b}\frac{1}{r^2}\frac{\partial}{\partial r}\left(r^2 \frac{\partial T^{7/2}}{\partial r}\right). \tag{3.25}$$

We call

$$c = \frac{4\mu\kappa_0}{21\rho k_b} \tag{3.26}$$

and discretize similarly to the heat equation in Morton and Mayers[32] to get

$$\frac{\partial T_i}{\partial t} \approx 3c_i \frac{r^2_{i+\frac{1}{2}} T^{7/2}_{i+1} - \left(r^2_{i+\frac{1}{2}} + r^2_{i-\frac{1}{2}}\right) T_i^{7/2} + r^2_{i-\frac{1}{2}} T^{7/2}_{i-1}}{\left(r^2_{i+\frac{1}{2}} + r_{i+\frac{1}{2}} r_{i-\frac{1}{2}} + r^2_{i-\frac{1}{2}}\right) \Delta r^2}. \tag{3.27}$$

Assuming forward difference in time is still used, the condition on our time step becomes

$$\Delta t \leq \frac{\Delta r^2}{\max_i \left\{6 c_i T_i^{5/2}\right\}}, \tag{3.28}$$

which was also used by Filbet et al.[9]. If we take $S_{\max}$ from the CFL condition for Godunov's Scheme and assume

$$S_{\max} \sim 100\,\mathrm{km/s}, \tag{3.29}$$

and then take $6cT^{5/2}$ from Equation 3.28 and assume approximate inner boundary conditions for density and temperature to be

$$\rho \sim 10^{-16}\,\mathrm{g/cm^3} \tag{3.30}$$

$$T \sim 10^6\,\mathrm{K}, \tag{3.31}$$

then for $\Delta r \sim 10^{-2}\,\mathrm{R}_\odot$

$$\frac{\Delta r^2 S_{\max}}{\Delta r\, 6cT^{5/2}} \sim 0.1. \tag{3.32}$$

This ratio only further decreases with decreasing Δr. The temperature and density values used are a best case scenario, since density decreases much faster than temperature as r increases. Even though our advection portion requires a more reasonable time step, the heat conduction term causes unnecessary computational work for our advective solver.

The solution to this conundrum is called source splitting (Toro[46]). The idea is to split the system into an advective part,

$$\mathbf{U}_t + \mathbf{F}\left(\mathbf{U}\right)_r = 0, \tag{3.33}$$

and a source part,

$$\mathbf{U}_t = \mathbf{S}. \tag{3.34}$$

We can advance Equation 3.33 one time step Δt, as determined by the CFL condition for Godunov's Scheme, and proceed to advance Equation 3.34 to get our updated state $\mathbf{U}^{n+1}$. The stiff source term problem is then resolved by taking the advective time step and dividing it into sub-time steps Δt_{src} such that Δt_{src} satisfies Equation 3.28. For each advancement of the advective part, we actually advance the source part several Δt_{src} until an overall Δt advancement is accomplished.

Additionally, with source splitting, there is a requirement for the overall scheme to be a specific order of accuracy. The methods for advancing both the advective and source parts must be at least that specified order. Currently, we are using first-order schemes. Should we choose to use a second-order scheme, as described in the previous chapter, our method for advancing the source part would need to be second-order as well. Another requirement for second-order source splitting is to advance the source part half a time step Δt, the adjective part a full time step, and the source part a half time step once more.

3.2.1.2 Boundary Conditions

For our outer boundary condition, we can use the same transparent boundary condition described in the previous chapter as long as the outflow is supersonic. This is accomplished by placing our outer boundary far enough away from the sonic point. Previous studies (Vernet-Meyer[31]; Pinto et al.[35]; Withbroe[51]) have shown the sonic point to be at about $4-5\,R_\odot$ from the solar surface. We will then ensure our outer boundary is placed several $R_\odot$ out from $5\,R_\odot$ by choosing $10\,R_\odot$ for all our 1D hydrodynamic cases.

The inner boundary is not so simple. It will need to absorb the wind without any disturbances reflecting back. We take the boundary between the leftmost cell r_0 and ghost cell r_{-1} to be $r = R_\odot$, where the inner boundary values $\rho = \rho_0$, $u = 0$, and $p = p_0$ are defined. We then make the flux at the boundary close to zero by assuming $\frac{\partial \rho}{\partial r} = \frac{\partial p}{\partial r} = 0$ between r_0 and r_{-1} and setting $u_{-1} = -u_0$ (Lugaz et al.[26]).

3.2.2 Steady-State Results

We are nearly set to generate a 1D steady-state coronal wind. The one selection yet to be made it the spatial step size Δr. Making Δr arbitrarily small, while decreasing error in the solution, requires significantly more computational resources. With the computational resources used, the CPU time for finding a steady-state solution on our selected domain nears days for N greater than 2000. However, for low N (large Δr) we not only get a less accurate solution, but also get an accreting wind near the inner boundary (Figure 3.2, for example), which we try to avoid with a 1D hydrodynamic model.

The significant rise in CPU time can be seen when varying N. Table 3.1 shows how the ratio between time step Δt and sub-time step Δt_{src} varies with N. On top of an increased CPU time

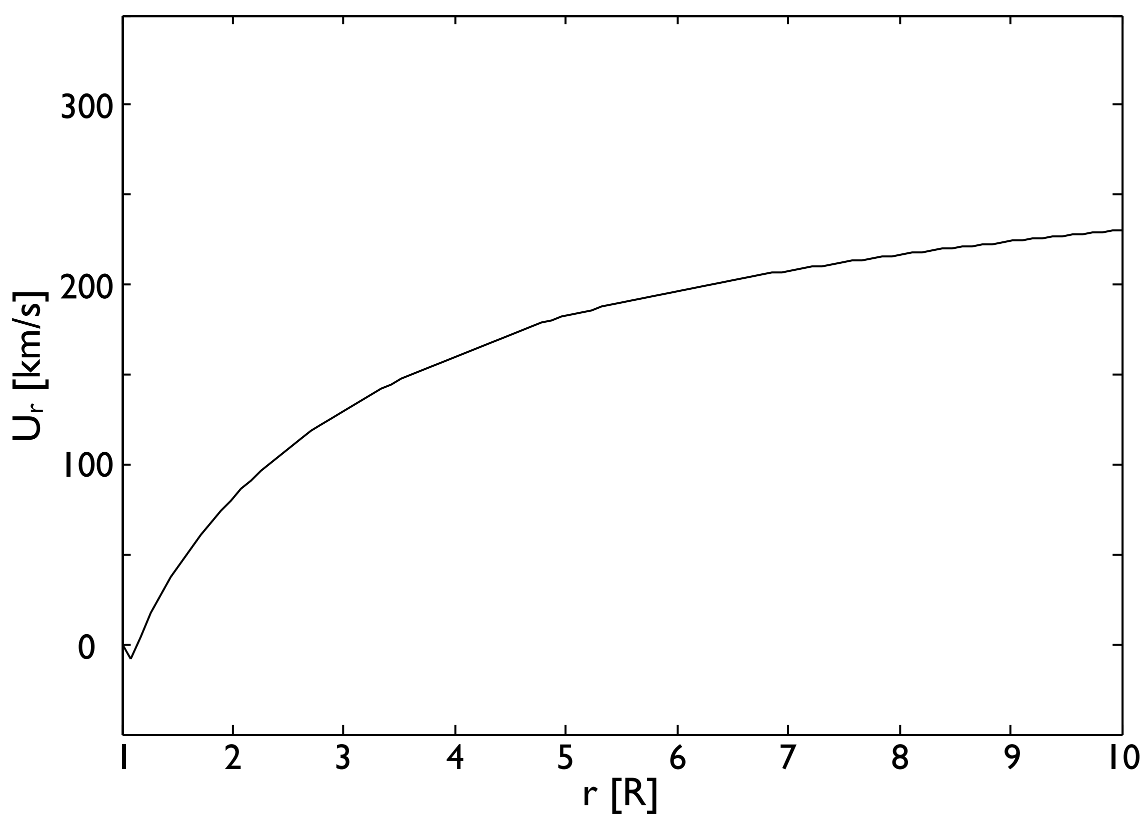

Figure 3.2: A radial velocity steady-state coronal wind solution using $N = 100$ and $Q_0 = 3 \times 10^5\,\mathrm{erg\,cm^{-2}\,s^{-1}}$. This steady-state solution not only provides a slower-than-desired coronal wind, but also generates unwanted accretion near the solar surface. This is an example of the negative effects of using a larger spatial step size Δr.

due to higher N, the method must perform additional source loops as N increases. The number of required source loops initially varies as Δr^2, but approaches a more linear relation for larger N, which is expected from Equation 3.32.

Table 3.1: Comparisons of advective time steps versus source time steps, resulting from source term splitting, with varying spatial steps N.

N	$\Delta t/\Delta t_{\mathrm{src}}$
100	3
200	11
400	42
800	144
1600	408

To avoid an excessive amount of CPU time but obtain our desired steady-state solution a compromise must be made. We can use a more reasonable spatial step size, but then adjust certain source terms to compensate. We have a target outer boundary velocity of 350 km/s.[2] Since our coronal heating term $\mathbf{Q}_{cor}$ is a source that is calibrated to generate our desired wind, we will simply use the correct N and Q_0 combination to allow this outflow velocity. We then choose $N = 1200$, followed by testing various Q_0 values to determine the correct coronal heating constant. This value is found to be $Q_0 = 3 \times 10^5\,\mathrm{erg\,cm^{-2}\,s^{-1}}$.

Using the numerical method described in this chapter, a steady-state solution for the coronal wind, with 1200 spatial steps and $Q_0 = 3 \times 10^5\,\mathrm{erg\,cm^{-2}\,s^{-1}}$, is found and plotted in Figure 3.3. The sonic point is marked at a little under $r = 4\,R_\odot$ (compared to $r = 4.5\,R_\odot$ with an isothermal wind). This location will be important for where we place our mass-loading regions later in this chapter.

3.2.3 Linking the Transonic Coronal Wind and Expanding Cometary Atmospheres

There is a notable link between the transonic coronal wind we just generated and the expanding cometary atmospheres study referenced in the previous chapter. The link is created by the

[2] Based on previous 1D hydrodynamic studies.

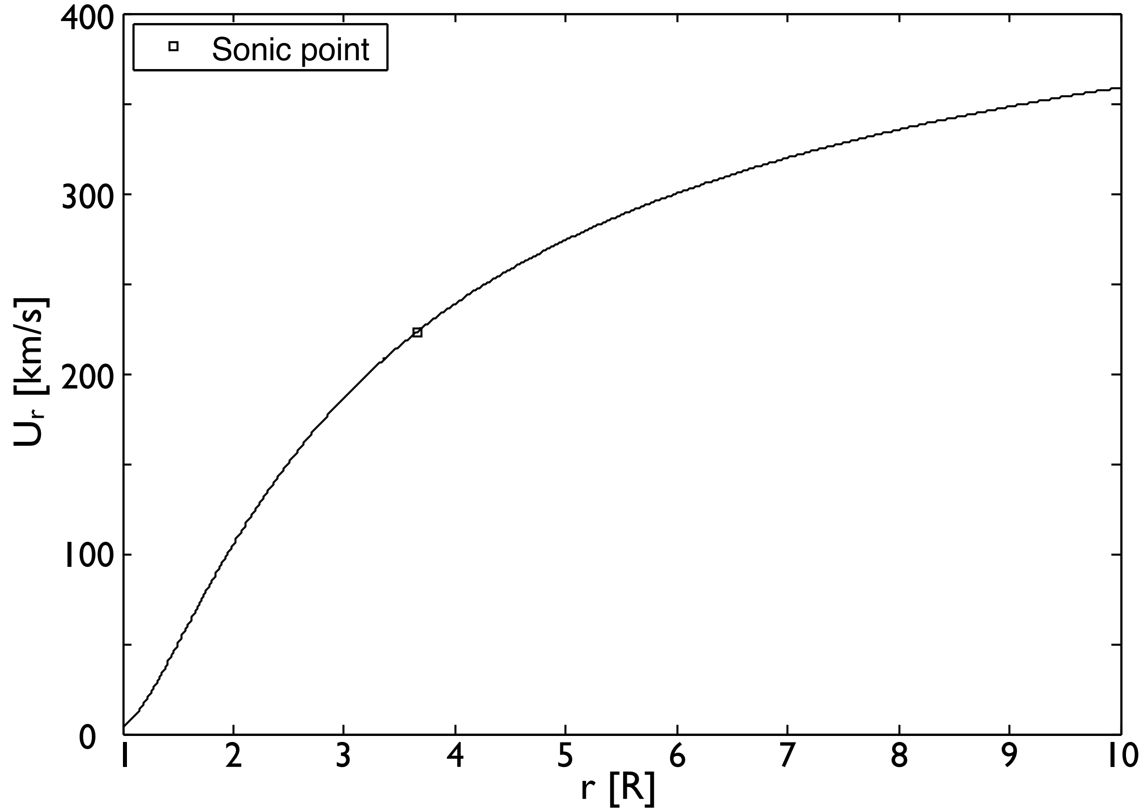

Figure 3.3: The steady-state coronal wind, solved as described using 1200 spatial steps. The marked sonic point corresponds with choke point of the effective area.

effective area and resulting acceleration for each situation. The effective area was calculated (in arbitrary units) for results in Figure 3.3 and plotted in Figure 3.4, along with velocity and effective area plots from Gombosi et al.[11]. For certain parameters in the cometary case, both have very similar acceleration profiles as well as effective area curves that resemble the de Laval nozzle from Figure 2.1.

Each situation, whether an expanding cometary atmosphere or coronal wind acceleration, needs to have both contraction and expansion source terms to generate supersonic flows. In the cometary atmosphere application these two terms come from the momentum loss due to interactions with dust (contraction) and spherical area expansion, respectively. In the coronal wind case, the stronger gravitational pull nearer the Sun replaces the dust interactions, and as it becomes weaker further out the spherical expansion becomes dominant. Similar connections will be drawn as we

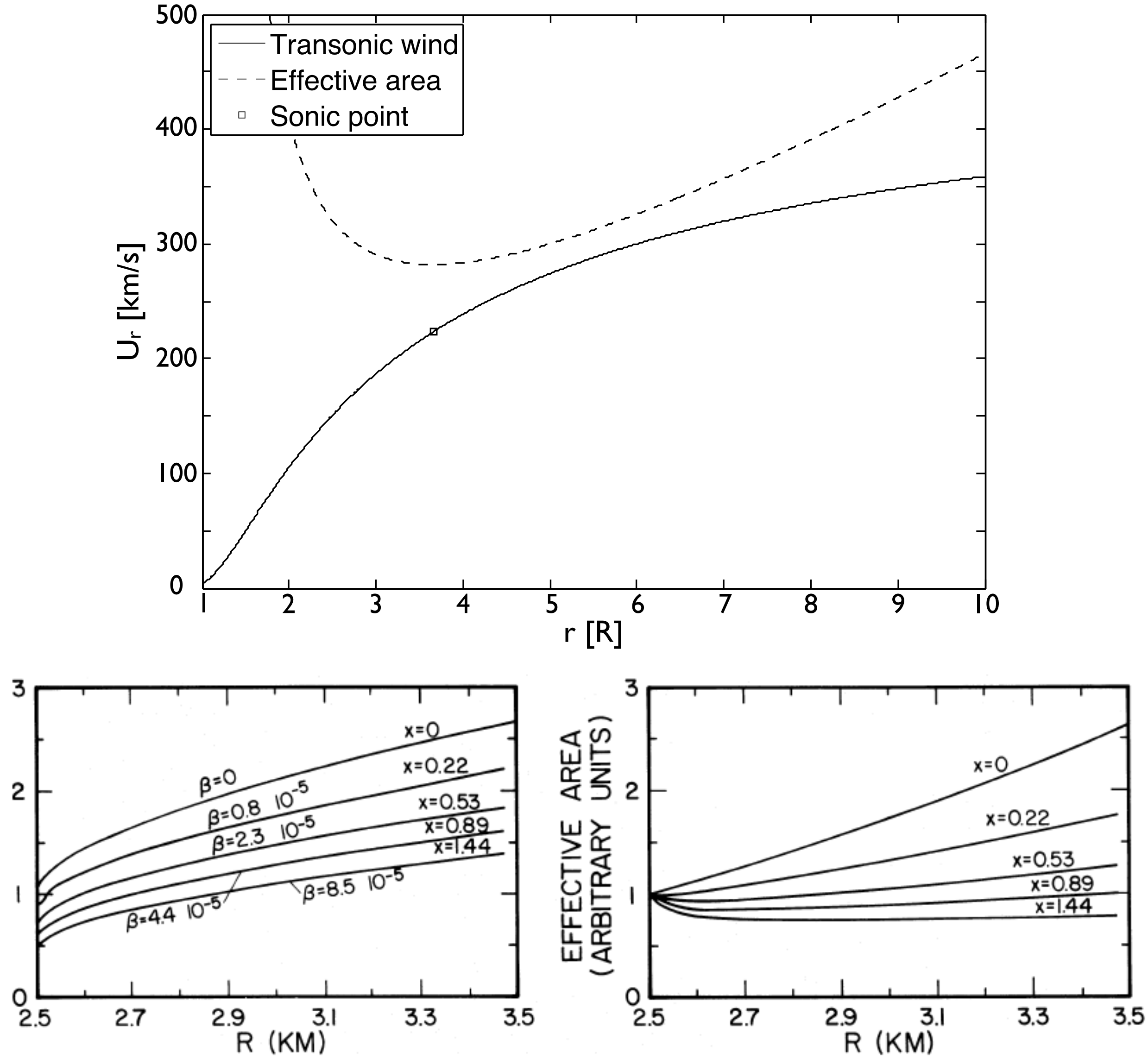

Figure 3.4: Mach number curves (bottom left) and effective area curves (bottom right) produced in Gombosi et al.[11] for expanding cometary atmospheres, compared with the coronal wind velocity and effective area. The various χ values represent dust to gas production rate ratios and β values are friability parameters. The effective area (in arbitrary units) for Figure 3.3 has been calculated and overlaid to show the de Laval nozzle effect taking place in the solar corona. Like the expanding coronal wind, expanding cometary atmospheres behave similar to a fluid passing through a de Laval nozzle, but as a result of different physical processes. Bottom images are reproduced from Gombosi et al.[11].

introduce a mass-loading dust source into the solar corona.

3.3 Mass-Loading Setup

We can now solve Equations 3.10-3.13 with both coronal sources (Equations 3.15-3.18) and mass-loading sources $\mathbf{S}_d$. We will begin as in the previous chapter, by defining mass-loading regions for different intervals, each $1\,R_\odot$ in length. We will also assume again that we have a replenishing dust source.

One significant deviation from our previous mass-loading runs will be the mass-loading factor P_{ml}. From Mann et al.[28], the dust forming the F-corona has a distribution that, in general, increases with decreasing r, before being cut off completely a couple solar radii out. We then define P_{ml} such that it varies by the power law

$$P_{ml} \quad \propto \quad \left(\frac{1}{r}\right)^{1/2}. \tag{3.35}$$

Once again, we are mainly looking for the effects a sudden mass-loading burst will have on the solar wind. P_{ml} is then set somewhat arbitrary such that

$$P_{ml}\,(r = 5\,R_\odot) \quad = \quad 5 \times 10^{-23}\,\mathrm{g\,cm^{-3}\,s^{-1}}. \tag{3.36}$$

This is equivalent to loading the solar wind with $30\,\mathrm{m_p\,cm^{-3}\,s^{-1}}$.

Previous mass-loading results were also limited to an initial solar wind that was purely supersonic. With the coronal wind there are both supersonic and subsonic regions to play around with. We will then also be splitting our mass loading regions into two cases:

- Mass-loading in a subsonic coronal wind
- Mass-loading in a supersonic coronal wind.

We will frame the setup for each case in the following subsection and find new coronal wind steady-states, assuming a constant mass-source with respect to time.

3.3.1 Case 1: Pre-Sonic Point Mass-Loading Regions

Our mass-loading results thus far have relied on an initially supersonic wind. What makes a subsonic wind special is that information can now travel upwind. As a result, we would not expect to get a standing shock, as we did in the previous chapter. The case of placing mass-loading regions before the sonic point (or subsonic case) will allow us to observe a different effect than before. Each mass-loading case will differ only by the mass-loading factor P_{ml}. P_{ml} was described previously to follow the power law $r^{-1/2}$. P_{ml} will now only follow this law within our mass-loading regions and be zero elsewhere,

$$P_{ml} = \begin{cases} 0 & r < r_{\mathrm{L}} \\ P_{ml0}\left(\frac{5R_{\odot}}{r}\right)^{1/2} & r_{\mathrm{L}} \leq r \leq r_{\mathrm{R}} \\ 0 & r > r_{\mathrm{R}} \end{cases} , \tag{3.37}$$

where P_{ml0} is the constant

$$P_{ml0} = 5 \times 10^{-23}\,\mathrm{g\,cm^{-3}\,s^{-1}},$$

described previously.

For the subsonic case, we will solve Equations 2.1-2.4 twice, with a different mass-loading region for each, to test variations within the subsonic case. We will first assign $r_{\mathrm{L}} = 2\,R_{\odot}$ and $r_{\mathrm{R}} = 3\,R_{\odot}$, and then move the mass-loading each out $1\,R_{\odot}$ such that $r_{\mathrm{L}} = 3\,R_{\odot}$ and $r_{\mathrm{R}} = 4\,R_{\odot}$. We then have a mass-loading region entirely within the subsonic region, and one that begins just prior to the sonic point. Also, we will not go closer than $2\,R_{\odot}$, as that would be within the theorized dust-free zone.

3.3.2 Case 2: Post-Sonic Point Mass-Loading Regions

For the supersonic case, we continue with gradually moving the mass-loading region outward to generate two additional sub-cases. We assign $r_{\mathrm{L}} = 4\,R_{\odot}$ and $r_{\mathrm{R}} = 5\,R_{\odot}$ for the first supersonic mass-loading region, which begins right after the sonic point in the undisturbed coronal wind.

Following the established pattern, the other supersonic sub-case has $r_\mathrm{L} = 5\,R_\odot$ and $r_\mathrm{R} = 6\,R_\odot$. All cases are summarized in Table 3.2.

Table 3.2: Mass-loading cases in the 1D coronal wind.

	r_L	r_R
Case 1a	$2\,R_\odot$	$3\,R_\odot$
Case 1b	$3\,R_\odot$	$4\,R_\odot$
Case 2a	$4\,R_\odot$	$5\,R_\odot$
Case 2b	$5\,R_\odot$	$6\,R_\odot$

Due to the nature of the supersonic mass-loading case being located after the sonic point, we do not expect much to change in the way of the post-sonic point wind profile, nor do we expect the location of the first[3] sonic point to change. Not having done a pre-sonic case in the previous chapter, it will be interesting to observe how the sonic point is affected by the mass-loading regions in that case.

3.4 Mass-Loading Results

Using the described amendments to our numerical techniques, we solved Equations 3.10-3.13 for the cases described in the previous section. The undisturbed solar wind and four new mass-loaded steady-states are shown in Figure 3.5, along with corresponding mean molecular weight plots. Prior to the undisturbed sonic point, mass-loading adversely affects the flow upstream, but then accelerates it within the mass-loading region. As expected, if mass-loading takes place after the wind passes through the sonic point, a shock is developed followed by re-acceleration, creating two separate sonic points. This corresponds to how compressible flows behave with area expansions/contractions.

For each steady-state solution in Figure 3.5, we calculated the effective area and plotted them in Figure 3.6 against the velocity and mean mass curves, once again using arbitrary units. Looking back to the previous section, it is again evident a mass addition ($S_2 > 0$) would have an

[3] We may now have solutions with two sonic points, as the mass-loading regions in Case 2 are expected to accelerate the solar wind after a deceleration to subsonic velocities.

area contracting, and thus choking, effect on the flow, forcing the wind to decelerate when it is supersonic but then causing an acceleration of the subsonic wind. The magnitude at which the wind is affected depends on the P_{ml0}, which was set to demonstrate a clearly visible shock past the undisturbed sonic point.

Looking at the downwind effect of mass-loading on the coronal wind, there is a clear trend in how the mass-loading location affects both wind velocity and composition, the latter being represented by mean molecular mass. In general, mass-loading will generate a slower and more massive wind downstream, but the locations of mass-loading will vary the effects. Even though the mass-loading rate is greater near the Sun in our simulations, mass-loading further out will have a more significant effect on both aforementioned aspects of the solar wind. With increasing heliocentric distance the mass-loading rate is not dropping as fast as the solar wind density, causing a larger ratio of P_{ml} to ρ further out. We should note that this effect can vary with mass-loading rate models different from Equation 3.35. These results are presented in Rasca and Horányi[38].

3.5 Need for an Advanced Solar Wind Model

This is a fairly simplified model of the coronal wind. While the actual solar wind does behave much like a fluid, it is also made up of charged particles mutually interacting with solar-originating magnetic fields. The lack of magnetic fields $\mathbf{B}$ in a purely hydrodynamic model is reflected by the lack of a magnetic pressure component. The total pressure should be the sum of the gas pressure and magnetic pressure,

$$p = p_{\text{gas}} + p_{\text{mag}}, \tag{3.38}$$

but the hydrodynamic model only includes the gas pressure $p = p_{\text{gas}}$. Additionally, this model is restricted to 1D, even though it captures the generally spherical geometry of the flow. Hence, we cannot see how the magnetic field environment is changing in a 3D space due to the mass-loaded solar wind. For these reasons we will apply the same mass-loading model to a 3D MHD code.

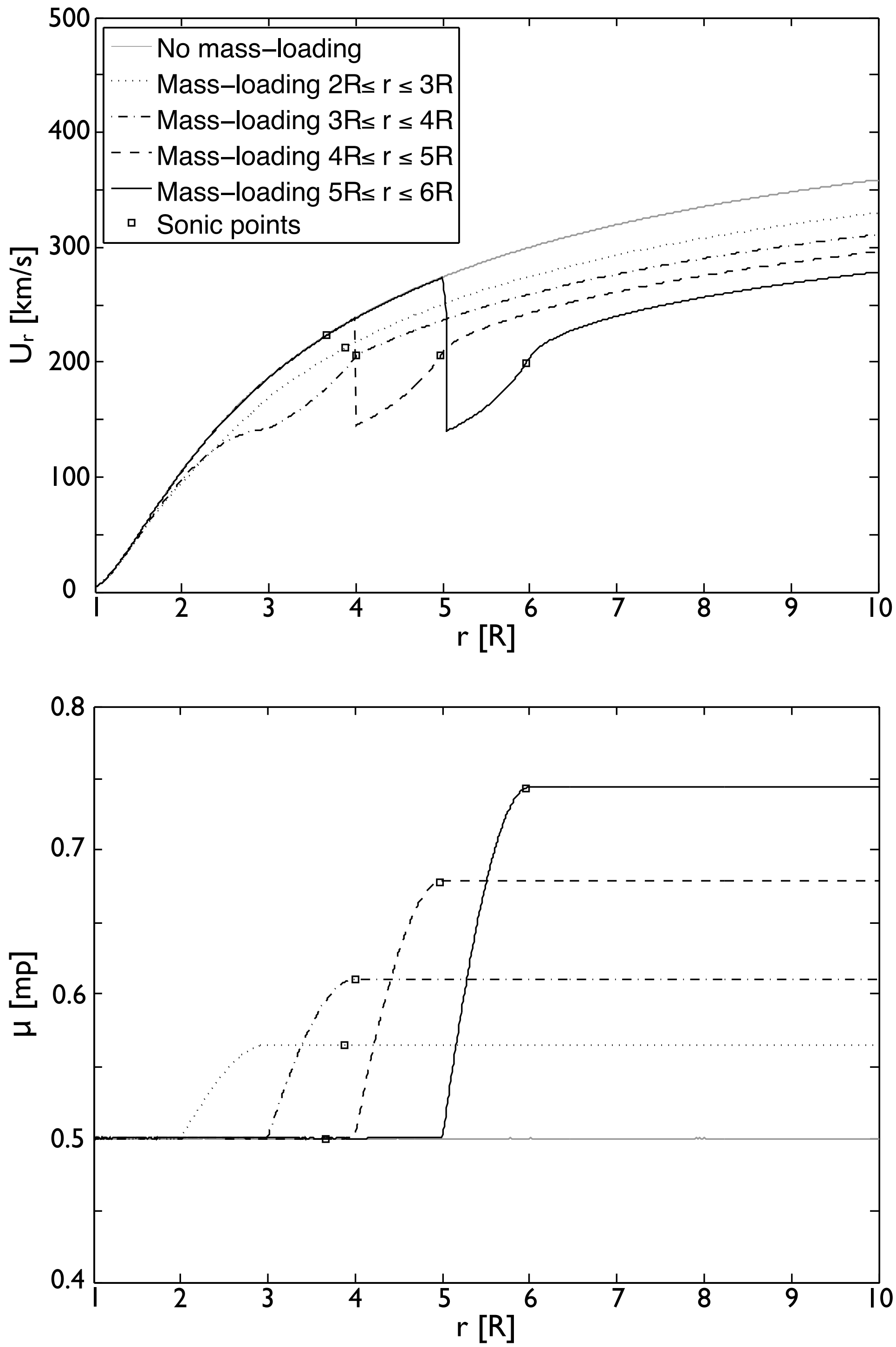

Figure 3.5: Steady-state solutions for radial velocity and mean molecular weight (assuming micron-sized dust particles) with mass-loading occurring in four different spatial intervals away from the Sun. Sonic points are marked for both the undisturbed coronal wind and the new steady-states. Note the difference in deceleration/acceleration between cases when mass-loading starts before the undisturbed sonic point and when it begins after the sonic point.

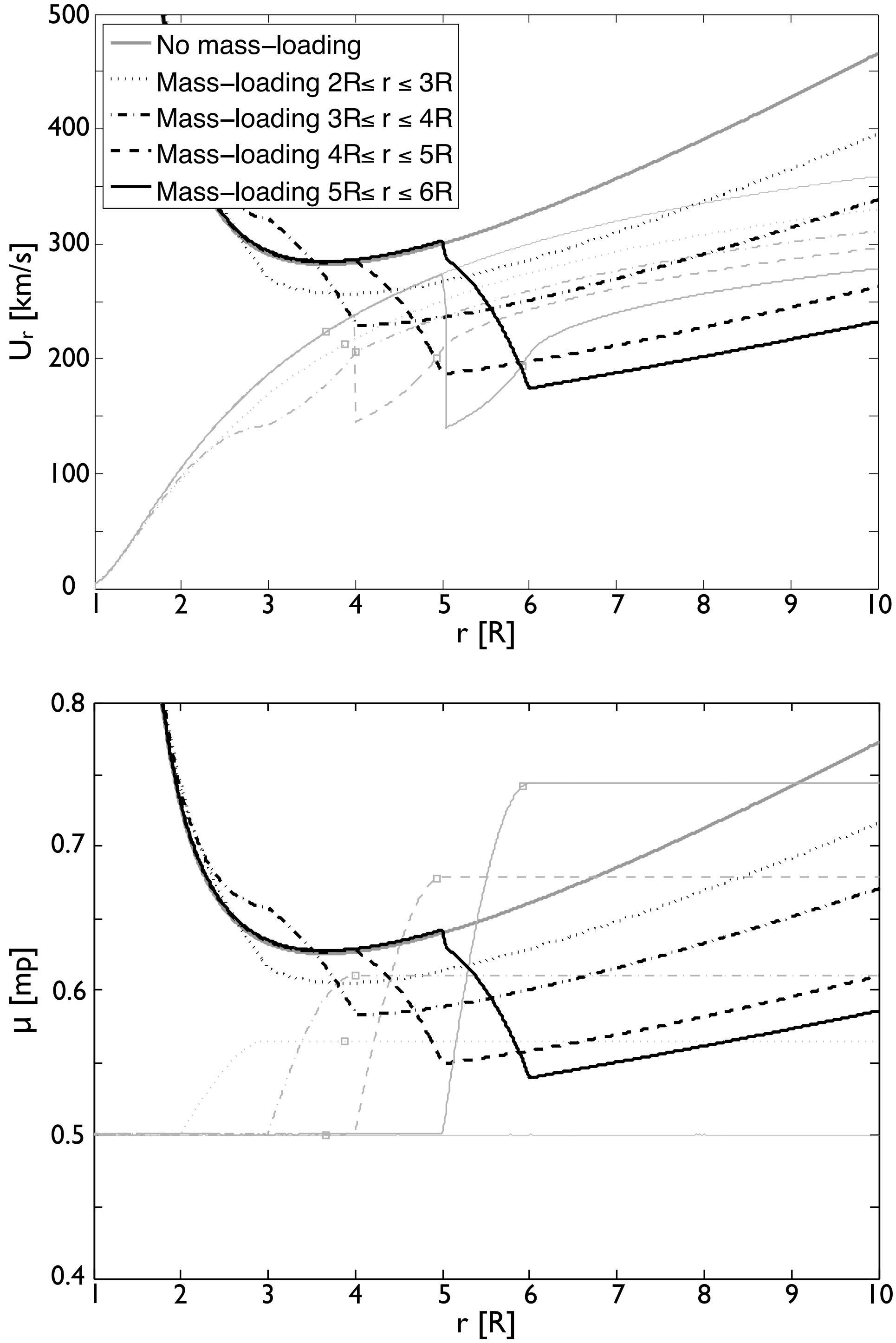

Figure 3.6: The effective area profiles (in bold) for all four mass-loaded steady-states and the initial condition plotted against the velocity and mean molecular weight profiles from Figure 3.5. The effective area uses arbitrary units and has been scaled to fit within the plot ranges. In agreement with area expansion/contraction effects for compressible flows, sharp changes between expanding A_{eff} and contracting A_{eff} in the last two curves correspond with both the shocks and second sonic points in the appropriate velocity profiles. For the first two mass-loaded curves we only get one change in A'_{eff}, corresponding with the single sonic point.

Chapter 4

3D MHD Modeling

We now venture away from the safety of 1D hydrodynamic modeling and move to using a full 3D MHD model. MHD modeling has numerous applications, not only for the solar wind, but for the solar interior as well as both solar and planetary magnetospheres. There are multiple groups worldwide developing such codes for heliospheric problems, many of which are utilized by the Community Coordinated Modeling Center (CCMC) for space weather modeling. One prominent model is called the Space Weather Modeling Framework (SWMF), developed at the University of Michigan's Center for Space Environment Modeling (CSEM). Due to its reputation, easy accessibility, and adaptability to additional heliophysics problems, the SWMF is the code we will be working with for our MHD simulations.

In this chapter we will describe the SWMF used for several heliophysics-related problems, with detailed information on a Solar Corona (SC) component used by SWMF for coronal wind modeling. We will describe our modifications to the selected SC component in order to model mass-loading in the solar wind. Last, we will set up and run the modified SC component code for mass-loading cases similar to those in the previous chapter. These new results will allow a comparison between the hydrodynamic and MHD models.

4.1 SWMF and BATS-R-US Description

The SWMF provides space weather scientists an excellent way to model phenomenon taking place anywhere in the solar system due to its interwoven modular physical component structure.

For example, the SWMF can have one of its physical components model a solar storm originating from the corona and have a different component modeling its impact on planetary magnetospheres. We provide a brief overview in this section of both the SWMF and an MHD code it relies heavily on called the Block-Adaptive-Tree-Solarwind-Roe-Upwind-Scheme (BATS-R-US), as it pertains to our particular problem. The SWMF and BATS-R-US are described in much more detail in Powell et al.[36], Tóth et al.[47], and references therein.

4.1.1 Model Components

The SWMF is a collection of components that can be all coupled together. Each component covers a different physical domain. The list of domains are:

- Solar Corona (SC)
- Eruptive Event Generator (EE)
- Inner Heliosphere (IH)
- Solar Energetic Particles (SP)
- Global Magnetosphere (GM)
- Inner Magnetosphere (IM)
- Radiation Belt (RB)
- Ionosphere Electrodynamics (IE)
- Upper Atmosphere (UA).

Many of these components are not relevant to our particular work, but are important to other areas of space weather modeling. We are mainly concerned with the SC component, and to some extent the IH component, as it is an extension of the solar corona domain. These, along with other components such as the EE and GM, rely on the BATS-R-US MHD modeling code.

BATS-R-US, originally described in Powell et al.[36], is a 3D MHD model based, similarly to our 1D hydrodynamic code, on finite-volume upwind schemes and approximate Riemann solvers. However, their set of MHD equations extends from Euler's fluid equations to account for Maxwell's equations of electrodynamics. The basic set of 3D MHD equations (excluding external sources such as gravity) are

$$\begin{aligned}
\frac{\partial \rho}{\partial t} + \nabla \cdot (\rho \mathbf{u}) &= 0 && (4.1)\\
\frac{\partial \rho \mathbf{u}}{\partial t} + \nabla \cdot \left[\rho \mathbf{u}\mathbf{u} + \left(p + \frac{B^2}{2\mu_0}\right) I - \frac{\mathbf{B}\mathbf{B}}{\mu_0}\right] &= 0 && (4.2)\\
\frac{\partial \mathbf{B}}{\partial t} + \nabla \cdot (\mathbf{u}\mathbf{B} - \mathbf{B}\mathbf{u}) &= 0 && (4.3)\\
\frac{\partial E}{\partial t} + \nabla \cdot \left[\mathbf{u}\left(E + p + \frac{B^2}{2\mu_0}\right) - \frac{(\mathbf{u}\cdot\mathbf{B})\,\mathbf{B}}{\mu_0}\right] &= 0, && (4.4)
\end{aligned}$$

where we now introduce the 3D velocity vector

$$\mathbf{u} = (u_x,\, u_y,\, u_z)^\top, \tag{4.5}$$

the magnetic field vector

$$\mathbf{B} = (B_x,\, B_y,\, B_z)^\top, \tag{4.6}$$

the magnetic field strength

$$B = |\mathbf{B}|, \tag{4.7}$$

the permeability of free space μ_0, and an updated energy definition,

$$E = \frac{1}{2}\rho \mathbf{u}\cdot\mathbf{u} + \frac{p}{\gamma - 1} + \frac{B^2}{2\mu_0}. \tag{4.8}$$

Instead of three equations, we now have a system of eight coupled equations.

Equations 4.1-4.4 form the backbone of SWMF components SC, EE, IH, and GM, and can be tailored to suit a specific need. And unlike our 1D hydrodynamic model, BATS-R-US is a massively parallel code and includes adaptive mesh refinement (AMR) for resolving regions of high gradients, both of which take advantage of the grid block structure.

4.1.2 Block Structure

BATS-R-US is run on a grid using a block tree structure. The grid is first divided into a user-selected number of blocks, each one containing the same number of cells. A typical block structure used with BATS-R-US is a 3D 4x4x4 structure, meaning the grid is initially split into 64 blocks, with four to a side. The user can then define the cell structure for all blocks. Again, say the blocks all have a 4x4x4 cell structure. The grid is then composed of 64 blocks, each containing 64 cells, for an overall 4,096-cell grid. This is not limited to a Cartesian grid, though we did use Cartesian subscripts for the $\mathbf{u}$ and $\mathbf{B}$ components in Equations 4.5 and 4.6, and can be applied to non-Cartesian grid such as a spherical one.

If a grid needs to be refined, blocks are divided into eight self-similar blocks (four blocks for 2D), each retaining the same cell structure. Figure 4.1 (bottom) shows an example of a 2D grid with a 2x2 block structure and 4x4 cell structure being refined three levels. It also shows a 3D grid with a 1x1x2 block structure and 8x8x8 cell structure being partially refined (top), with the inclusion of ghost cells. Regions of refinement can be user-selected or automatic by specific criteria. For the SC component, refinement is initially performed in the current sheet and near the solar surface, where large gradients exist.

4.1.3 Performance

BATS-R-US was created with high-performance, parallel computing in mind. The block tree structure just described plays a very significant part in boosting the performance of BATS-R-US when running in parallel. This is done by dividing the grid between processors according to blocks, which all have the same cell structure. This reduces the amount of time needed for processors to communicate with each other, freeing up computing power for solving on the individual blocks first.

Figure 4.2 shows how BATS-R-US performs on various supercomputers when the number of processors is increased. Optimally, we would want performance to increase linearly with processors, but code will always underperform as a result of more processors requiring more communication

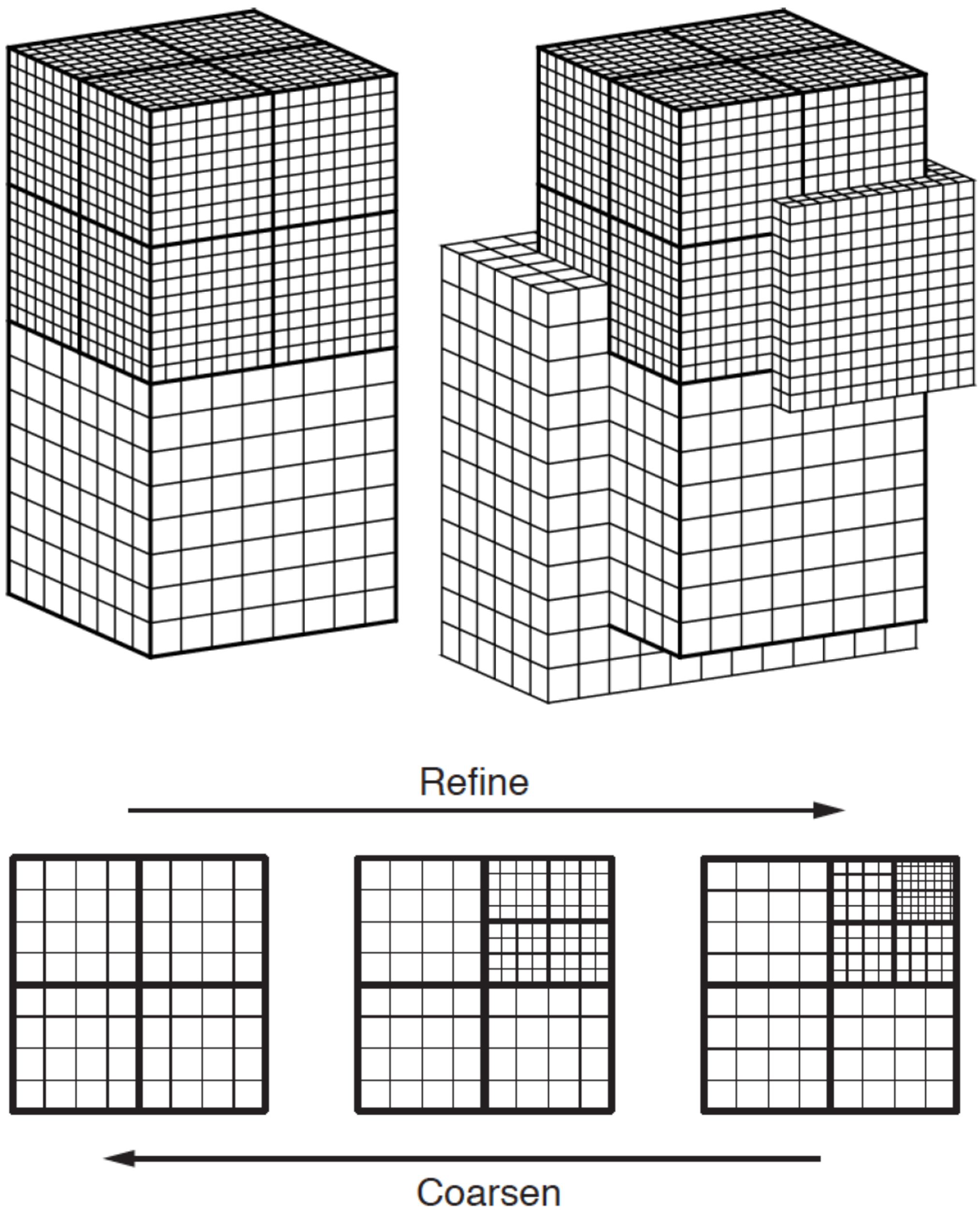

Figure 4.1: Two examples of refined BATS-R-US grids: (top) a 3D grid with a 1x1x2 block structure and 8x8x8 cell structure, and (bottom) a 2D grid with a 2x2 block structure and 4x4 cell structure, both being partially refined. Images are reproduced from Hansen et al.[14].

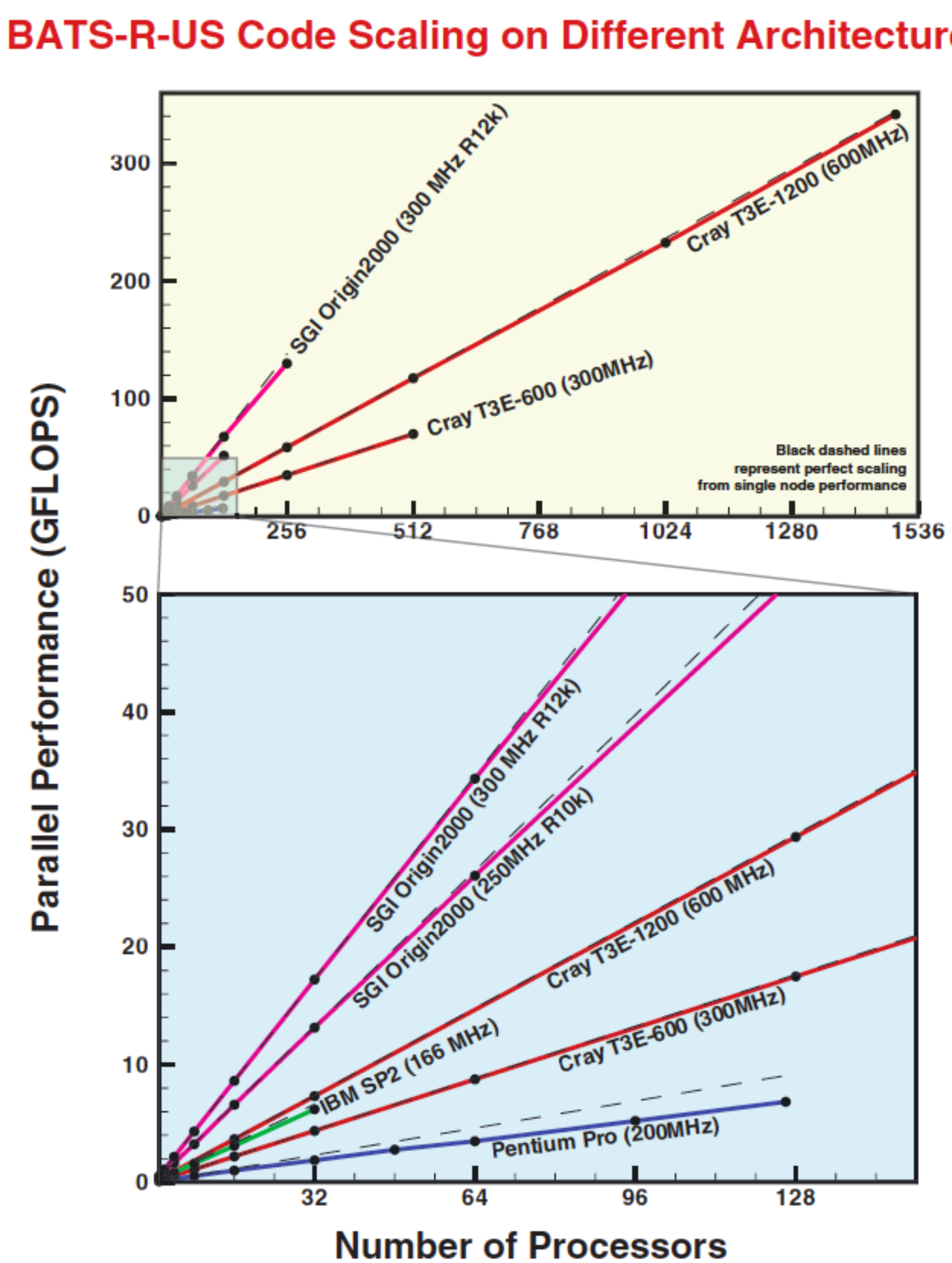

Figure 4.2: Performance of BATS-R-US as a function of processors used when run on various supercomputers. Image is reproduced from BATS-R-US and CRASH User Manual[5].

between them. For BATS-R-US, the curves are very near linear as a result of processor communication relying on the number of blocks instead of the number of cells.

4.2 A Solar Corona Component of SWMF

In this study, we build on the coronal model of van der Holst et al.[49] for the SC component. This model solves the coupled system of the MHD equations and a WKB equation for low frequency Alfvén waves. The waves serve to accelerate and heat the plasma in open magnetic field lines (Hollweg[16]). Although this model is capable of describing a two temperature (electrons+protons) plasma, in this work we consider a single temperature plasma, since we wish to focus on the plasma-dust interactions. For this purpose, we modify the model by van der Holst et al.[49] to account for dust-wind interactions through mass-loading by extending it to a multi-species description. The multi-species capabilities of BAT-S-RUS are described in Tóth et al.[48]. The multi-species aspect generates an additional mass conservation equation as a result of splitting the mass density into hydrogen density ρ_{H} (both protons and electrons) and ionized dust density ρ_{d_i} such that

$$\rho = \rho_{\mathrm{H}} + \rho_{d_i}. \tag{4.9}$$

We also have gas pressure p and energy E as the sum of hydrogen and dust contributions, but would only be separated as in Equation 4.9 for a multi-fluid model.

4.2.1 SC Component Equations

The updated set of MHD equations, taken from van der Holst et al.[49] and modified for multi-species use with dust particles, are

$$\begin{aligned}
\frac{\partial \rho_{\mathrm{H}}}{\partial t} + \nabla \cdot (\rho_{\mathrm{H}} \mathbf{u}) &= 0 && (4.10)\\
\frac{\partial \rho_{d_i}}{\partial t} + \nabla \cdot (\rho_{d_i} \mathbf{u}) &= S_{\rho_{d_i}} && (4.11)\\
\frac{\partial (\rho \mathbf{u})}{\partial t} + \nabla \cdot \left[\rho \mathbf{u}\mathbf{u} + \left(p + p_{\mathrm{W}} + \frac{B^2}{2\mu_0}\right) I - \frac{\mathbf{B}\mathbf{B}}{\mu_0}\right] &= \mathbf{S}_{\rho \mathbf{u}} && (4.12)\\
\frac{\partial \mathbf{B}}{\partial t} + \nabla \cdot (\mathbf{u}\mathbf{B} - \mathbf{B}\mathbf{u}) &= 0 && (4.13)
\end{aligned}$$

$$\frac{\partial E}{\partial t} + \nabla \cdot \left[\mathbf{u} \left(E + p + p_{\mathrm{W}} + \frac{B^2}{2\mu_0} \right) - \frac{(\mathbf{u} \cdot \mathbf{B}) \mathbf{B}}{\mu_0} + \left(E_{\mathrm{W}}^{+} - E_{\mathrm{W}}^{-} \right) \mathbf{u}_{\mathrm{A}} \right] = S_E, \tag{4.14}$$

where $\mathbf{u}_{\mathrm{A}}$ is the Alfvén speed and $S_{\rho_{d_i}}$, $\mathbf{S}_{\rho\mathbf{u}}$, and S_E are the dust density, momentum, and energy sources, respectively. The presence of Equation 4.11 replaces the need for a number density conservation equation, since we can determine n from ρ_{H} and ρ_{d_i}.

The wave energy densities of the Alfvén waves propagating parallel and anti-parallel to $\mathbf{B}$ are denoted by E_{W}^{+} and E_{W}^{-}, respectively, and the Alfvén wave energy density and pressure are defined as

$$E_{\mathrm{W}} = E_{\mathrm{W}}^{+} + E_{\mathrm{W}}^{-} \tag{4.15}$$

and

$$p_{\mathrm{W}} = E_{\mathrm{W}}/2. \tag{4.16}$$

The energy definition gets a second modification, extending from the basic MHD definition to

$$E = \frac{1}{2}\rho \mathbf{u} \cdot \mathbf{u} + \frac{p}{\gamma - 1} + \frac{B^2}{2\mu_0} + E_{\mathrm{W}}, \tag{4.17}$$

with the Alfvén wave energy given by the time-dependent solution of

$$\frac{\partial E_{\mathrm{W}}^{\pm}}{\partial t} + \nabla \cdot \left[E_{\mathrm{W}}^{\pm} \left(\mathbf{u} \pm \mathbf{u}_{\mathrm{A}} \right) \right] = -p_{\mathrm{W}}^{\pm} \nabla \cdot \mathbf{u} - Q^{\pm}, \tag{4.18}$$

where the $\pm$ sign stems from two Alfvén wave solutions. $Q^{\pm}$ is the wave dissipation defined as

$$Q^{\pm} = \frac{\left(E_{\mathrm{W}}^{\pm} \right)^{3/2}}{L\sqrt{\rho}}, \tag{4.19}$$

where L is the perpendicular correlation length of the Alfvén waves. The non-zero source terms for mass, momentum, and energy take into account mass-loading, gravity, thermal heat flux, and angular motion of the Sun,

$$\begin{aligned} S_{\rho_d} &= S_{d2} && (4.20) \\ \mathbf{S}_{\rho\mathbf{u}} &= \mathbf{S}_{d3} - \rho \left[\frac{GM}{r^3}\mathbf{r} + \mathbf{\Omega} \times (\mathbf{\Omega} \times \mathbf{r}) + 2\mathbf{\Omega} \times \mathbf{u} \right] && (4.21) \\ S_E &= S_{d4} - \nabla \cdot \mathbf{Q}_{cond} + \rho \mathbf{u} \cdot \left[\frac{GM_{\odot}}{r^3}\mathbf{r} + \mathbf{\Omega} \times (\mathbf{\Omega} \times \mathbf{r}) \right]. && (4.22) \end{aligned}$$

$\mathbf{Q}_{cond}$ is the Spitzer thermal heat flux vector applied only within 10 $R_{\odot}$ and $\mathbf{\Omega}$ is the angular velocity of the Sun.

4.2.2 Computational Grid and Boundary Conditions

This model for the SC component is not only capable of utilizing a Cartesian grid, but a spherical grid as well. This is a much better grid for 3D work, considering the spherical nature of the corona and inner heliosphere. The spherical grid we will employ extends from the inner boundary defined at the coronal base to the outer boundary defined at $r = 24\,R_{\odot}$.

The inner boundary for the magnetic field uses the solar dipole field at $1\,R_{\odot}$ with field strength $1.4\,G$ at the poles, while the remaining inner boundary values are determined using the Wang-Sheely-Arge (WSA) model Arge and Pizzo[2], with the temperature and number density normalized to 1.5×10^6 K and $10^8\,\mathrm{cm}^{-3}$ at the inner boundary. The radial distance for the outer boundary can be arbitrarily chosen, provided the wind speed at that boundary exceeds the magnetosonic speed (the sonic speed equivalent for a magnetized plasma) for outflow boundary conditions, which is satisfied well within $r = 24\,R_{\odot}$. The grid uses a 6x4x4 block tree structure, meaning the entire grid is a collection of blocks with dimensions 6 by 4 by 4 cells in the radial, polar, azimuthal directions, respectively.

Initially, the grid will be refined near the solar surface and in the current sheet, located in the Sun's equatorial plane. In these locations there exist large gradients in velocity, hence the reason for refinement. Figure 4.3 shows our initial grid in the xz-plane. The the location and size of the Sun is evident by the inner boundary of the grid surrounding $(x,\, z) = (0,\, 0)$.

4.2.3 A Steady-State Coronal Wind

The general structure of the solar wind, without the inclusion of mass loading source terms is illustrated in Figure 4.4, where we show results from a steady-state (in the co-rotating frame) simulation run on the Janus supercomputer, operated by the University of Colorado at Boulder. Color contours show the radial speed in the entire domain. Unlike our 1D model, the 3D solar wind has a latitude-dependent structure. A fast wind blows above the poles, while a slow wind occupies the equatorial regions. The 1D wind model is based on slow wind parameters, which is evident

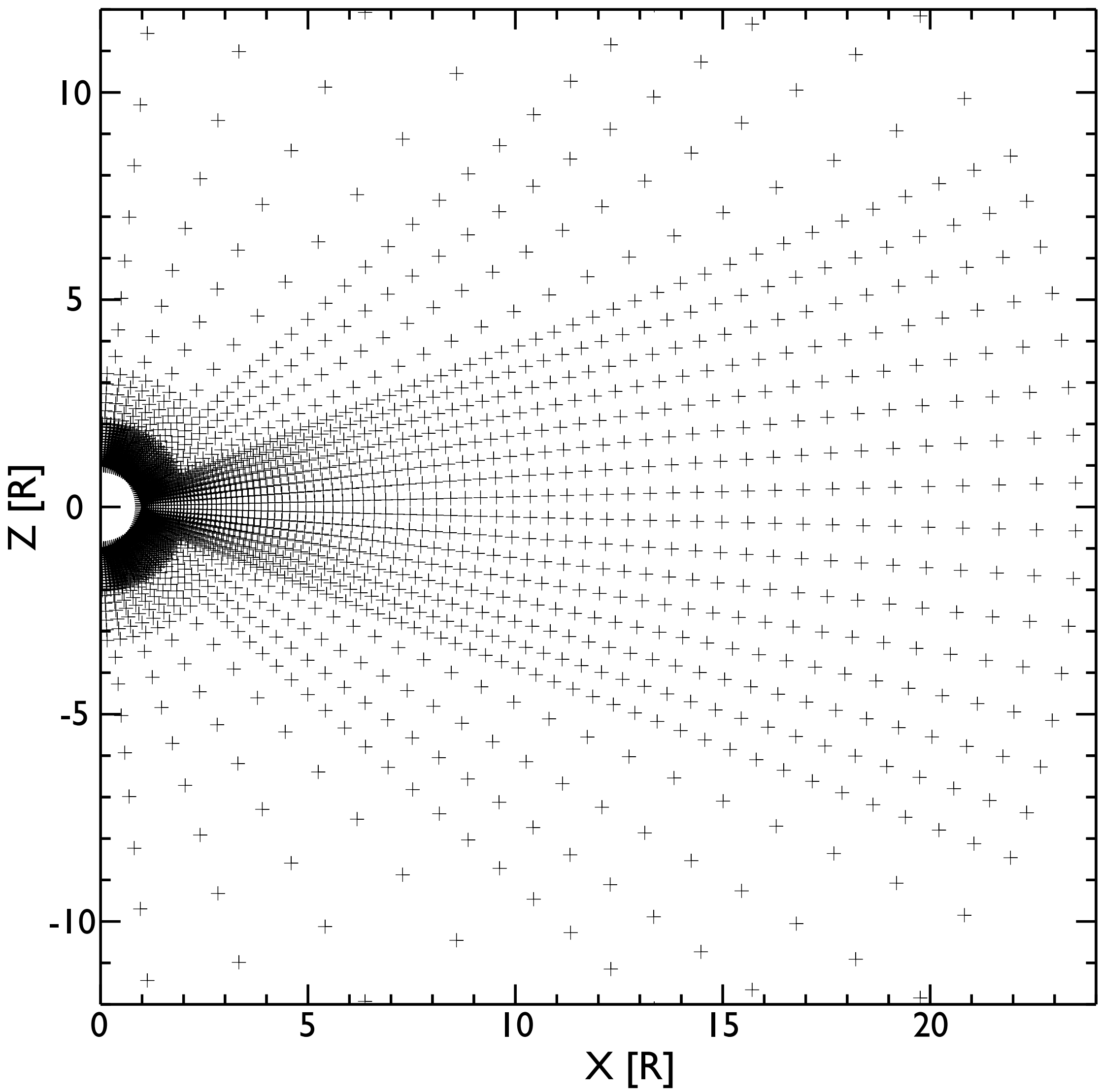

Figure 4.3: A starting computational grid shown in the xz-plane for determining an initial steady-state coronal wind. The initial AMR regions are located near the solar surface and encompass the current sheet.

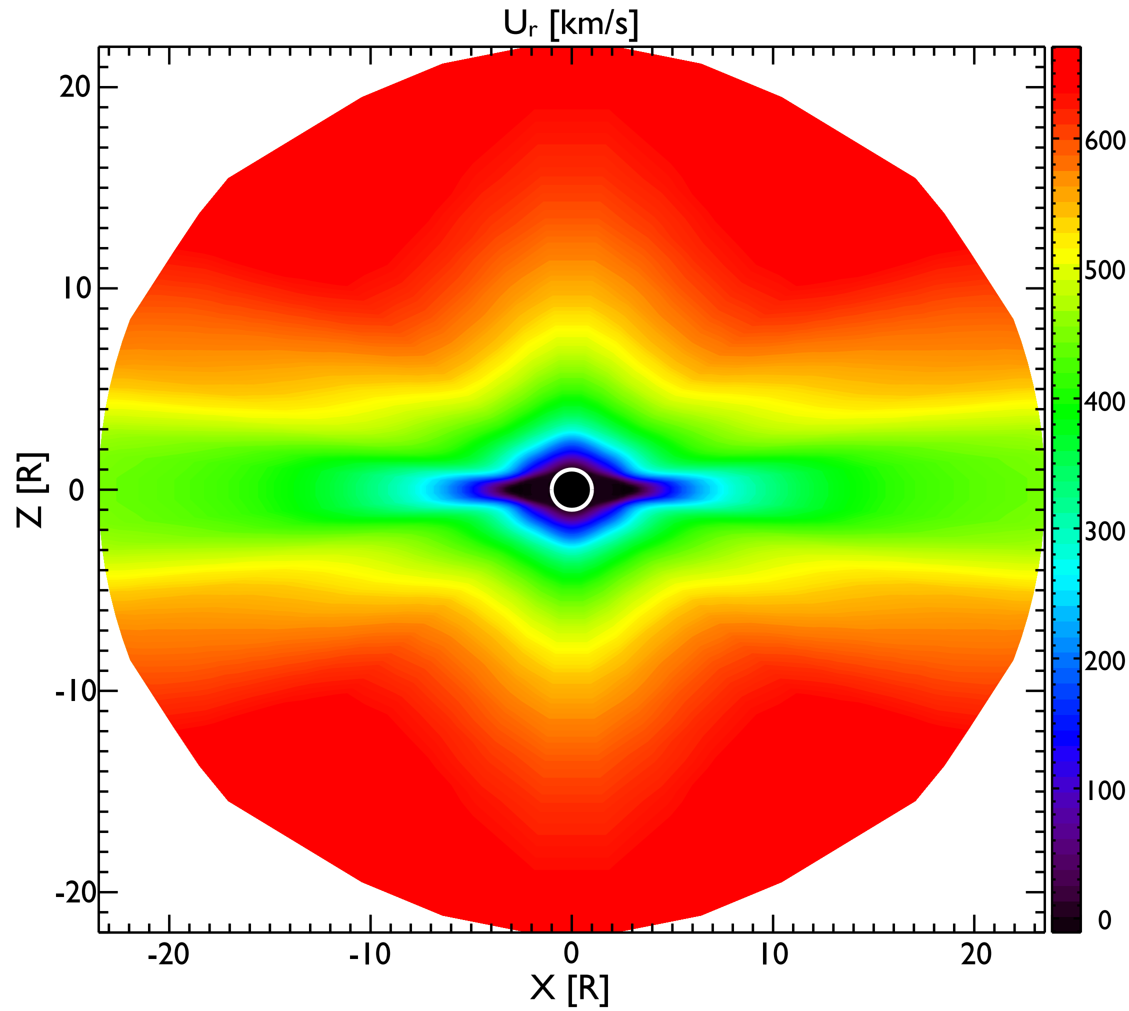

Figure 4.4: The radial velocity steady-state in the xz-plane from solving the SC component (Equations 4.10-4.14) using the computational grid shown in Figure 4.3. The Sun's outline is drawn in the center.

when observing the radial velocities from Figure 4.4 along the $+x$-axis (Figure 4.5).

Another significant addition with the MHD model is the presence of magnetic fields. Figure 4.6 shows the magnetic field structure from the steady-state solution in Figure 4.4, both in the xy-(top) and xz-planes (bottom). In the xy-plane, we see the initial formation of Parker spirals, an important result of the solar rotation terms in Equations 4.20-4.22. These cause objects further out from the Sun to not see the solar magnetic field as straight radial lines, due to continued bending, forming a spiral magnetic structure. In the xz-plane, the field lines do appear radial[1] and switch directions between the north and south hemispheres. Magnetic field lines in Figure 4.6 and later in this chapter appear to cross at $z = 0$, forming v-shaped curves. Though there are closed magnetic loops near the Sun's surface, such connections further out are a result of numerical diffusion causing magnetic reconnections between outgoing and ingoing field lines near $z = 0$. The drop in magnetic

[1] The magnetic field lines still bend in the azimuthal direction.

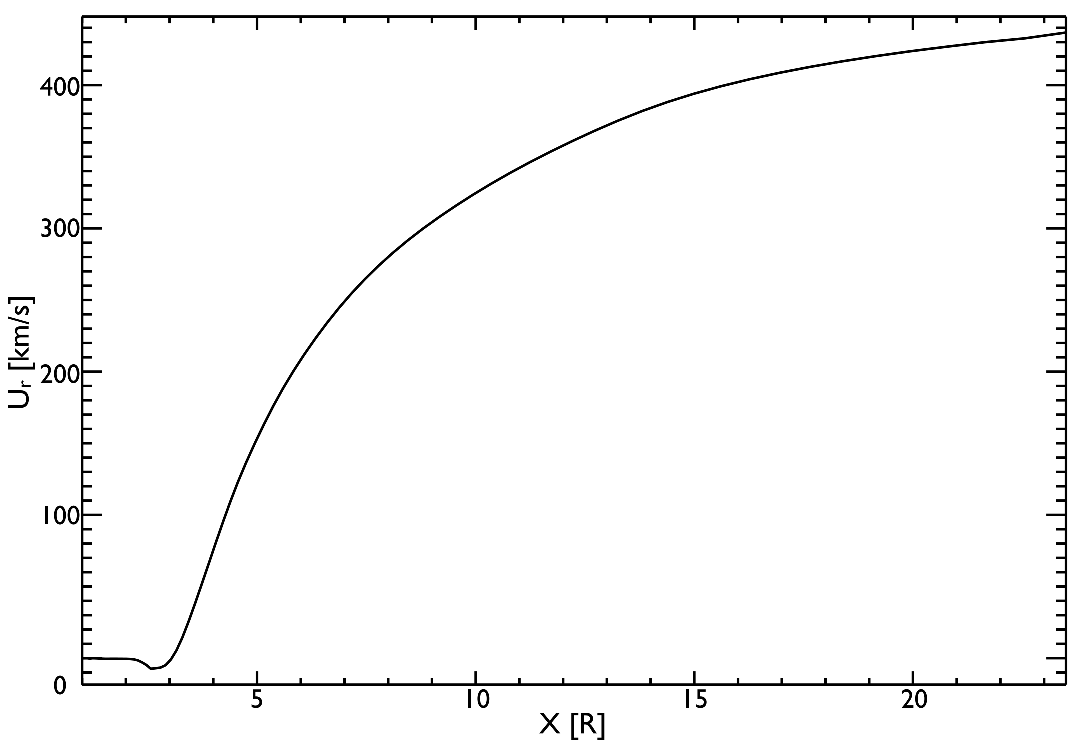

Figure 4.5: The radial velocity steady-state from Figure 4.4 depicted along the $+x$-axis. Due to symmetry from our boundary conditions, the radial velocity profiles should be equal for any radial direction in the xy-plane.

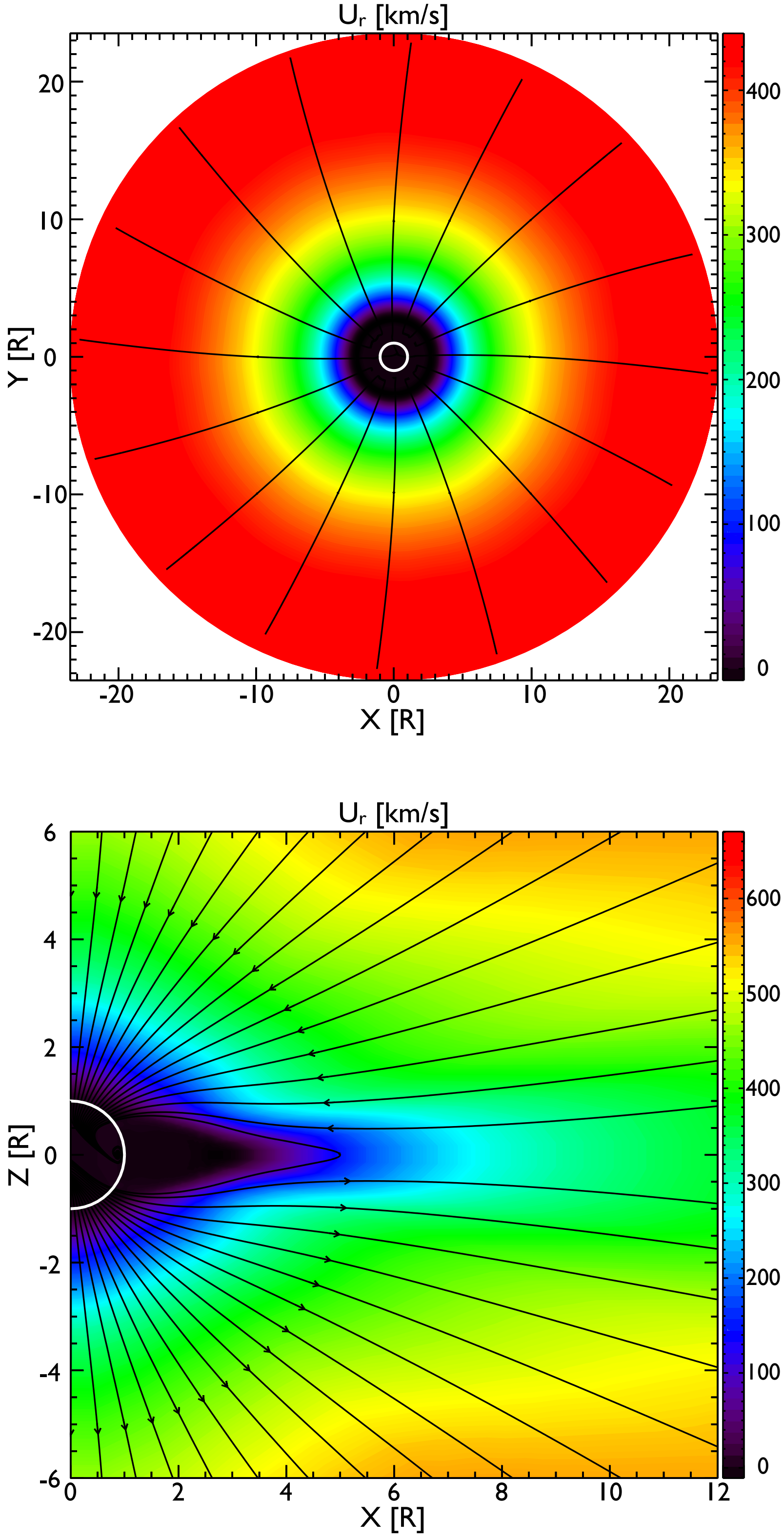

Figure 4.6: Magnetic field lines plotted over the radial velocity steady-state from Figure 4.4. The top panel shows magnetic field lines in the xy-plane, forming a spiral structure resulting from solar rotation. The bottom panel shows the radial line structure in the xz-plane.

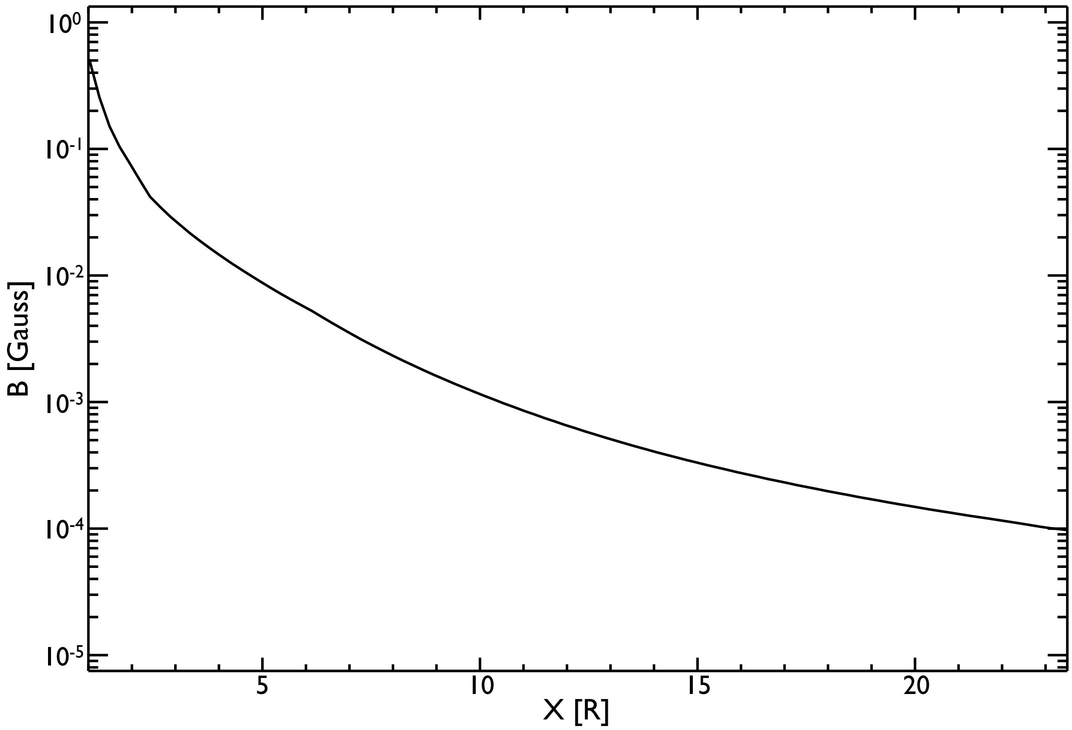

Figure 4.7: The magnetic field strength B from the Figure 4.6 depicted in the slow solar wind along the x-axis.

field strength B in the slow solar wind, along the x-axis is shown in Figure 4.7.

4.3 Comparing 1D Hydrodynamic Results with MHD Simulations

With a reasonable steady-state MHD coronal wind established, we can generate a mass-loading coronal wind without the limitations of a simple 1D hydrodynamic model. In this section we will set up mass-loading regions similar to those created in the previous chapter, but using the modified SC component described above. Included will be several adjustments to the mass-loading cases, due to differences in transitioning from a hydrodynamic to an MHD model. We will then compare the 1D hydrodynamic and 3D MHD results obtained thus far.

4.3.1 Differences Between 1D Hydrodynamic and 3D MHD Steady-State Winds

The purpose of the 1D hydrodynamic results discussed in previous chapters were to illustrate the outcome of a mass-loaded solar wind in the corona. The 1D aspect allows for a simple and convenient model to work with, but a full 3D MHD solar wind gives a better picture of the environment being mass-loaded. Two major differences between the slow wind velocity profile depicted in Figure 4.5 and the undisturbed wind velocity in Figure 3.3, while similar in shape and velocity, are the outward shift of initial acceleration from a near-zero wind and the sonic point, located $1\,R_{\odot}$ further out, at around $r = 5\,R_{\odot}$ in the MHD velocity profile. These differences generate a few changes in setting up similar mass-loading cases to those in Chapter 3, but now using the modified SC component described in the previous section.

To compare mass-loading results between using 1D hydrodynamic and 3D MHD models, we need to change the locations of our mass-loading regions. The shock-generating mass-loading regions used for results in Figure 3.5 are placed just downstream of the sonic point. Seeing that the sonic point is now over $1\,R_{\odot}$ further out with the MHD model, it is reasonable to place our new mass-loading region further out as well. However, with changes in location (and model) also come changes in wind density. Both factors cause the local solar wind density to decrease. For example, $\rho\,(5\,R_{\odot})$ in the MHD model is nearly an order of magnitude less than $\rho\,(4\,R_{\odot})$ in the hydrodynamic model. It is no longer reasonable to use the same mass-loading rate P_{ml} value as with the hydrodynamic model. We will instead select P_{ml} such that the ratio of the mass per volume being added to the solar wind over a fixed time and the initial local solar wind wind density remains about the same.

Additionally, the spatial bounds on the mass-loading region will also need to be adjusted. As evidenced in Figure 4.4, wind velocities in the MHD model are dependent on the polar angle. We are only concerned with comparing the hydrodynamic results with results originating from similar initial velocity profiles, so we will also restrict our mass-loading region to the slow wind near the current sheet by placing bounds on the z coordinates. This results in a ring-shaped mass-loading region. Since we expect a shock to form in results involving post-sonic mass-loading regions, we will also use AMR to create a similarly-shaped refined grid encompassing any post-sonic mass-loading regions to help better resolve the shock.

4.3.2 Mass-Loading Setup

Like with our 1D hydrodynamic model, we divide our first 3D MHD mass-loading tests into two separate cases, but with each surrounding the magnetosonic point, which is at approximately the same location as the hydrodynamic sonic point in our MHD steady-state (in any MHD context we will refer to the magnetosonic point as simply the sonic point). Again, we have a subsonic case, where the mass-loading region begins prior to the sonic point, and a supersonic case, where the mass-loading region begins after the sonic point. We define the radial bounds of our mass-loading regions by $4.5\,R_\odot \leq r \leq 5.5\,R_\odot$ for the subsonic case and by $7.0\,R_\odot \leq r \leq 8.0\,R_\odot$ for the supersonic case, as summarized in Table 4.1.

Table 4.1: Mass-loading cases in the 3D coronal wind.

	r_{L}	r_{R}
Case 1	$4.5\,R_\odot$	$5.5\,R_\odot$
Case 2	$7.0\,R_\odot$	$8.0\,R_\odot$

As stated before, we will keep the ratio $P_{ml}/\rho_{t=0}$ for the mass-loading regions similar between the hydrodynamic and MHD cases. However, this ratio was not the same between the cases and sub-cases in the previous chapter. The calculated ratios for the hydrodynamic cases are listed in Table 4.2. Since we will not have sub-cases for each subsonic and supersonic MHD case, we will need to choose which hydrodynamic sub-cases to match with Case 1 and Case 2 from Table 4.1. MHD Case 1 will be matched with hydrodynamic Case 1b and MHD Case 2 will be matched with hydrodynamic Case 2a. We then have mass-loading factors of $P_{ml} = 6 \times 10^{-24}\,\mathrm{g\,cm^{-3}\,s^{-1}}$ and $P_{ml} = 4 \times 10^{-24}\,\mathrm{g\,cm^{-3}\,s^{-1}}$ at the inner radial mass-loading boundaries for MHD Case 1 and for MHD Case 2, respectively.

4.3.3 Mass-Loading Results

We first solve Equations 4.10-4.14 to find new steady-states for the described subsonic case (shown in Figure 4.4). We do not refine the grid further than in Figure 4.3 since we know from

Table 4.2: Mass-loading factor to local density ratios for the hydrodynamic cases.

	$P_{ml}/\rho_{t=0}$
Case 1a	$2.9 \times 10^{-5}\,\mathrm{s}^{-1}$
Case 1b	$1.0 \times 10^{-4}\,\mathrm{s}^{-1}$
Case 2a	$1.9 \times 10^{-4}\,\mathrm{s}^{-1}$
Case 2b	$2.9 \times 10^{-4}\,\mathrm{s}^{-1}$

the previous chapter there will not be a resulting shock. Once again we look at the resulting radial velocity and mean mass steady-state profiles, which are plotted in Figure 4.8.

For the supersonic case we refine the region to encompass our entire mass-loading region, in order the better resolve potential shocks, similar to the supersonic cases in Figure 3.5. A cross-sectional region of the refined grid in the xz-plane is plotted in Figure 4.9. Solving Equations 4.10-4.14 for this case yields the radial velocity and mean mass profiles plotted in Figure 4.10.

The first difference to point out is due purely to our additional AMR region for the post-sonic case. The two jumps preceding the shock in the velocity curve are non-physical artifacts resulting from larger numerical errors generated at the boundary between grids of different resolution. This type of discontinuity is inherent in any discretization scheme with a non-uniform grid, and although their magnitude can be reduced, they cannot be completely removed from our solutions. The same discontinuity occurs when transitioning back to the coarser grid, though not as prominent. This can be seen in both the radial velocity and mean mass profiles.

While the velocity profiles in Figures 4.8 and 4.10 share several similarities with Figure 3.5, such as the shock and reacceleration for the post-sonic case and upwind velocities reduction for the pre-sonic point case, there are dramatic differences in the mean mass profiles proceeding the mass-loading regions. In the hydrodynamic model the greatest mean mass is accomplished with the mass-loading region located furthest from the Sun and reaches approximately 0.75 $\mathrm{m_p}$. The mean masses reached with the MHD model are not only much greater, but the trend is reversed, with the pre-sonic point mass-loading region resulting in a greater mean mass. A likely contributing factor is the lower undisturbed solar wind speed relative to the 1D hydrodynamic model, with an

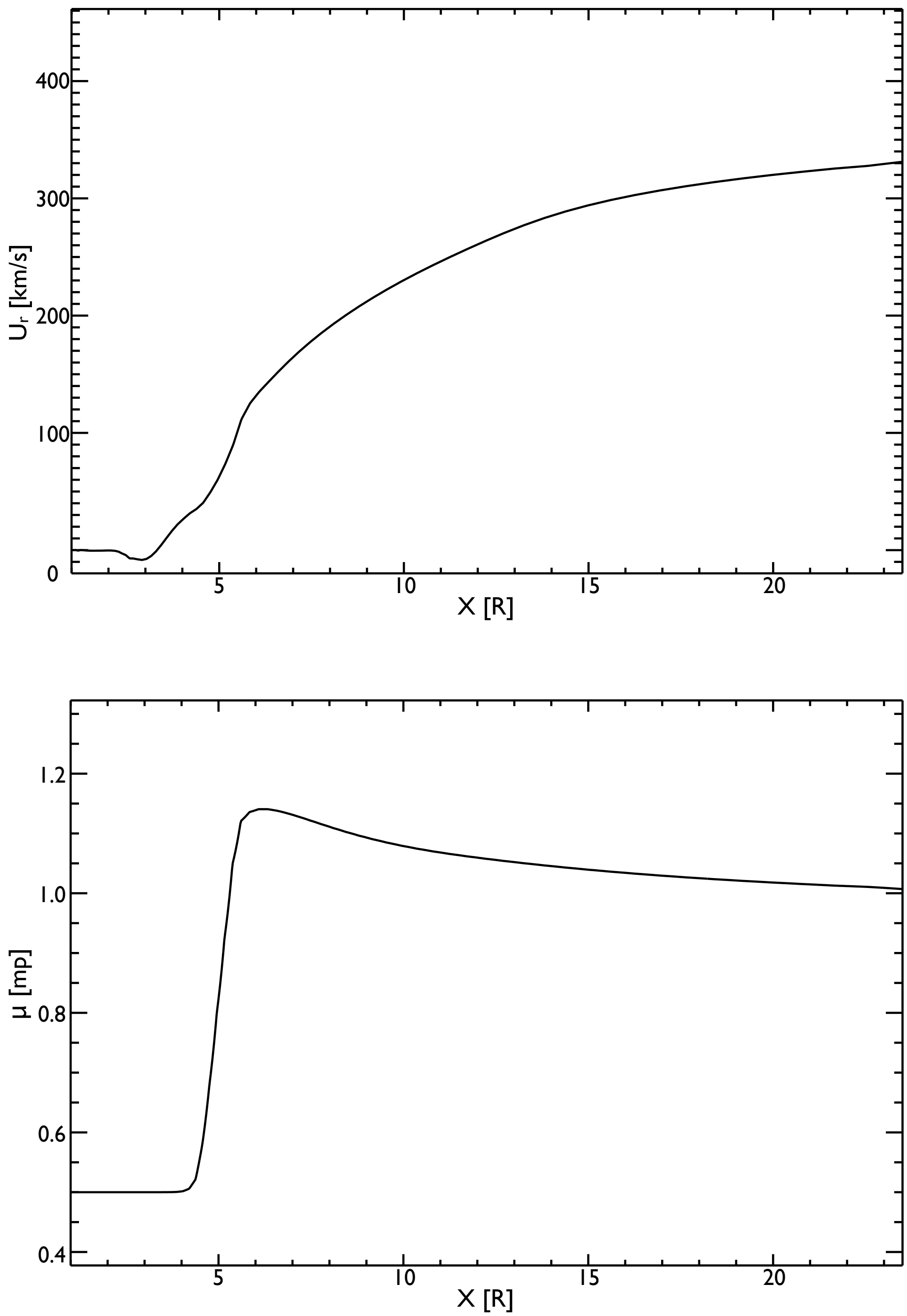

Figure 4.8: Radial velocity (top) and mean mass (bottom) profiles for Case 1, mass-loading the solar wind between $4.5\,R_{\odot} \leq r \leq 5.5\,R_{\odot}$. Both profiles correspond to the subsonic cases used in Figure 3.5.

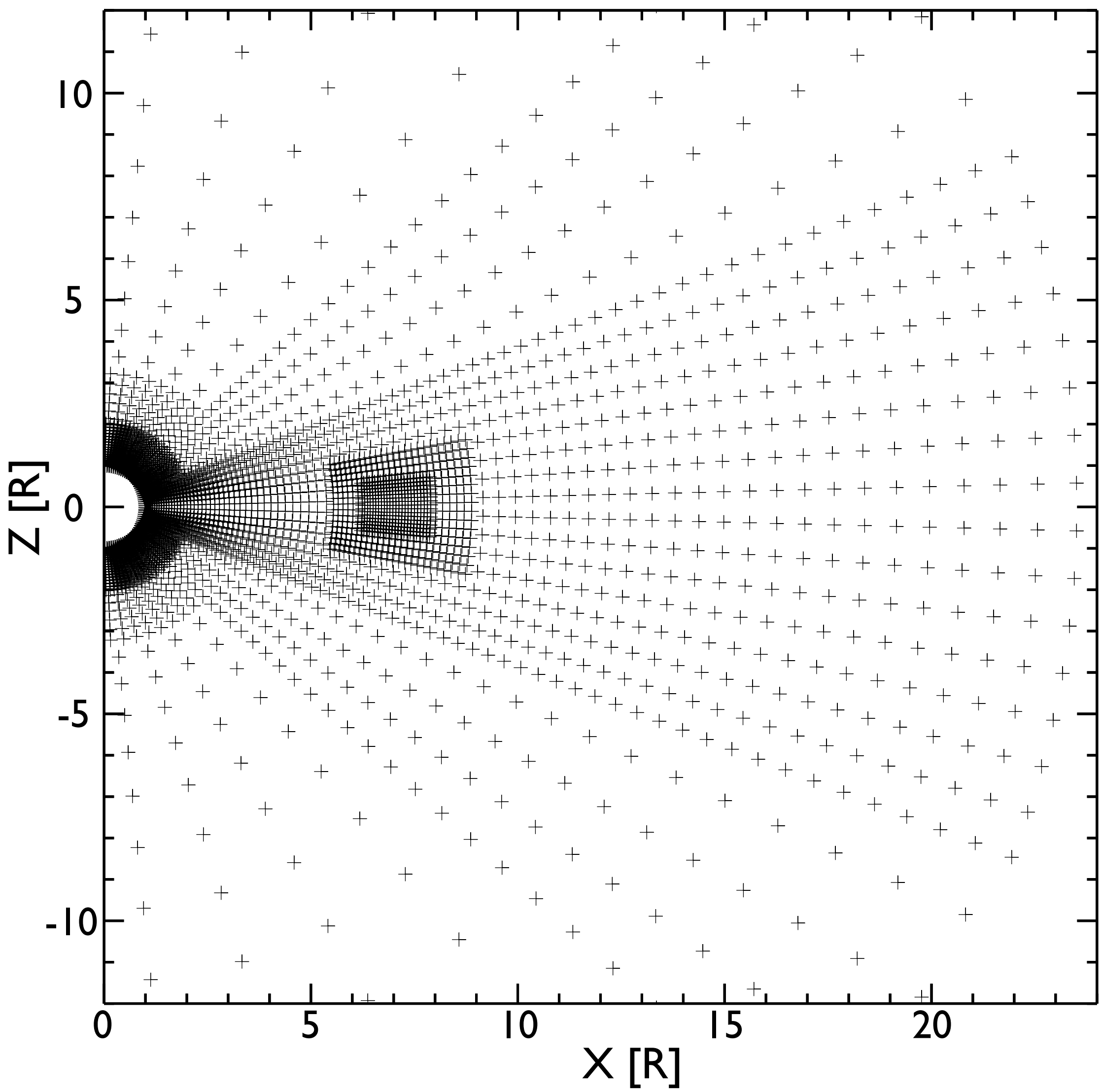

Figure 4.9: The spatial grid in the xz-plane used for the post-sonic point case, with a z-centered AMR region encompassing the mass-loading region.

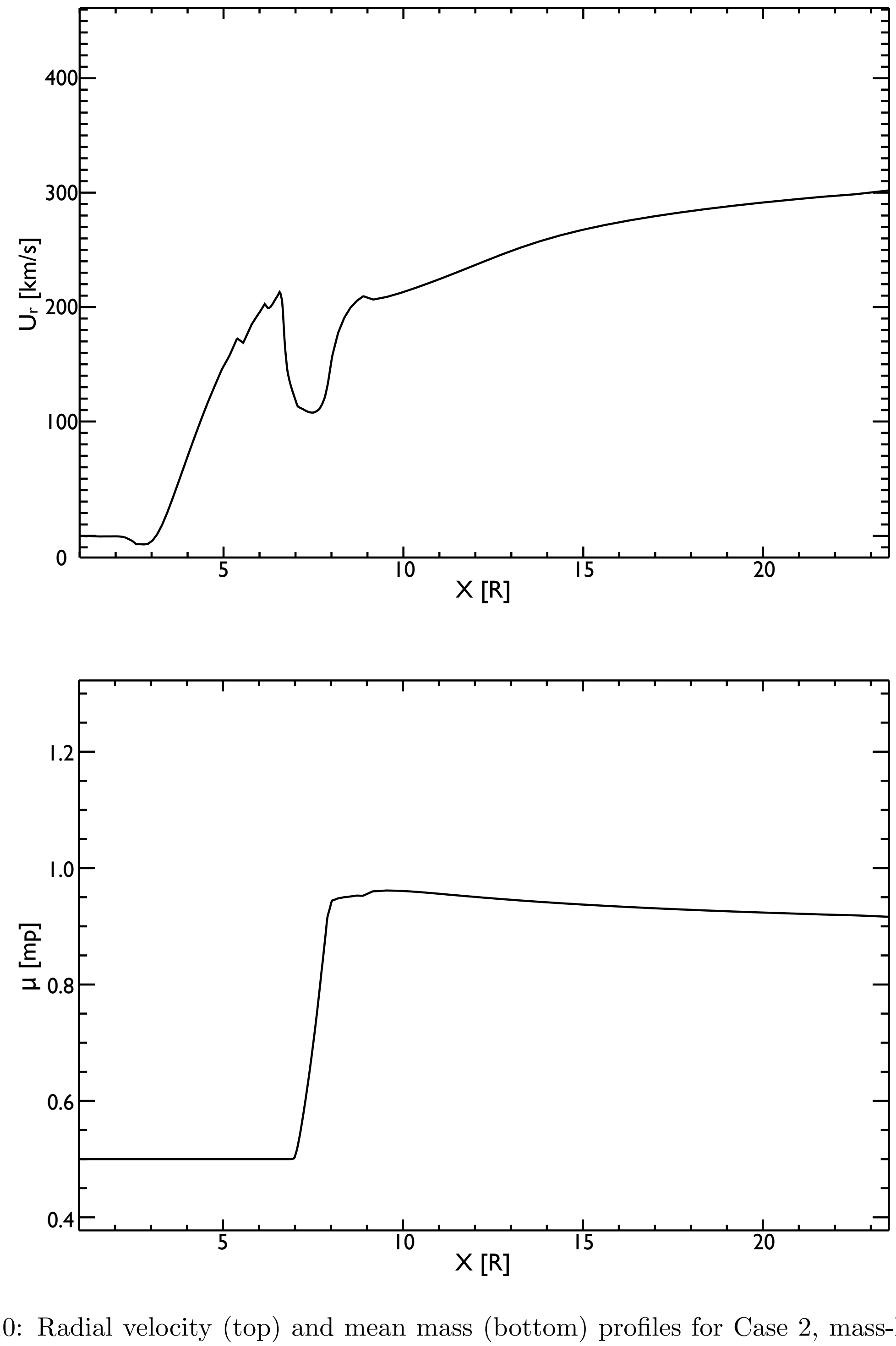

Figure 4.10: Radial velocity (top) and mean mass (bottom) profiles for Case 2, mass-loading the solar wind between $7\,R_{\odot} \leq r \leq 8\,R_{\odot}$. Both profiles correspond to the supersonic cases in Figure 3.5.

increasing difference closer to the Sun. The lower velocities are less effective at transporting ionized dust particles, allowing additional build-up in the mass-loading regions, though other factors may contribute to the increased mean mass.

While Figures 4.8 and 4.10 are useful for comparisons with 1D hydrodynamic results from Chapter 3, the MHD model allows us to look magnetic field properties of the mass-loaded solar wind. Figure 4.11 shows the new magnetic field structure in the xz-plane for both cases. Magnetic field lines tend to curve around the ring-shaped mass-loading regions, though this is more prominent for Case 2 (bottom). Looking at the magnetic field strength along the x-axis for both cases (Figure 4.12) shows a magnetic build-up preceding both mass-loading regions, followed by a drop in magnetic field strength, which agrees with the diverging field lines within the mass-loading regions in Figure 4.11.

By using the mass-loading model presented in earlier chapters, we have successfully extended the SC component described in van der Holst et al.[49], with the development of this modified SC component described in Rasca et al.[39]. This opens up for a variety of coronal wind mass-loading applications. For the remainder of this thesis we will explore one particular application, resulting from bursts of dust particles into the coronal wind by sungrazing comets.

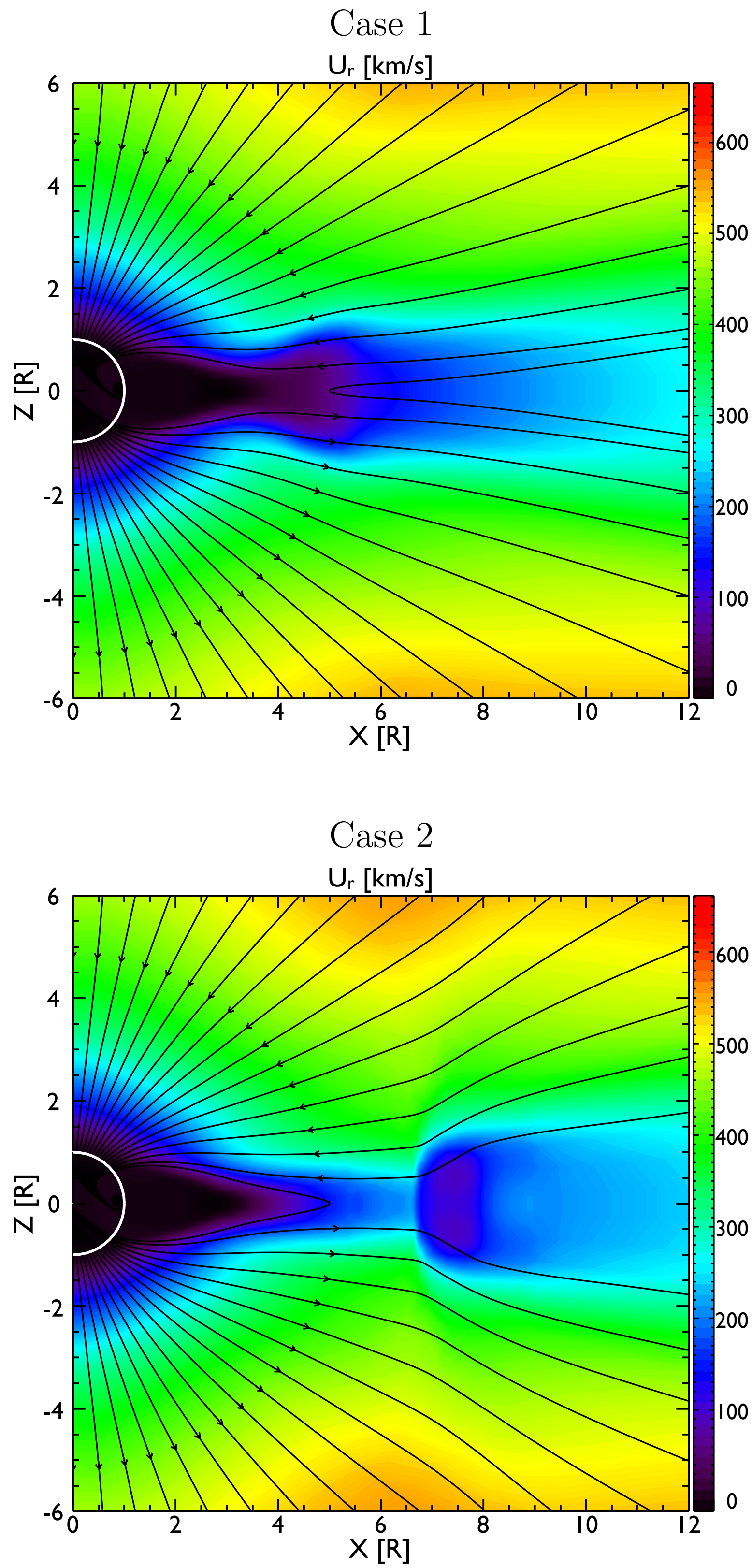

Figure 4.11: Magnetic field lines plotted over the radial velocity in the xz-plane for both Case 1 (top) and Case 2 (bottom). A divergence of magnetic field lines around each mass-loading region is evident in both cases.

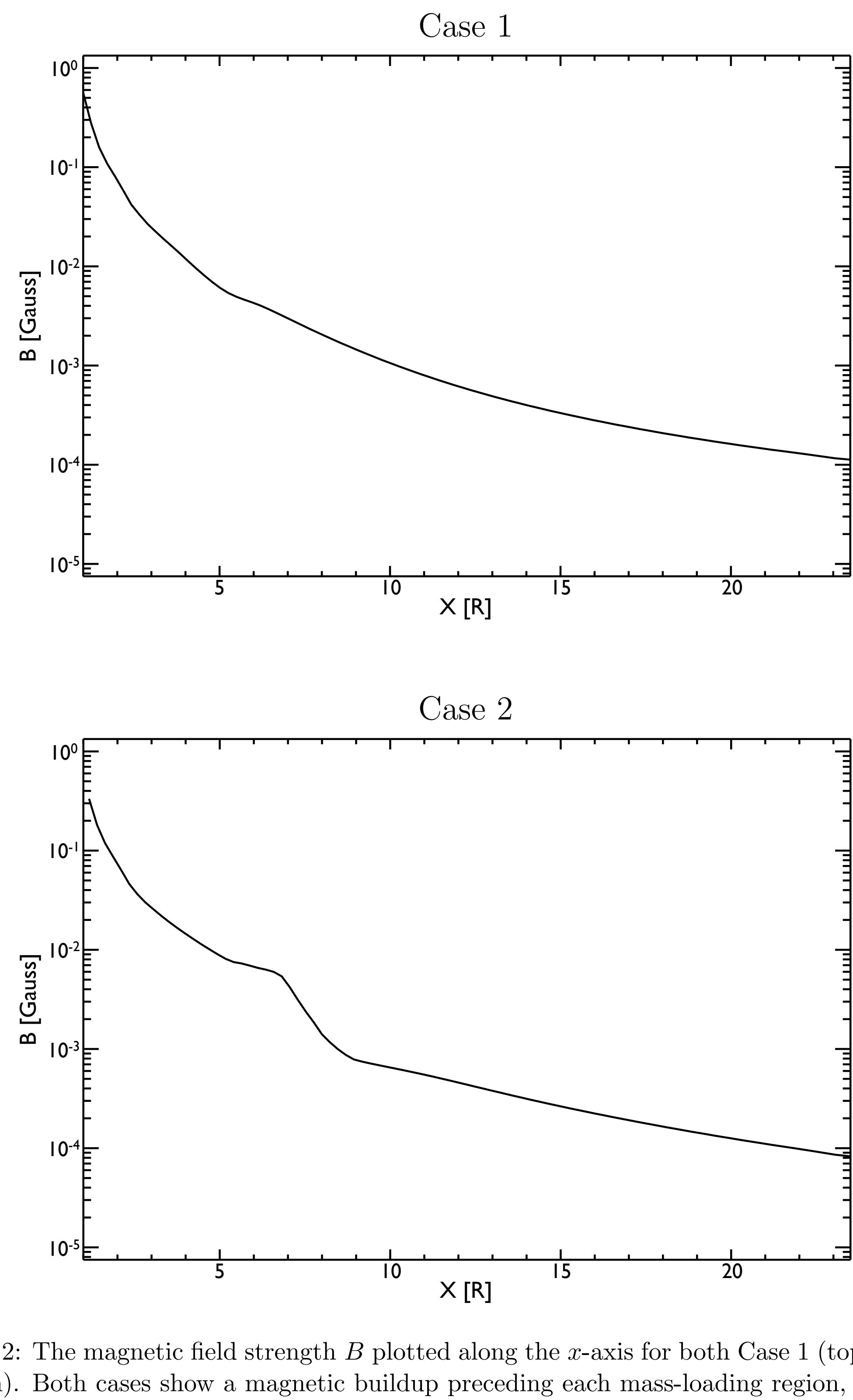

Figure 4.12: The magnetic field strength B plotted along the x-axis for both Case 1 (top) and Case 2 (bottom). Both cases show a magnetic buildup preceding each mass-loading region, followed by a drop in field strength, corresponding to diverging magnetic field lines in the regions.

Chapter 5

A Cometary Dust Source Application

5.1 Sungrazing Comets

In addition to particle migration to the F-corona, another means for dust to find its way into the corona is through sungrazing comets that emit dust and gas near the Sun. Comets venturing in so close to the Sun can lose significant mass from a single pass, if they survive at all. On December 15, 2011 Comet C/2011 W3 (Lovejoy) passed within $0.2\,R_\odot$ of the solar surface, significantly reducing its mass and leading to a cataclysmic fragmentation days later (Sekanina and Chodas[44]). Such a loss in mass could potentially create observable impacts to the wind velocity and composition. Modeling solar wind mass-loading from a sungrazing comet such as Comet C/2011 W3 serves as our first application for modeling mass-loading within a full 3D MHD environment.

5.2 Mass-Loading Point Source

With a functioning mass-loading component established with the SWMF, we move to approximating a mass-loading region as a single point source on a cometary path. However, when working with computational grids, we must settle for a single computational cell acting as our "point" source. This should be sufficient if the cell volume is comparable in size to a cometary coma, the dusty atmosphere that can range in size from 10^4 to 10^5 km across.[1] Images provided in Sekanina and Chodas[44] and taken by Černý (Figure 5.1) show the head of Comet C/2011 W3

[1] In the extreme case of 2007's Comet 17P/Holmes, the coma expanded to a volume greater than the Sun.

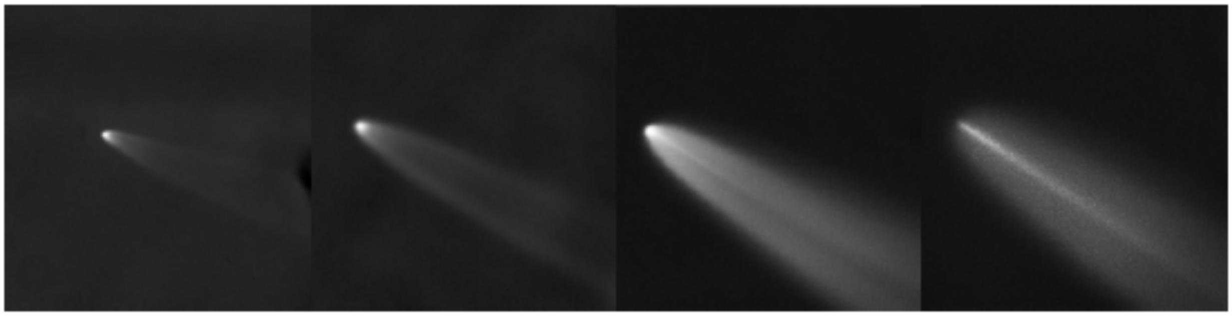

Figure 5.1: The growing coma and tail of Comet C/2011 W3, following a day after a close approach to the Sun. Images are reproduced from Sekanina and Chodas[44].

to be several 10^4 km in width a day after perihelion.

5.2.1 Comet Lovejoy Orbital Characteristics and Mass Loss Estimate

For the first simulations of our sungrazing comet application we place a dust source at various locations along a cometary path using the same orbital characteristics as Comet C/2011 W3, but restricted to the equatorial plane, eliminating the need to add extra refinement outside the current sheet. Sekanina and Chodas[44] provide orbital characteristic for Comet C/2011 W3, which has a perihelion distance of $r = 1.2\,R_\odot$. We also use $t = 0$ as the reference time for its perihelion passage. We will look as locations along its path and refine the grid such that each cell volume acting as our "point" source will be approximately the same as a spherical coma with radius 10^4 km.

In addition to orbital characteristics, we obtain dust loss estimates for Comet C/2011 W3 from Sekanina and Chodas[44]. Using post-perihelion light curve data they find an effective cross-sectional area X_d of the dust in the cloud. This is then used in their model to estimate the mass loss indicated by the scattered sunlight by dust particles of diameter d with a size distribution d^{-k},

$$M_d = \begin{cases} \frac{2(k-3)}{3(4-k)}\Theta\rho_{\text{bulk}}X_d d_{\text{min}}^{k-3}d_{\text{max}}^{4-k} & 3 < k < 4 \\ \frac{2(k-3)}{3(k-4)}\Theta\rho_{\text{bulk}}X_d d_{\text{min}} & k > 4 \end{cases}, \tag{5.1}$$

which is an overestimate due to the contribution of sodium ions in the light curve. Equation 5.1 is for a specific range in dust particle sizes, from d_{min} to d_{max}, and where $\rho_{\text{bulk}} = 0.4$ g cm^{-3} is the bulk dust density for dust from Comet C/2011 W3 and Θ is the coefficient

$$\Theta = \frac{1 - (d_{\min}/d_{\max})^{|k-4|}}{1 - (d_{\min}/d_{\max})^{k-3}}. \tag{5.2}$$

Sekanina and Chodas[44] state particles smaller than 0.1 μm contribute very little to the mass, making $d_{\min} = 0.1$ μm. For $d_{\max}$, multiple values are used in their study, but we set $d_{\max} = 100$ μm since it is an upper limit for dust particles getting picked up by the solar wind, and $k = 3.5$, which also gives an upper estimate for the total mass. Due to the light curve being much stronger post-perihelion than during pre-perihelion, the dust is presumed to be released during the two days following perihelion. With these parameters we have a total mass loss of approximately 3×10^9 kg over that time period.

5.2.2 Mass-Loading Setup

We set up our simulations for modeling mass-loading due to a sungrazing comet in the following manner. We assume the estimated mass loss of 3×10^9 kg is evenly distributed between post-perihelion times $t = 0$ and $t = 48$ hours, which gives a mass loss rate of about 1.7×10^4 kg/s. This mass loss rate will be used as the mass-loading rate in the computational cell acting as our "point" source. Then, at four points on the orbit between perihelion ($x = 1.2\,R_\odot$) and the edge of our domain ($r = 24\,R_\odot$), time-independent solutions are found using the specified mass-loading rate.

For each point used along the orbit that is not contained in a cell satisfying the volume requirement discussed earlier, their blocks will be refined until such condition is met. Figure 5.2 shows the refined grid in the xy-plane for three cometary time locations t_C we will be using, which are $t_C = 12$, 18, and 24 hours (post-perihelion). A fourth location we will look at, at $t_C = 6$ hours, is close enough to the Sun that no extra refinement is needed.

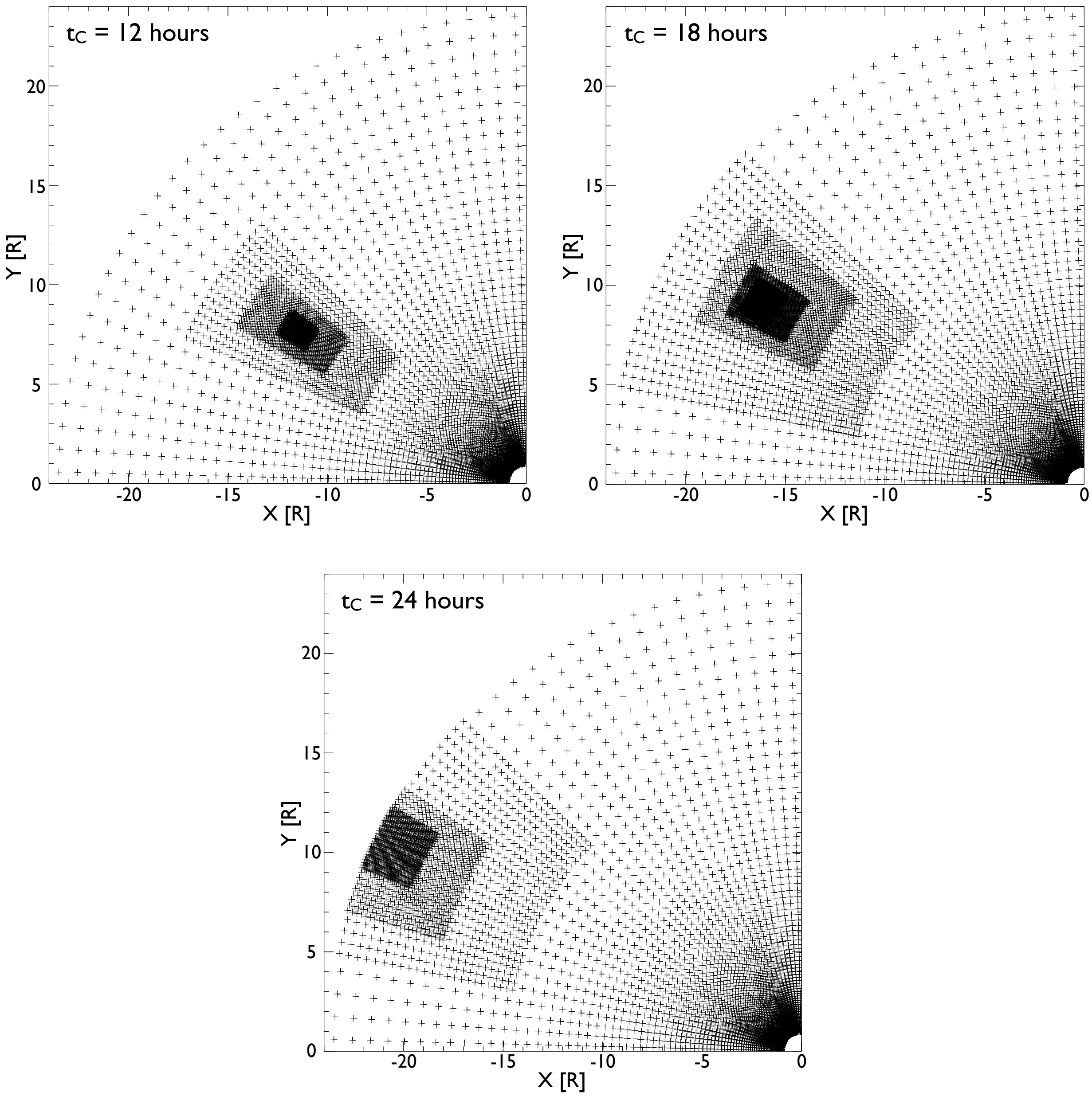

Figure 5.2: Grid refinements in the xy-plane for three different comet locations, corresponding the post-perihelion times $t_C = 12$, 18, and 24 hours.

5.2.3 Mass-Loading Results

Figure 5.3 shows solutions from our four different time locations, $t_C = 6$, 12, 18, and 24 hours. This source orbits counterclockwise in the xy-plane, as viewed from above, and much like with our previous results a sudden localized deceleration occurs, with reacceleration downwind. The panels start at $t_C = 6$ hours since any effects much closer to the Sun will become lost due to the much higher solar wind density. For example, at $t_C = 6$ hours, only minute changes can be seen in the velocity contours beyond $r = 10\,R_{\odot}$. For $t_C = 18$ and $t_C = 24$ hours, the resulting drop in velocity remains approximately the same, even though a drop in the solar wind density with increasing r should result in a more pronounced velocity change if the mass-loading rate remains constant.

5.3 Dust Tail Dynamics and Formation

On the spatial scales used, our assumption of a cometary body being a dusty point source seems reasonable. However, in a more realistic situation dust particles may survive being picked-up long after ejection from their cometary parent. This has been clearly evident over centuries of observations, in which light scattering off dust particles generates occasionally magnificent cometary tails, such as with Comet C/2006 P1 (McNaught) in Figure 5.4.[2] Here we will cover how dust tails are dynamically formed, defining a new mass-loading region we can use in our MHD simulations.

Particles ejected from their cometary parent are subject to two basic forces: gravitational forces from the Sun and forces resulting from radiation pressure. The ratio of the two forms a particle's β value, defined in Equation 1.27, and tells us the dominating force on a particle. Each particle of a specific size and mass has its own β value, which we will use to distinguish between dust particle species. Smaller particles have a large β, while larger, more massive particles have a very small β. Consequently, β determines the type of orbit ejected particles will inherit: elliptical ($\beta < 1$), hyperbolic ($\beta > 1$), or simply a straight path resulting from balancing forces ($\beta = 1$).

[2] A cometary body actually forms two types of tails: a curved dust tail and a plasma ion tail, the latter being made of ionized gases released from the comet, pointing directly away from the Sun. However, we will only be concerning ourselves with dust tails for now, since different physical processes are involved with mass-loading ion tails.

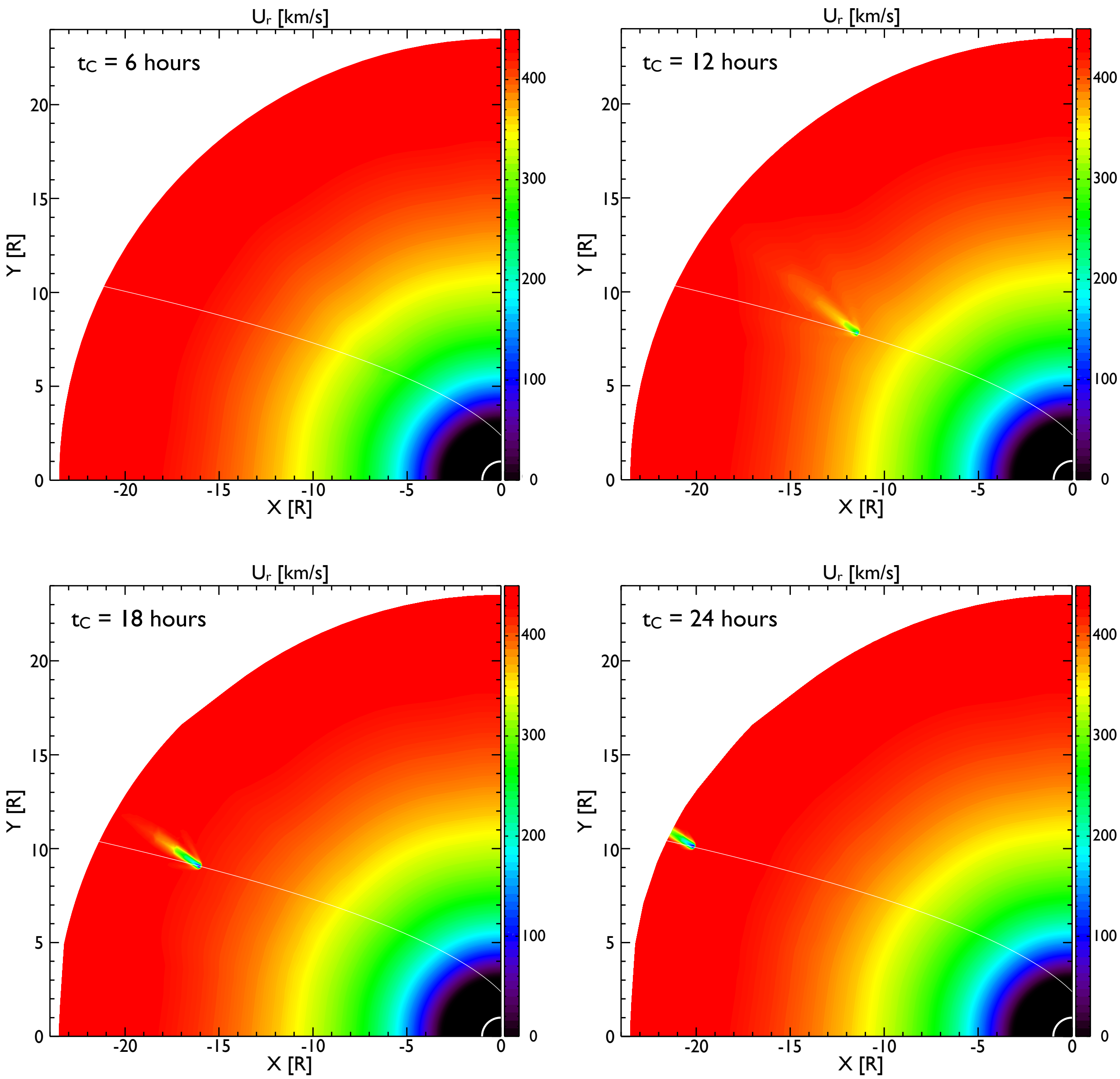

Figure 5.3: Radial velocity results from using the SC component to place a dust point source along a sungrazing cometary orbit (white curve) in the xy-plane, with a mass loss rate of 1.7×10^4 kg/s. The four panels correspond to $t_C = 6$, 12, 18, and 24 hours.

Figure 5.4: The dust tail of Comet C/2006 P1 (McNaught), viewed from the Southern Hemisphere in 2007. Views of its magnificent tail gained it the nickname the “Great Comet of 2007”.

Now imagine particles of various sizes being ejected at $t = t_0$ from Comet C/2011 W3's orbit with zero relative velocity. While initially occupying the same location in space, variations in post-ejection trajectories separate the particles over time, forming an elongating curve of particles corresponding to the ejection time. Several of these curves, called synchrones, exist for each time of dust particle ejections. Another curve, called a syndyne, is also formed, but instead consists of dust particles of the same species but ejected at various times. Unlike with synchrones, for a time t_C in the cometary orbit all syndynes remain connected to the cometary orbit.

Figure 5.5 shows an example of a synchrone curve at time $t_C > t_0$ along the cometary orbit, with dust particles being initially ejected at the comet's perihelion ($t = t_0$), and a syndyne curve also at t_C, formed by all the particles of a specific β ejected during $t_0 \leq t \leq t_C$. Varying β for syndyne curves and varying the ejection time for synchrone curves creates a tail region, like the one shown in Figure 5.6. This syndyne/synchrone-generated dust tail is what is seen in images such as Figure 5.4 when light is scattered by the dust particles, and their construction is also described by Mendis et al.[29]. Dust tails generally remain in the comet's orbital plane, but migrate away from

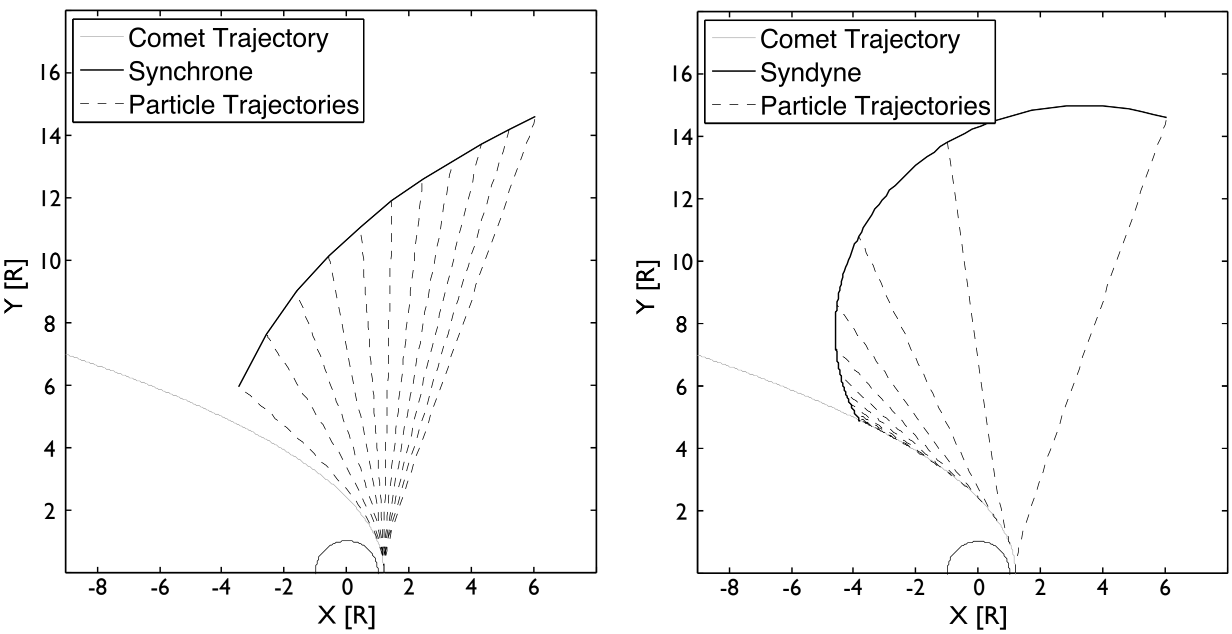

Synchrone Syndyne

Figure 5.5: Examples of a cometary synchrone (left) and syndyne (right). Dashed lines correspond to particle trajectories for their respective synchrone or syndyne. For the synchrone, each particle trajectory corresponds to a difference dust particle species, with each species defined by their β value, but with all particles ejected at the same time/location (perihelion, in the illustrated example). For the syndyne, all trajectories are for the same species of particle, but each corresponds to a different time of ejection.

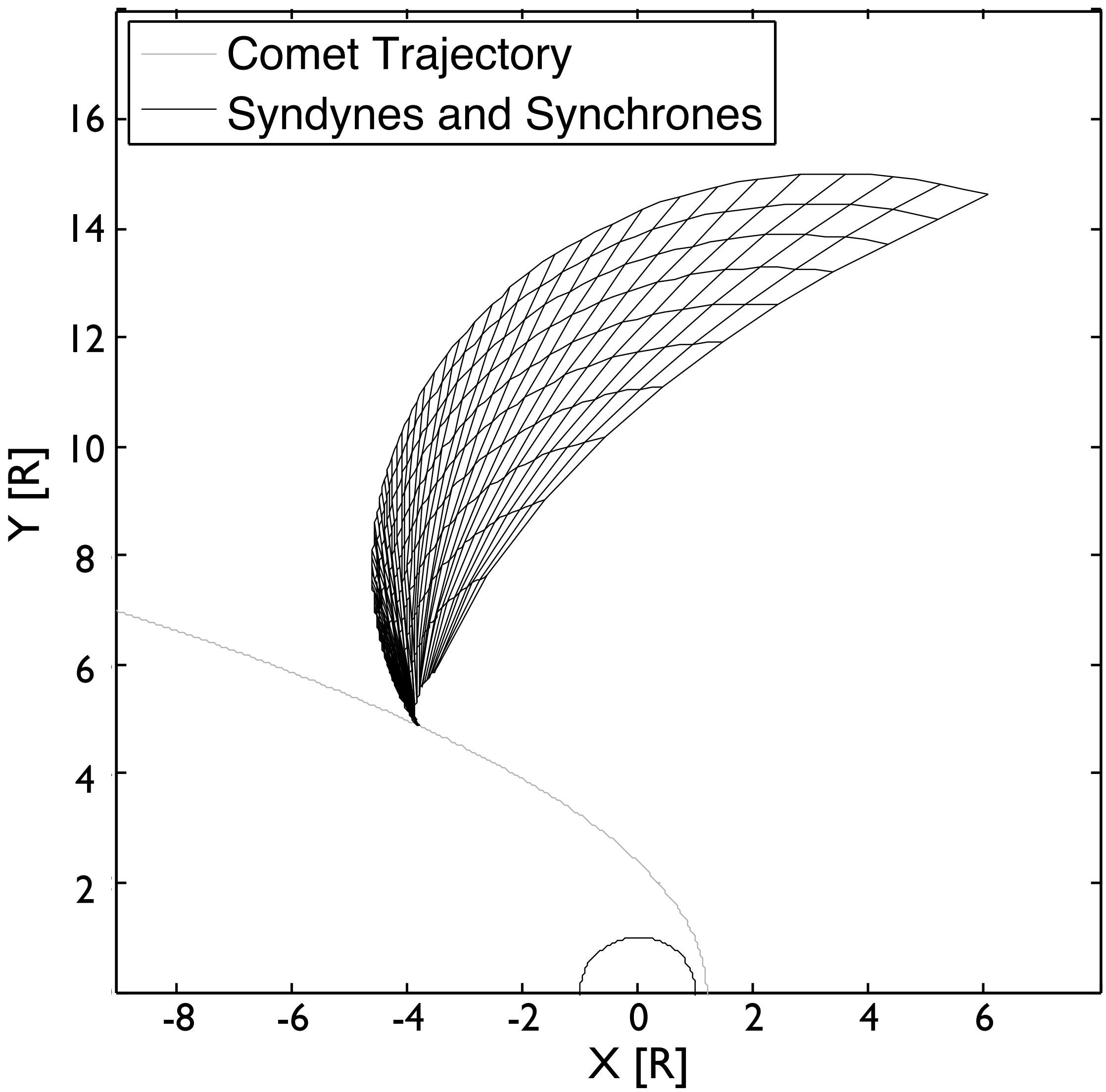

Figure 5.6: An example of a syndyne/synchrone-defined dust tail along Comet C/2011 W3's orbit. The curves, corresponding to 4 hours after perihelion, are generated with the assumption that various species of dust particles are ejected from the cometary body at several points in time beginning at perihelion.

it further out due to perturbations and non-zero relative speeds during ejection.

5.4 Mass-Loading Dust Tail

Defining a dust tail in the previous section now provides a more realistic mass-loading region than the point sources used previously. A series of syndyne and synchrone curves, such as those in Figure 5.6, define the new mass-loading regions for revisiting the post-perihelion mass-loading cases from earlier in the chapter. And fortunately, we need not concern ourselves too much with particle drift outside the orbital plane. Our grids introduced in Figure 5.2 will actually help account for any slight particle drift outside the orbital plane since the cell dimensions increase with distance from the cometary body and therefore cover more volume outside the orbital plane.

In addition to the newly-defined mass-loading region, mass distribution in the tail needs to be considered. The mass distribution is determined by two factors. First, the trajectories of various species of dust particles make the particle distribution non-uniform. Second, the distribution of particle size, which was introduced in the previous section, must be used in conjunction with particle number distribution to determine final mass distribution estimates, which we then use in new MHD simulations.

5.4.1 Syndyne/Synchrone-Defined Dust Tail

To determine new tail-shaped mass-loading regions and particle distributions for the $t_C = 6, 12, 18,$ and 24 hour cases from our point source results, we first assume uniform ejection of dust particle size, once again ranging from $d = 0.1\,\mu$m to $d = 100\,\mu$m.[3] For each case, we then eject particles periodically along the cometary orbit between $t = 0$ and $t = t_C$, assuming the only forces acting on the particles result from solar gravity and radiation pressure. At $t = t_C$, synchrones for each ejection time and syndynes for each particle species are determined, along with coordinates for tracked dust particles.

Figure 5.7 shows distributions for ejected dust particles at each of our four post-perihelion

[3] Particles smaller than $0.1\,\mu$m behave differently due to more influence from magnetic fields.

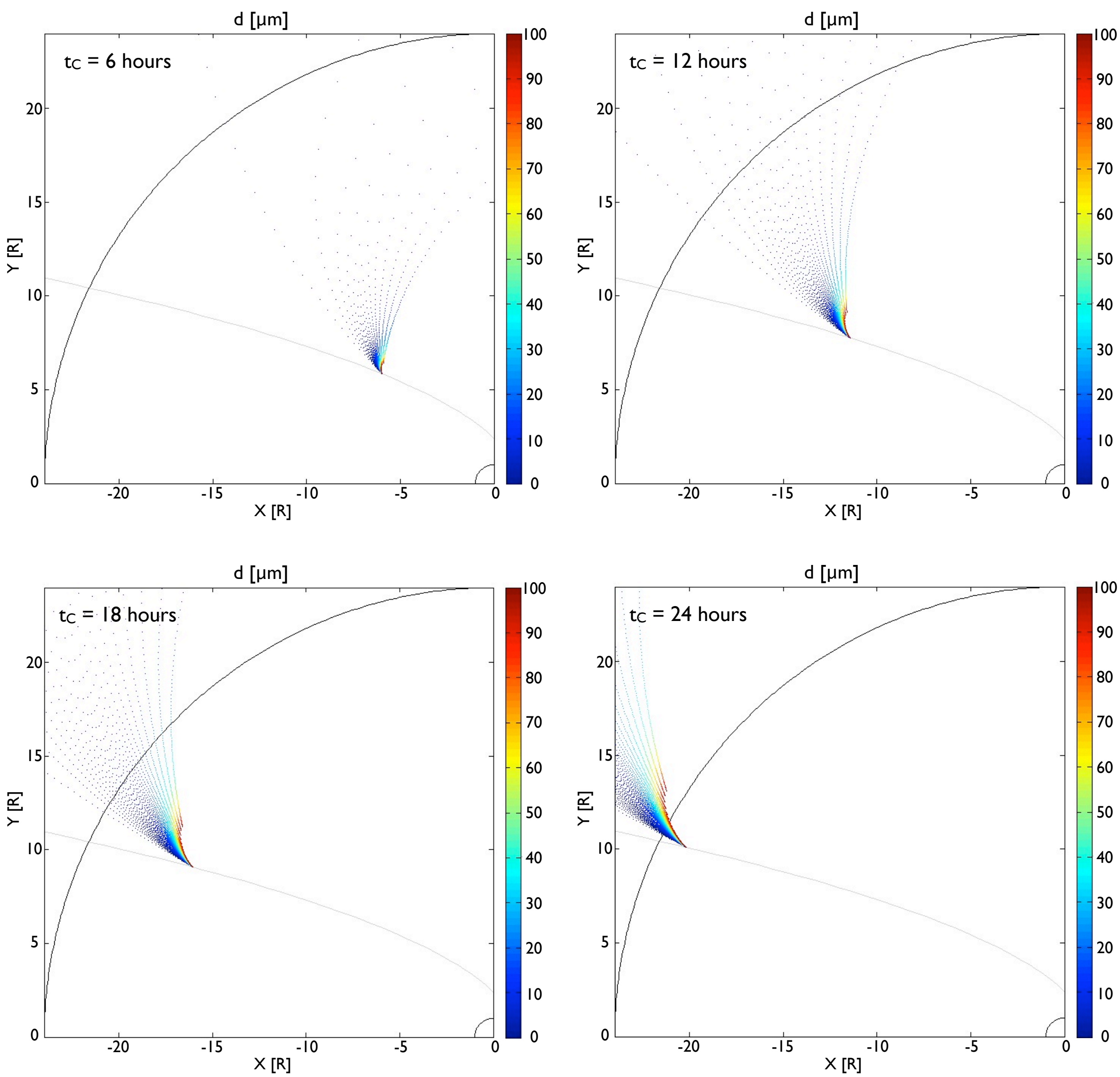

Figure 5.7: Tail-shaped mass-loading regions and particle distributions used to update results for the four cases from Figure 5.3. The particles are colored according to their diameter d, ranging from $d = 0.1\,\mu m$ to $d = 100\,\mu$m. The solar surface, cometary orbit, and outer boundary of the SC component domain are drawn.

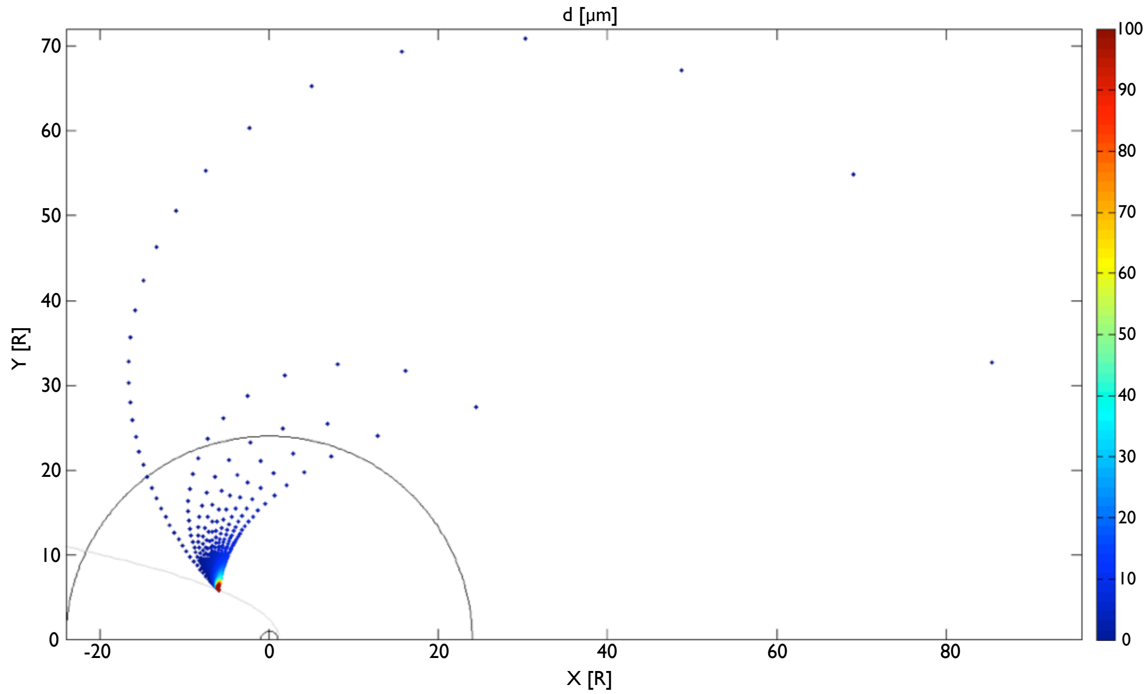

Figure 5.8: A wider view of the tail-shaped mass-loading region and particle distribution for the $t_C = 6$ hours case, showing the dust tail in its entirety.

times t_C. The particles are colored according to particle diameter d. Being mostly influenced by gravity, the massive particles (in red) remain near their cometary parent. The least massive particles (in blue) form hyperbolic orbits that take them far from the Sun astonishingly fast. While the entire tails are not shown in Figure 5.7, Figure 5.8 shows an example of the whole tail for $t_C = 6$ hours, with the outer boundary $r = 24\,R_\odot$ drawn, showing the extent of the outward migration of the smallest dust particles.

5.4.2 Mass-Loading Setup

Using the mass-loading regions just defined for the four time cases t_C used in our point source MHD simulations, we rerun the SC component with a more realistic spread of dust particles. This is done by taking the particle distributions in Figure 5.7 and reading them into our modified SC component described previously. The initial particle size distribution d^{-k}, with $k = 3.5$, is then used to determine the overall mass distribution within the region, which we calculate our mass-loading source with.

We initially keep the overall mass loss rate the same as in our point source simulations, where dust is lost to the solar wind at a rate of 1.7×10^4 kg/s during the first two days following perihelion. This is done by normalizing our mass-loading source and scaling it to allow the appropriate mass-loading rate. The result is a mass-loading rate equal to that used with our point source, but spread out across our new mass-loading region.

5.4.3 Mass-Loading Results

Figure 5.9 shows the new radial velocity steady-state solutions from using the SC component with the tail-shaped mass-loading regions described. The mass-loading rate remains the same as in Figure 5.3, but the mass is more spread out. The result is only a slight change in radial velocity, the drop maxing out at around 100 km/s for $t_C = 18$ and $t_C = 24$ hours, with no visible change for $t_C = 6$ hours. Additionally, we do no see any visible effect that the shape of the mass-loading region is having on the radial velocity. The results could easily be mistaken for mild mass-loading point sources.

The next question anyone working with numerical models would ask is, what happens if we scale up the mass-loading source further? Figure 5.10 partially answers that question, where our mass-loading source $\mathbf{S}_d$ has been multiplied by a factor of 10. Since cometary bodies can vary greatly in both size and evaporation, an order of magnitude difference in mass loss is reasonable. The next major sungrazing comet, Comet C/2012 S1 (ISON), is estimated to be much larger than Comet C/2011 W3, possibly large enough to survive perihelion (Knight and Walsh[23]). The mass-loading results are now similar to those from Figure 5.3, though there are still no features indicating the tail-shaped aspect of the mass-loading region.

Finally, we check if the tail-shaped mass-loading region is an improvement on the point source method. We know the realistic spread of the dust particles is great enough to reduce the impact on the solar wind, which we must assume for the time being is closer to the actual impact a sungrazing comet would have. However, the area that is clearly affected by the sungrazing comet in our radial

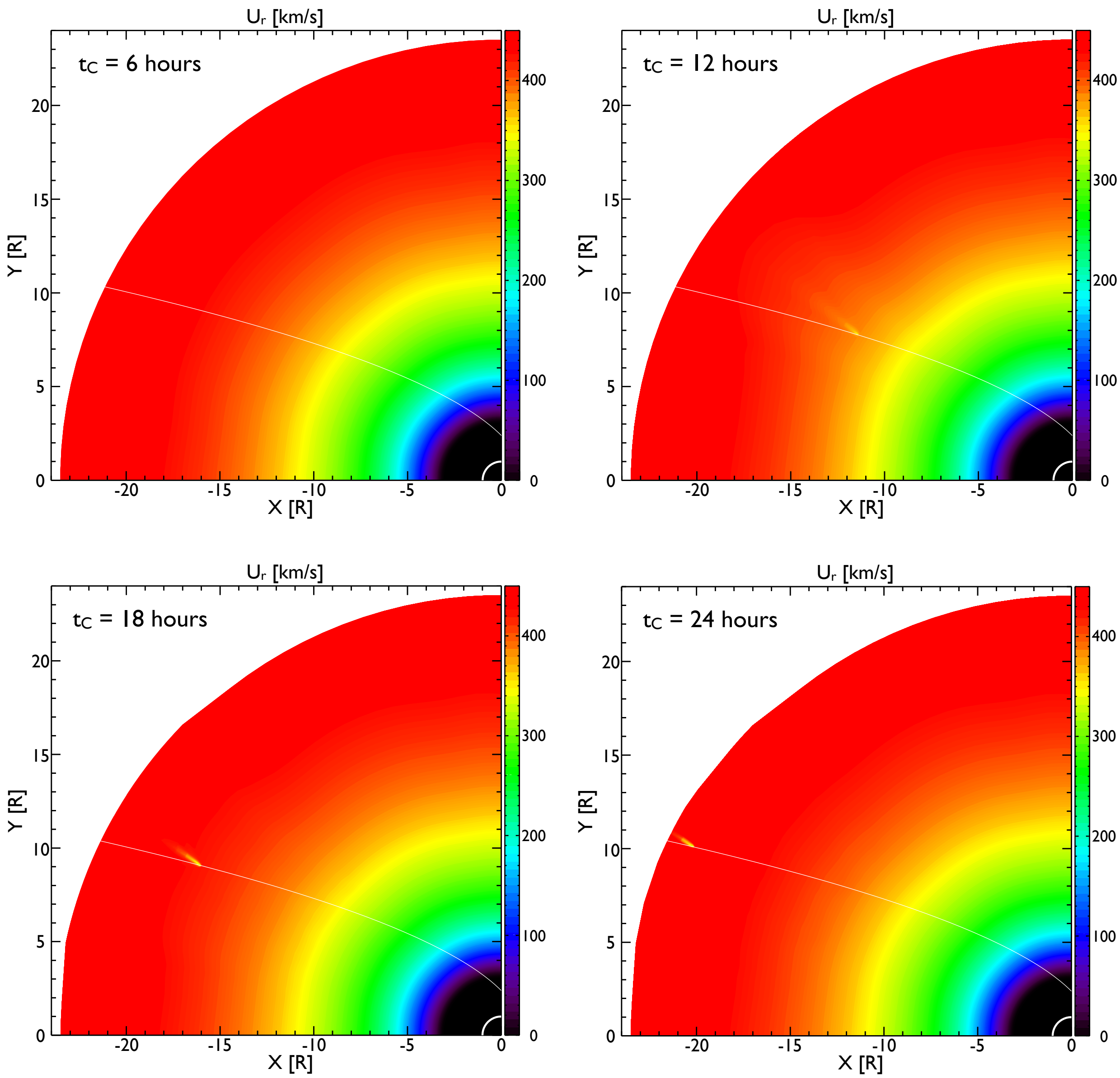

Figure 5.9: Radial velocity results from using the SC component to place a dust tail-shaped source along a sungrazing cometary orbit (white curve) in the xy-plane, using a mass loss rate of 1.7×10^4 kg/s. The four panels correspond to $t_C = 6$, 12, 18, and 24 hours after perihelion.

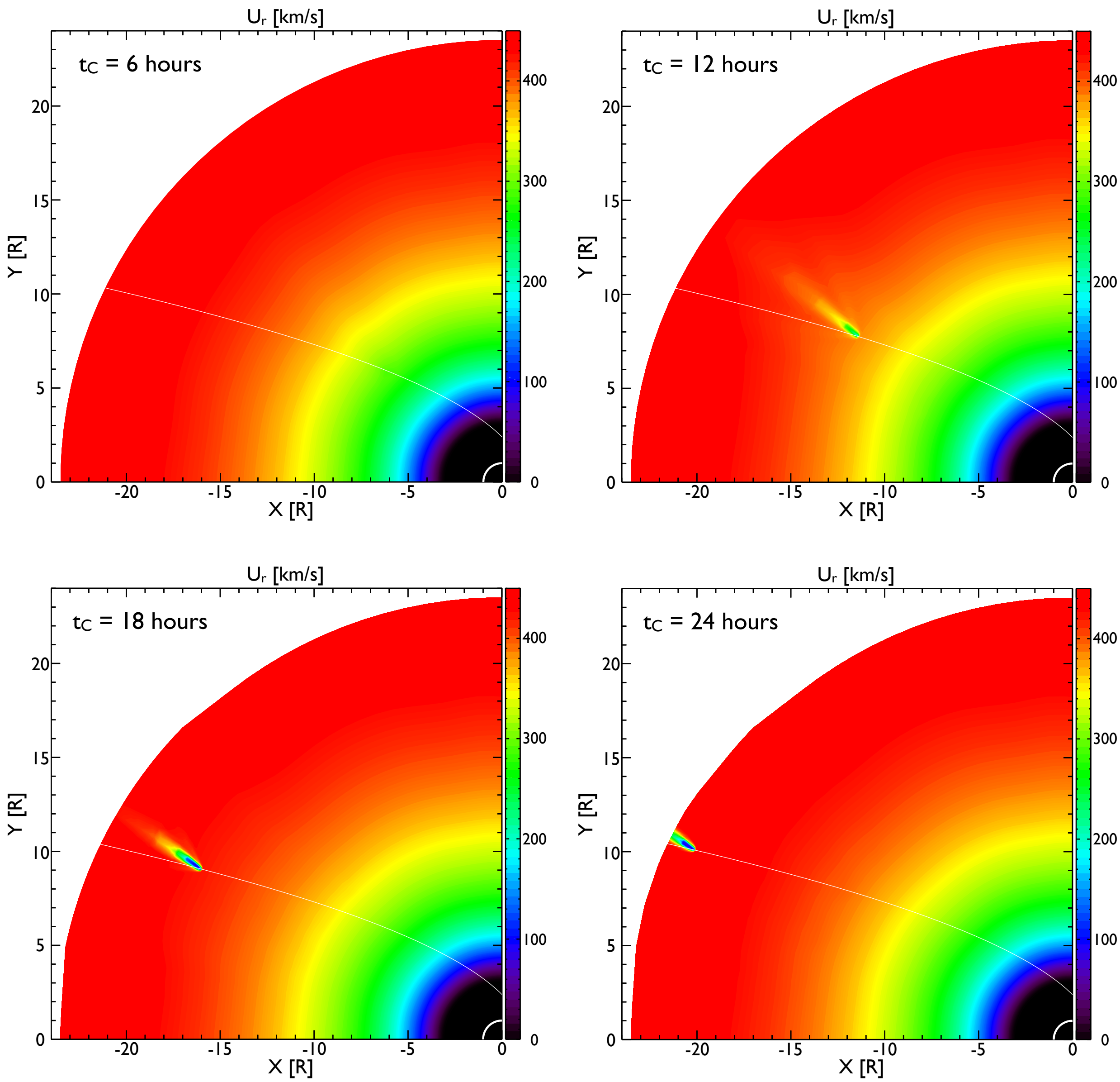

Figure 5.10: Radial velocity results from using the SC component to place a dust tail source along a sungrazing cometary orbit (white curve) in the xy-plane, using a mass loss rate of 1.7×10^5 kg/s. The four panels correspond to $t_C = 6$, 12, 18, and 24 hours after perihelion.

velocity plots is the same for both types of mass-loading regions, meaning the number of particles still concentrated near the cometary body outshines the number of particles carried further away by their trajectories. To actually see a velocity drop affecting the solar wind in a curving tail region, our mass-loading source would need to be scaled up $\times 10^3$, but then the solar wind immediately surrounding the cometary body becomes backed up enough to begin flowing upwind.[4] In a sense, we would be "breaking" the solar wind by the time we see a curving dust tail in the radial velocity results.

5.5 A Solar Probe's View

We now address the planned Solar Probe Plus (SPP) mission, which will be taking direct observations of the solar corona within the next decade. Planned to launch in 2018, SPP will spend seven years orbiting the Sun, making several passes through the solar corona. SPP's closest approach will take it near $8.5\, R_{\odot}$ from the solar surface[1]. Figure 5.11 shows a radial velocity plot in the xy-plane with three SPP approaches overlaid and the four t_C points in the cometary orbit we have been looking at.

The three approaches shown in Figure 5.11 highlight the potential for taking observations near a mass-loaded coronal wind. If a sungrazing comet is upwind of a passing solar probe, it may be capable of detecting the changes in the solar wind we have been modeling. With two of the SPP passes being immediately downwind of two of our cometary locations,[5] we can look at the changes in the solar wind such a probe may detect. For the $t_C = 12$ and $t_C = 18$ hour cases from Figure 5.9, we plotted their nearest respective downwind SPP paths, along with three shifted paths from the original, in both radial density and solar wind density[6] plots (Figure 5.12). The additional paths give us an idea of how changes in the solar wind appear to the probe with distance from a cometary source.

---

[4] Results not shown.

[5] The case for $t_C = 6$ hours is omitted since it does not generate a significant observable impact on the coronal wind.

[6] We do not look at the mean molecular mass for these cases, as we are no long assuming only three species of particles, but instead a spectrum of dust particle sizes. Looking at the overall density relative to the undisturbed

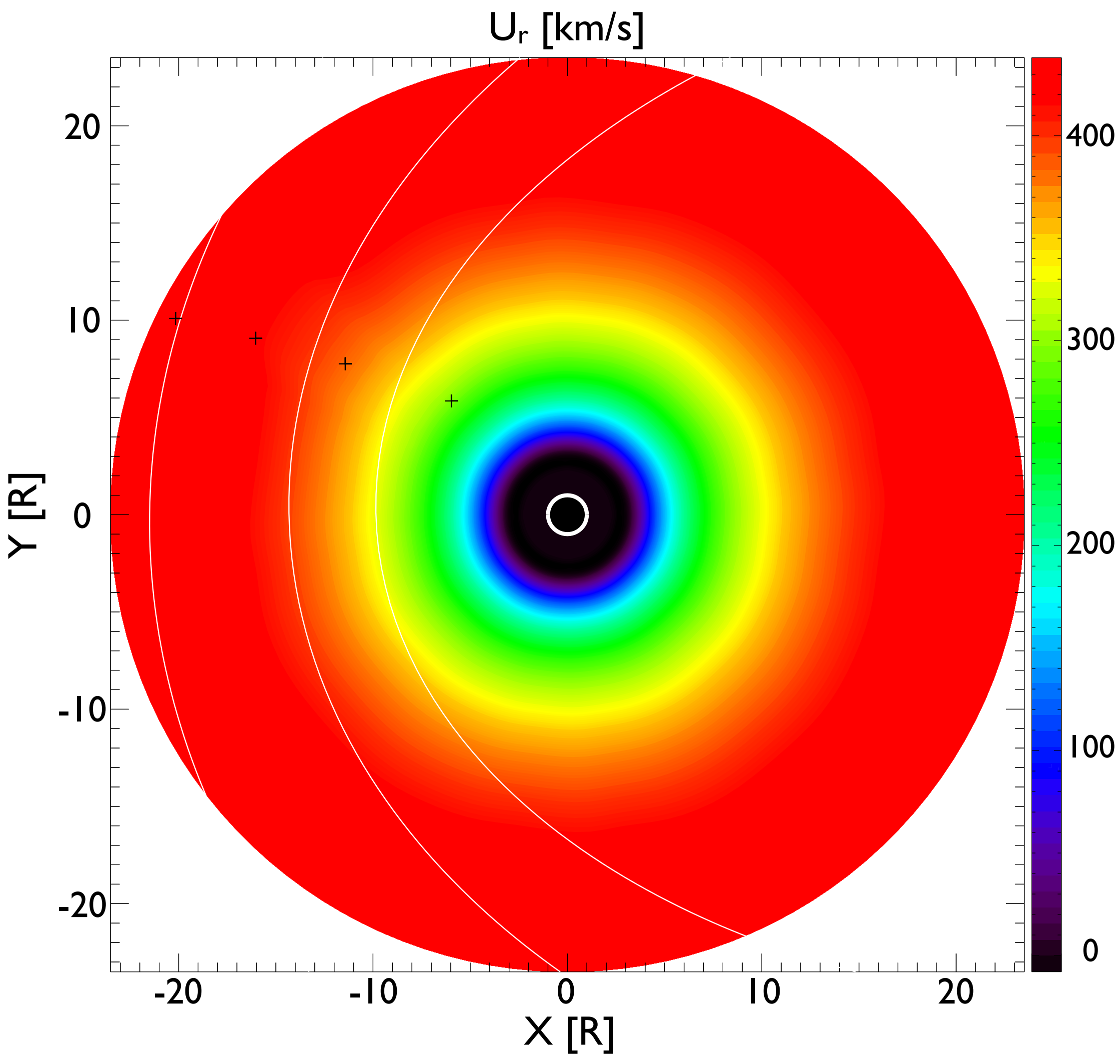

Figure 5.11: Undisturbed radial velocity plot of the solar corona in the xy-plane, with three SPP approaches overlaid and the four post-perihelion cometary locations of our focus (t_C = 6, 12, 18, and 24 hours).

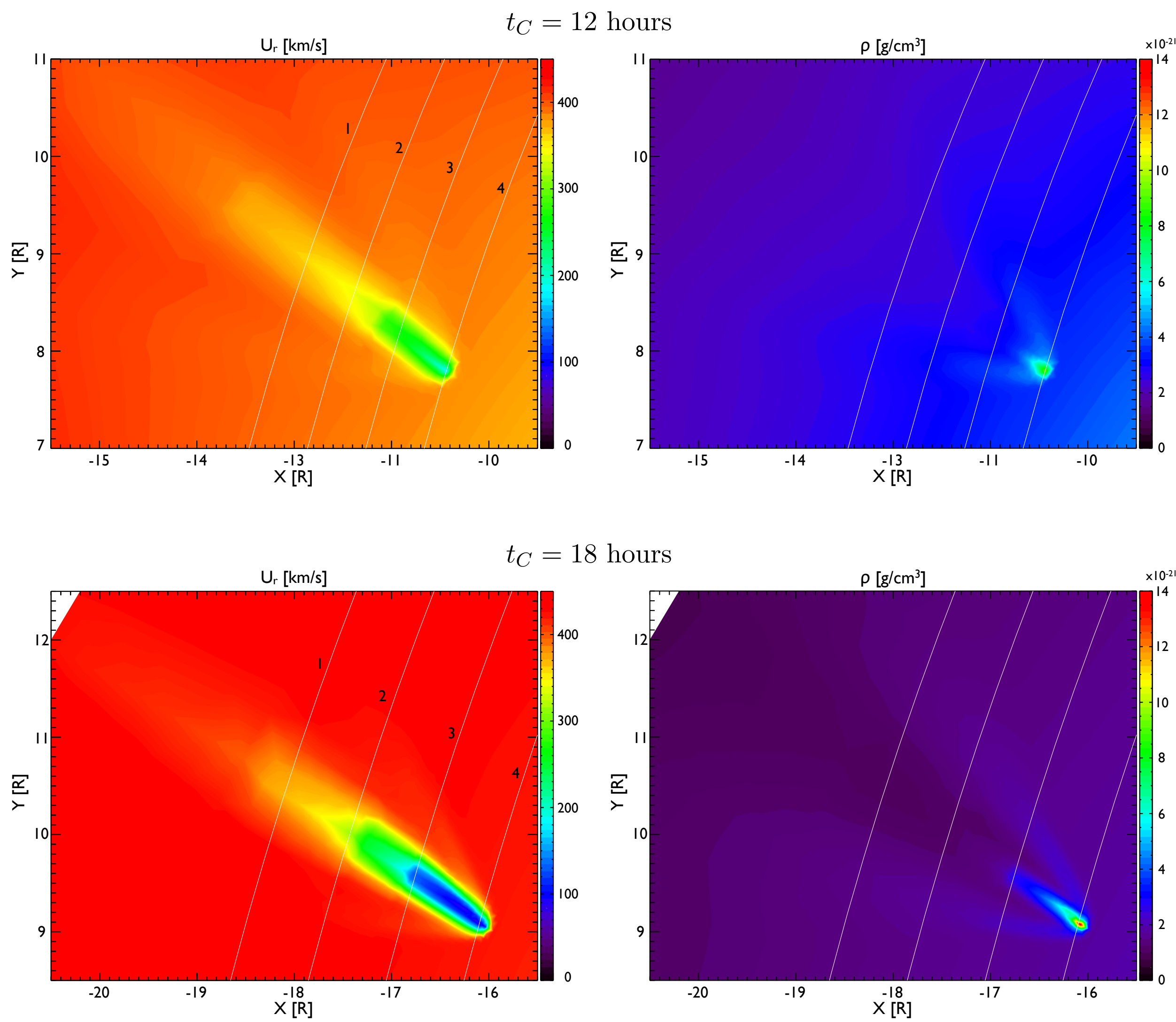

Figure 5.12: Radial velocity (left) and wind density (right) plots for $t_C = 12$ and $t_C = 18$ hours from Figure 5.10. Each has their respective nearest downwind SPP path from Figure 5.11 plotted, along with three similar paths.

Figure 5.13 shows the changes in the solar wind a solar probe such as SPP would see along the paths in Figure 5.12. The radial velocity plots show fairly typical changes, with drops in velocity, increasing in magnitude nearer the cometary source. However, solar wind density changes are a bit more interesting. Further downwind, changes seen along the path actually occur as a drop in solar wind density, contrary to what has been observed in previous chapters. This is the result of a wake seen only in the density plots of Figure 5.12. It is not until we get nearer to the cometary source that the results turn into a spike in solar wind density. This transition from a drop to a spike also involves increases in density on either side of the drop. This is seen best for $t_C = 18$ hours in Figure 5.13, where we actually get three distinct density peaks along Orbit 3, before having only one peak in Orbit 4.

Also, as with our mass-loading tests in Chapter 4, we can look at how the magnetic field strength is affected along the solar probe's path. Figure 5.13 shows the magnetic field strength B along all four paths for $t_C = 12$ (top) and $t_C = 18$ (bottom) hours. Changes in B correspond closely with changes in density, showing a build-up and magnetic wake downwind of the cometary source, even containing the same number of peaks in each respective curve. These again agree with results from the previous chapter.

These results, which are partially presented in Rasca and Horányi[37], are of course for our exaggerated mass-loading tail results in Figure 5.10. Variations in mass-loading rates would alter the strengths in the velocity and density drops/peaks observed. For example, results in Figure 5.9 for $t_C = 12$ and $t_C = 18$ hours only show velocity drops to around $350\,\mathrm{km/s}$, which would still be a prominent change to the surrounding solar wind, but not to the extent shown in Figure 5.13.

---

wind density is an adequate substitute for indicating the presence of mass-loading particles.

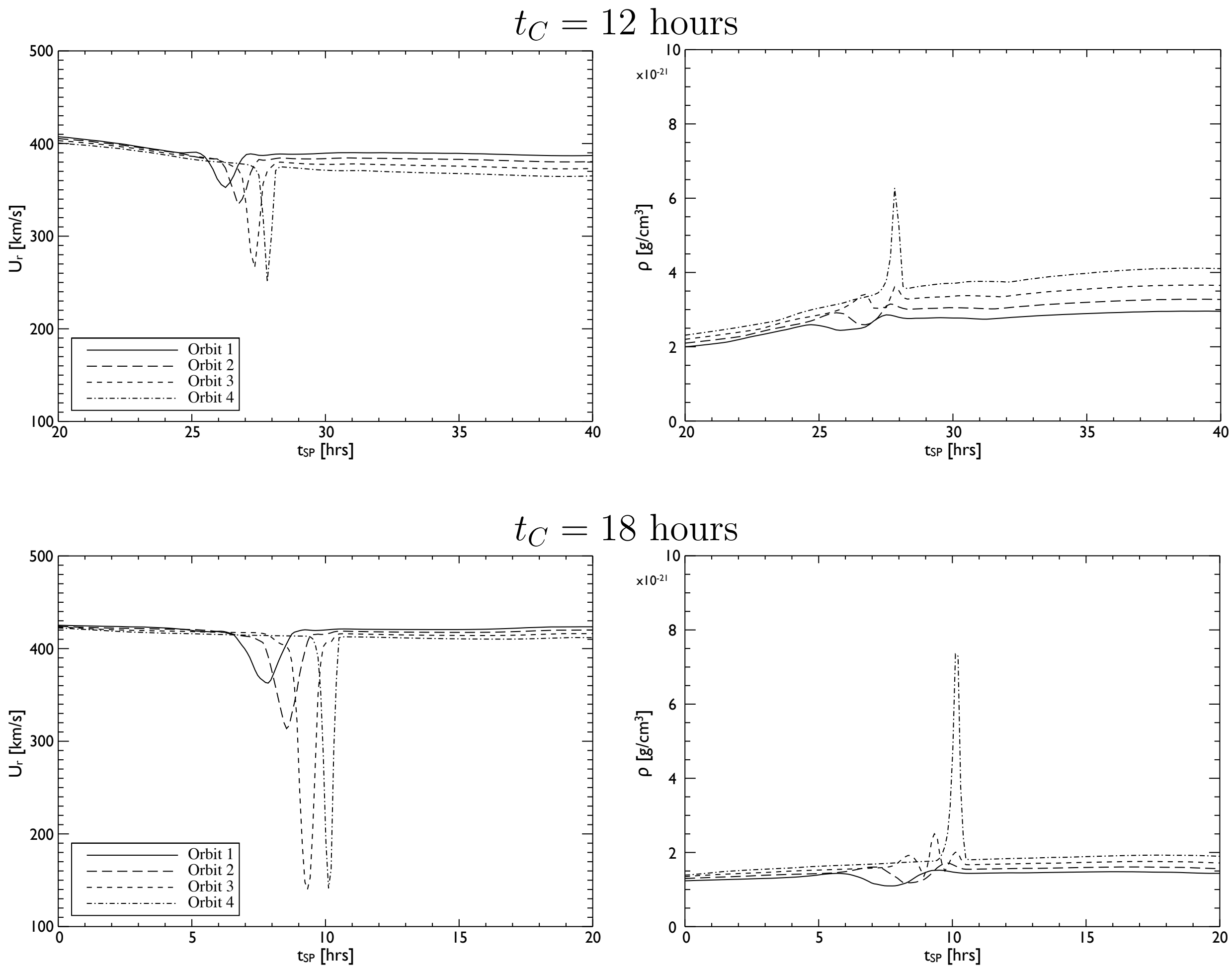

Figure 5.13: The solar wind radial velocity (left) and density (right) as seen along the orbits drawn in Figure 5.12 for $t_C = 12$ and $t_C = 18$ hours.

$t_C = 12$ hours

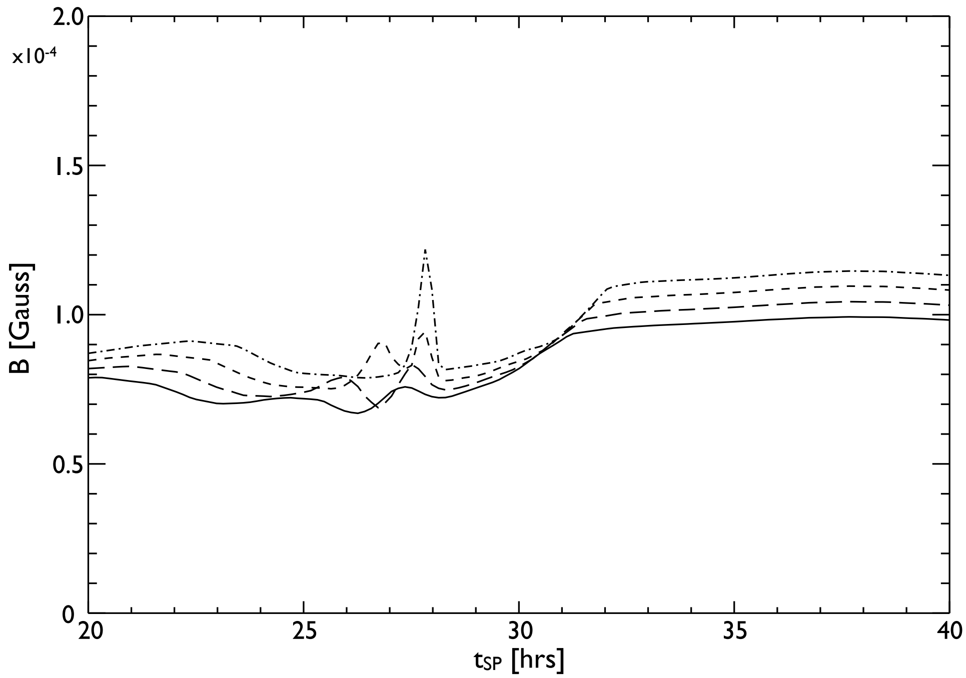

$t_C = 18$ hours

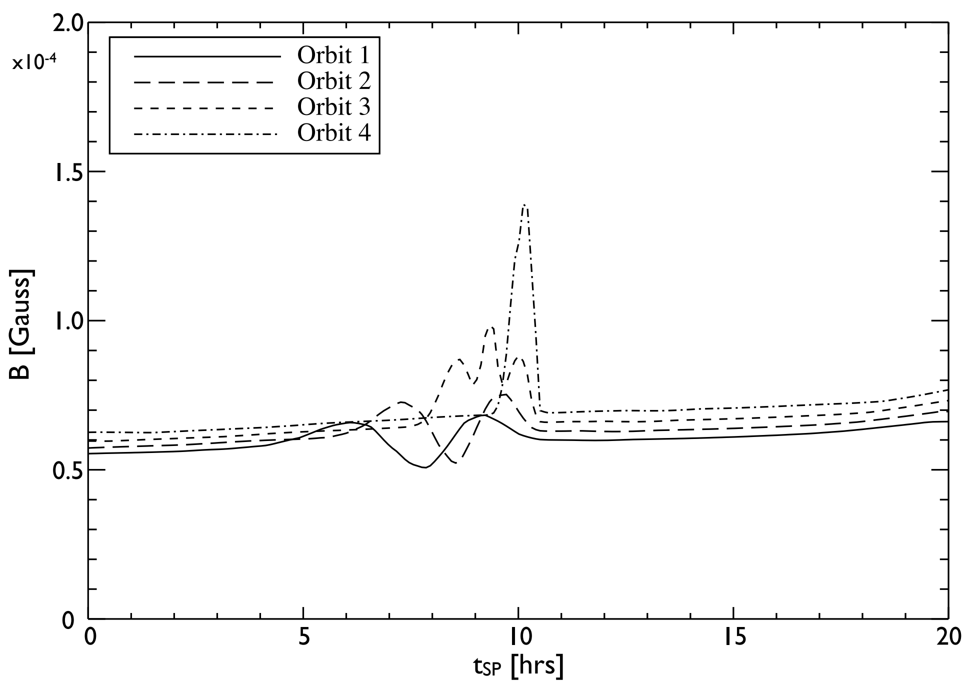

Figure 5.14: Magnetic field strength B along four solar probe paths for $t_C = 12$ (top) and $t_C = 18$ (bottom) hours from Figure 5.10.

Chapter 6

Summary and Conclusions

This thesis was motivated by the lack of a solar corona model capable of modeling effects of mass-loading by dust and by the potential for direct observations in the future. The presence of dust in the solar corona is already known through theoretical modeling and remote observations. Theoretical data obtained from the Solar Corona (SC) component modified for mass-loading can be used to predict how changes indicating a dust source in the coronal wind will appear, with the longterm goal being to eventually compare these results to direct observations.

In Chapter 2 we introduced the concept of mass-loading in a compressible hydrodynamic flow, while also mathematically deriving its nozzle-like effects. We also described a numerical solver for the time-dependent system of compressible 1D hydrodynamic equations (Euler's equations). The effects of mass-loading were demonstrated computationally with a uniform solar wind, using wind parameters appropriate for the slow solar wind at 1 AU from the Sun. These results also showed how a shock forms, forcing the solar wind to drop to subsonic velocities, followed by a mass-loaded subsonic solar wind mimicking the acceleration through a de Laval nozzle.

In Chapter 3 we moved to mass-loading the coronal wind with a spherically symmetric hydrodynamic model. We began by introducing the coronal wind with the first historical model, Parker's solution, and demonstrating that Euler's equations, with the appropriate heat transfer source terms, produce a more realistic coronal wind. The additional source terms introduced for the solar corona, namely heat transfer from collisional heat conduction, required amendments to numerical techniques introduced in Chapter 2. Mass-loading was then introduced at various distances from the Sun. These not only showed a similar effect to those in Chapter 2, where the region begin after the undisturbed sonic point, but also showed how a mass-loaded solar wind changes when it begins further upwind, where the coronal wind is still subsonic. In the latter case we get no shock, but a decelerated upwind flow.

In Chapter 4 we began our work with the Space Weather Modeling Framework, which contains a Solar Corona component based of the MHD BATS-R-US model. We described the SWMF and BATS-R-US code and proceeded to modify code for the SC component, originally a single-temperature model using Alfvén waves to accelerate the coronal wind, to make it multi-species (two separate mass conservation equations, one for hydrogen and the other for dust) and have it contain mass-loading source used in our 1D hydrodynamic model. We used the modified SC component to run mass-loading cases similar to those performed in Chapter 3. The effects on the corona wind velocity and mean molecular mass profiles shared several similarities to those in Chapter 3, but trends in the mean molecular mass were reversed with respect to mass-loading distance. The likely contributing factor to these discrepancies is variation in wind velocity between the 1D hydrodynamic and MHD models.

In Chapter 5 we used the modified MHD code from Chapter 4 to model changes in the coronal wind resulting for a sungrazing cometary dust source. First, using orbital characteristics and mass-loss estimates of Comet C/2011 W3 as an example, we treated the mass-loading region as a point source where the cometary body is located. This was done with four post-perihelion cometary locations within our SC domain. Each resulted in drops in wind velocity that stretch back to form radial tail features, increasing in strength with cometary distance from the Sun.

Second, we repeated our computational runs using a tail source (a tail-shaped mass-loading region) as opposed to a point source. Particle trajectories for ejected dust grains of various sizes were used to draw syndyne and synchrone curves, forming arcing dust tail regions. Using these updated mass-loading regions for the cometary source, and using both the same mass-loading rate as with our point sources and a $\times 10$ scaled mass-loading rate, we were able to make the following claims:

- With much of the ejected mass still near the cometary source, we get a similar imprint on the coronal wind velocity as with the point source. However, with the mass still spread out, the drop in velocity is significantly less.

- An order or magnitude increase of the mass-loading source term is enough to account for the dispersion of mass and regain comparable results to the point source results.

- Neither type of mass-loading region reveals a distinct arcing dust tail in any plots. For the tail source cases, the source term must be increased by a factor of 10^3 for any arcing feature to become evident in the radial velocity, but at this point the solar wind becomes severely disrupted near the cometary source.

Looking ahead to planned exploration of the solar corona, we looked at what a solar probe might see when traveling downwind of a sungrazing comet. The results show a general drop in radial velocity, decreasing in magnitude with distance from the cometary body. When looking at the wind density and magnetic field strength, features along a solar probe orbit reveal the presence of a wake further out, with multiple jumps in density nearer the cometary body.

The basic framework to compare future in-situ observations with theoretical modeling is established, but the next logical direction is to move from a multi-species code to a full-fledged multi-fluid code, motivated by the difference in particle size/properties between the native solar wind and dust. For work done in Chapter 4, this would split the solar wind into two fluids, one for the native solar wind particles and another for whichever species of dust particles we are interested in (micron-sized dust particles with the cases covered in Chapter 4). Unlike the multi-species model, where only the number of mass conservation equations is multiplied, we would need to solve an entire set of fluid equation for each fluid involved. For the cometary source application, this could become a difficult task, since we dealt with a spectrum of dust particle sizes. Similar multi-fluid work has been done using BATS-R-US, but as it applied to the Saturnian moon Enceladus (Jia et al.[22]; Jia et al.[21]; Jia et al.[20]).

Another direction, most likely post-multi-fluid, would be a fluid-kinetic model. This would be one of the more useful directions to go, as the solar wind is well-modeled as a fluid, but a population of dust particles are large and few, relative to native particles in the solar wind (protons and electrons). There is work currently in progress at CSEM to couple BATS-R-US to a kinetic dust model, which would likely be ideal for dust modeling in the solar corona.

Two possible physical aspects that can be explored with the cometary application involve the plasma tail and a better look at the time evolution of a mass-loading cometary tail. First, the plasma tail is a second cometary tail composed of ionized gases and points radially away from the Sun instead of arcing like a dust tail. Both tails result in a mass-loaded solar wind, making their combined impacts a topic of possible discussion. Second, with Comet C/2011 W3's perihelion in 2011, observations showed its dust tail vanishing, reappearing, and interacting with the Sun's magnetic fields at close-range (Schrijver et al.[43]). Incorporating a similar time evolution of the dust tail (and possibly the plasma tail) near and after perihelion with the mass-loading MHD simulations could reveal more interesting dynamical results.

Published and Presented Work

This thesis is based on the following refereed papers:

- A. P. Rasca and M. Horányi. Solar wind mass-loading due to dust. AIP Conference Proceedings, 1539:418-421, 2013.
- A. P. Rasca. M. Horányi, R. Oran, and B. van der Holst. Modeling solar wind mass-loading in the vicinity of the Sun using 3D MHD simulations, Journal of Geophysical Research, in review, 2013.
- A. P. Rasca and M. Horányi. Modeling solar wind mass-loading dust to a cometary source, in progress.

During this project partial results were presented at:

- American Geophysical Union Fall Meeting, 2011. "Solar Wind Mass-Loading Due to Dust," Poster Presentation.
- Center for Space Environment Modeling, Group Meeting Presentation, 2012. "Modeling Solar Wind Mass-Loading Due to Dust," Oral Presentation.
- Solar Wind 13 International Conference, 2012. "Solar Wind Mass-Loading Due to Dust," Contributed Talk.
- Institute for Astronomy, University of Hawaii at Manoa, Astrocoffee Talk, 2012. "Solar Wind Mass-Loading Due to Dust," Oral Presentation.
- In-Situ Heliospheric Science Symposium, 2012. "Modeling Solar Wind Mass-Loading Due to Dust," Oral Contribution.
- American Geophysical Union Fall Meeting, 2012. "Solar Wind Mass-Loading Due to Dust in the Vicinity of the Sun," Poster Presentation.

- USNC-URSI National Radio Science Meeting, 2013. "Modeling Solar Wind Mass-Loading Due to Dust in the Vicinity of the Sun," Oral Presentation.
- American Astronomical Society, Division for Planetary Sciences 45th Annual Meeting, 2013. "Modeling Solar Wind Mass-Loading Due to Cometary Dust," Poster Presentation.
- Department of Applied Mathematics, University of Colorado at Boulder, Dynamical Systems Seminar, 2013. "Modeling Solar Wind Mass-Loading Due to Dust in the Solar Corona," Oral Presentation.
- Laboratory for Atmospheric and Space Physics, University of Colorado at Boulder, Magnetospheres of the Outer Planets, Group Meeting Presentation, 2013. "Modeling Solar Wind Mass-Loading Due to Dust in the Solar Corona," Oral Presentation.

Bibliography

[1] Solar Probe Plus: Report of the science and technology definition team. Technical report, Goddard Space Flight Center, National Aeronautics and Space Administration, 2008.

[2] C. N. Arge and V. J. Pizzo. Improvement in the prediction of solar wind conditions using near-real time solar magnetic field updates. Journal of Geophysical Research, 105:10465–10480, 2000.

[3] Matania Ben-Artzi and Joseph Falcovitz. A second order Godunov-type scheme for compressible fluid dynamics. Journal of Computational Physics, 55:1–32, 1984.

[4] L. Biermann, B. Brosowski, and H. U. Schmidt. The interaction of the solar wind with a comet. Solar Physics, 1(2):254–284, 1967.

[5] Center for Space Environment Modeling. BATS-R-US and CRASH User Manual.

[6] J. Černý. URL: http://www.kommet.cz/page.php?al=prvni_snimky_komety_lovejoy_ ze_zeme.

[7] Alexandre Joel Chorin. Random choice solutions of hyperbolic systems. Journal of Computational Physics, 22:517–533, 1976.

[8] P. Colella. A direct Eulerian MUSCL scheme for gas dynamics. Journal of Scientific and Statistical Computing, 6:104–117, 1985.

[9] Francis Filbet, Claudia Negulescu, and Chang Yang. Numerical study of a nonlinear heat equation for plasma physics. International Journal of Computer Mathematics, 89(8):1060–1082, 2012.

[10] S. K. Godunov. A finite difference method for the computation of discontinuous solutions of the equations of fluid dynamics. Matematicheskii Sbornik, 47:357–393, 1959.

[11] T. I. Gombosi, T. E. Cravens, and A. F. Nagy. Time-dependent dusty gasdynamical flow near cometary nuclei. The Astrophysical Journal, 293:328–341, June 1985.

[12] T. I. Gombosi, A. F. Nagy, and T. E. Cravens. Dust and neutral gas modeling of the inner atmosphere of comets. Reviews of Geophysics, 24:667–700, August 1986.

[13] E. Grün, M. Horányi, and Z. Sternovsky. Lunar dust environment. Planetary and Space Science, 59(14):1672–1680, 2011.

[14] K. C. Hansen, Gábor Tóth, Aaron Ridley, and Darren De Zeeuw. BATS-R-US Design. Center for Space Environment Modeling.

[15] Ami Harten. High resolution schemes for hyperbolic conservation laws. Journal of Computational Physics, 49:57–393, 1983.

[16] Joseph V. Hollweg. Transition region, corona, and solar wind in coronal holes. Journal of Geophysical Research, 91:4111–4125, 1986.

[17] M. Horányi, V. Hoxie, A. Poppe, C. Bryant, B. Grogan, B. Lamprecht, J. Mack, F. Bagenal, S. Batiste, N. Bunch, T. Chanthawanich, F. Christensen, M. Colgan, T. Dunn, G. Drake, A. Fernandez, T. Finley, G. Holland, A. Jenkins, C. Krauss, E. Krauss, O. Krauss, M. Lankton, C. Mitchell, M. Neeland, T. Reese, K. Rash, G. Tate, C. Vaudrin, and J. Westfall. The Student Dust Counter on the New Horizons Mission. Space Science Reviews, 140(1-4):387–402, 2008.

[18] Mihály Horányi. Charged dust dynamics in the solar system. Annual Review of Astronomy and Astrophysics, 34:383–418, 1996.

[19] Arieh Iserles. A First Course in the Numerical Analysis of Differential Equations. Cambridge University Press, 1996.

[20] Y.-D. Jia, C. T. Russell, K. K. Khurana, Y. J. Ma, W. Kurth, and T. I. Gombosi. Interaction of Saturn's magnetosphere and its moons: 3. Time variation of the Enceladus plume. Journal of Geophysical Research, 115(A12), 2010.

[21] Y.-D. Jia, C. T. Russell, K. K. Khurana, Y. J. Ma, D. Najib, and T. I. Gombosi. Interaction of Saturn's magnetosphere and its moons: 2. Thape of the Enceladus plume. Journal of Geophysical Research, 115(A4), 2010.

[22] Y.-D. Jia, C. T. Russell, K. K. Khurana, G. Tóth, J. S. Leisner, and T. I. Gombosi. Interaction of Saturn's magnetosphere and its moons: 1. Interaction between corotating plasma and standard obstacles. Journal of Geophysical Research, 115(A4), 2010.

[23] Matthew M. Knight and Kevin J. Walsh. Will Comet ISON (C/2012 S1) survive perihelion? Astrophysical Journal Letters, 776(1), 2013.

[24] Alexander Kurganov and Eitan Tadmor. New high-resolution central schemes for nonlinear conservation laws and convection-diffusion equations. Journal of Computational Physics, 160:241–282, 2000.

[25] P. D. Lax and B. Wendroff. Systems of conservation laws. Communications on Pure and Applied Mathematics, 13(217-237), 1960.

[26] N. Lugaz, IV Manchester, W. B., and T. I. Gombosi. The evolution of coronal mass ejection density structures. The Astrophysical Journal, 627(2):1019–1030, 2005.

[27] I. Mann and R. M. MacQueen. Observation and analysis of the F-corona brightness. Advances in Space Research, 17(3):353–356, 1996.

[28] Ingrid Mann, Alexander Krivov, and Hiroshi Kimura. Dust cloud near the Sun. Icarus, 146(2):568–582, 2000.

[29] D. A Mendis, H. L. F. Houpis, and M. L. Marconi. The physics of comets. Fundamentals of Cosmic Physics, 10, 1985.

[30] N. Meyer-Vernet, M. Maksimovic, A. Czechowski, I. Mann, I. Zouganelis, K. Goetz, M. L. Kaiser, O. C. St. Cyr, J.-L. Bougeret, and S. D. Bale. Dust detection by the wave instrument on STEREO: Nanoparticles picked up by the solar wind? Solar Physics, 256:463–474, 2009.

[31] Nicole Meyer-Vernet. Basics of the Solar Wind. Cambridge University Press, Cambridge, 2007.

[32] K. W. Morton and D. F. Mayers Numerical Solution of Partial Differential Equations. Cambridge University Press, 2nd edition, 2005.

[33] E. N. Parker. Dynamics of the interplanetary gas and magnetic fields. American Astronomical Society, 128:664–676, 1958.

[34] E. N. Parker. Dynamical theory of the solar wind. Space Science Reviews, 4(5-6):666–708, 1965.

[35] R. Pinto, R. Grappin, Y.-M. Wang, and J. Leorat. Time-dependent hydrodynamical simulations of slow solar wind, coronal inflows, and polar plumes. Astronomy and Astrophysics, 497(2):537–543, 2009.

[36] Kenneth G. Powell, Philip L. Roe, Timur J. Linde, Tamas I. Gombosi, and Darren L. De Zeeuw. A solution-adaptive upwind scheme for ideal magnetohydrodynamics. Journal of Computational Physics, 154:284–309, 1999.

[37] A. P. Rasca and M. Horányi. Modeling solar wind mass-loading due to cometary dust. American Astronomical Society, DPS Meeting, Denver, CO, 2013.

[38] A. P. Rasca and M. Horányi. Solar wind mass-loading due to dust. AIP Conference Proceedings, 1539:418–421, 2013.

[39] A. P. Rasca, M. Horányi, R. Oran, and B. van der Holst. Modeling solar wind mass-loading in the vicinity of the Sun using 3D MHD simulations. Journal of Geophysical Research, submitted. 2013.

[40] J. J. Rennilson and D. R. Criswell. Surveyor observations of lunar horizon-glow. The Moon, 10:121–142, 1974.

[41] P. Riley, Z. Mikic, R. Lionello, J. A. Linker, N. A. Schwadron, and D. J. McComas. On the relationship between coronal heating, magnetic flux, and the density of the solar wind. Journal of Geophysical Research, 115(A6), 2010.

[42] P. L. Roe. Approximate Riemann solvers, parameter vectors, and difference schemes. Journal of Computational Physics, 43:357–372, 1981.

[43] Carolus J. Schrijver, Carey M. Lisse, and Cooper Downs. Comets as solar probes. Physics Today, 22:27–32, 2013.

[44] Zdenek Sekanina and Paul W. Chodas. Comet C/2011 W3 (Lovejoy): Orbit determination, outbursts, disintegration of nucleus, dust-tail morphology, and relationship to new cluster of bright sungrazers. The Astrophysical Journal, 757(2), 2012.

[45] E. F. Toro. A new numerical technique for quasi-linear hyperbolic systems of conservation laws. Technical Report CoA-8608, College of Aeronautics, Cranfield Institute of Technology, UK, 1986.

[46] E. F. Toro. Riemann solvers and numerical methods for fluid dynamics: a practical introduction. Springer, Berlin, 2nd edition, 1999.

[47] Gábor Tóth, Igor V. Sokolov, Tamas I. Gombosi, David R. Chesney, C. Robert Clauer, Darren L. De Zeeuw, Kenneth C. Hansen, Kevin J. Kane, Ward B. Manchester, Robert C. Oehmke, Kenneth G. Powell, Aaron J. Ridley, Ilia I. Roussev, Quentin F. Stout, Ovsei Volberg, Richard J. Wolf, Stanislav Sazykin, Anthony Chan, Bin Yu, and József Kóta. Space Weather Modeling Framework: A new tool for the space science community. Journal of Geophysical Research, 110(A12), 2005.

[48] Gábor Tóth, Bart van der Holst, Igor V. Sokolov, Darren L. De Zeeuw, Tamas I. Gombosi, Fang Fang, Ward B. Manchester, Xing Meng, Dalal Najib, Kenneth G. Powell, Quentin F. Stout, Alex Glocer, Ying-Juan Ma, and Merav Opher. Adaptive numerical algorithms in space weather modeling. Journal of Computational Physics, 231:870–903, 2012.

[49] B. van der Holst, W. B. Manchester IV, R. A. Frazin, A. M. Vásquez, G. Tóth, and T. I. Gombosi. A data-driven, two-temperature solar wind model with Alfvén waves. The Astrophysical Journal, 725(1):1373–1383, 2010.

[50] Bram van Leer. Towards the ultimate conservative difference scheme V. A second order sequel to Godunov's method. Journal of Computational Physics, 32(101-136), 1979.

[51] George L. Withbroe. The temperature structure, mass, and energy flow in the corona and inner solar wind. The Astrophysical Journal, 325:442–467, February 1988.